ABSTRACT

LEE, KYOUNGMI. Atomic Layer Deposition for Fiber Surface Modification and Nanosheet Fabrication. (Under the direction of Dr. Gregory N. Parsons).

Atomic layer deposition (ALD) is a vapor phase thin film deposition technique based upon the sequential dosing of precursor species. This sequential precursor delivery process affords precise control over thin film thickness in sub-nanometer resolution. Moreover, it is possible to vary film composition or create junctions by altering precursor chemistries in successive ALD processes.

We present the mechanism for wetting transition with X-ray photoelectron spectroscopy (XPS), in situ Fourier-transform infrared spectroscopy (in situ FTIR), and scanning electron microscope (SEM). The wetting property of cotton was modified only with a few number of ALD cycles. In situ FTIR and XPS suggest that Al-(O-C-)$_3$ bonding on the fiber surface bring about the change from hydrophilicity to hydrophobicity. Induced hydrophobicity is promoted from an increase in surface roughness after small number of Al2O3 cycles.

We show a new strategy to nanosheet synthesis that uses atomic layer deposition (ALD) and allows vast control over nanosheet composition and thickness. Nanosheets are two-dimensional (2D) materials with micro- to macro-scale lateral dimensions and nanometer to sub-nanometer thickness with unique electrical and mechanical properties. The two common routes to nanosheet synthesis, which are mechanical or chemical exfoliation from layered compounds, and vapor-phase or hydrothermal growth using morphologically constrained systems, suffer from limited control over nanosheet thickness or restriction to layered materials. We use metal oxide ALD films on a polymer sacrificial layer followed by dissolution to create nanosheets with

controlled thickness and show the photocatalytic activity of TiO_2 and ZnO nanosheets under UV light. Surface area and thickness of nanosheets as well as UV light intensity affect dye photodegradation rate according to the kinetic equation. More importantly, TiO_2/ZnO bilayer nanosheets from two successive ALD processes promote dye photodegradation > 5 times than TiO_2 nanosheets under UV light.

Cu_2O films are grown by electrodeposition. They all have pyramidal triangular grain in shape but the size depends on deposition temperature, pH of the solution, and deposition time. To increase electrochemical stability, TiO_2 ALD film with Al-doped ZnO buffer layer is deposited on Cu_2O films but the expected increase in stability is not observed.

Free-standing Cu_2O sheets are obtained using flexible ITO-PET substrates. Simple bending after electrodeposition isolates Cu_2O film from the substrates. Dye molecules are degraded with Cu_2O sheets for the first 30 min but it is recovered after 30 min under UV light while Cu_2O sheets with ZnO ALD layer prevent dye reduction showing continuous degradation. Under visible light, however, dye recovery is not observed with Cu_2O sheets. Although ZnO film prevents reduction of dye molecules, photocatalytic activity of Cu_2O sheets is decreased after ALD.

Atomic Layer Deposition for Fiber Surface Modification and Nanosheet Fabrication

by
Kyoungmi Lee

A dissertation submitted to the Graduate Faculty of
North Carolina State University
in partial fulfillment of the
requirements for the degree of
Doctor of Philosophy

Chemical Engineering

Raleigh, North Carolina

2013

APPROVED BY:

_____	_____
Gregory N. Parsons Committee Chair	Saad A. Khan
_____	_____
Orlin D. Velev	Michael D. Dickey

DEDICATION

To

My husband, Do Han Kim

My daughter, Averie Dasol Kim

My mother, Jonghee Gwon

My father, Hwadoo Lee

for their love, encouragement, and belief

BIOGRAPHY

Kyoungmi Lee was born in Daegu, South Korea in 1980. She spent childhood and teenage years there until 1999. In 1999, she moved to Seoul and studied chemical engineering in Seoul National University. After earning bachelor's degree, she researched the phase separation of polystyrene/poly(methylmetacrylate) for Master's Degree in Seoul National University under the guidance of Dr. Honghee Lee. After graduation in 2003, she joined in LCD department in Samsung electronics (Giheung, South Korea) as an engineer where she was responsible for reliability test of the developing small to mid-size LCD panel and analysis of defective products for two years. To seek doctoral degree, she started to study in Chemical and Biomolecular Engineering at North Carolina State University in 2008 under the guidance of Dr. Gregory N. Parsons. Her research focused on surface modifications of fibers by atomic layer deposition for the first two years after joining to Parsons Research group. Now she is working on the fabrication of metal oxide nanosheet for photocatalysts and water splitting.

ACKNOWLEDGMENTS

First of all, I would like to express my great appreciation to Dr. Gregory Parsons, y advisor, for his constructive advices and encouragement. He always took my research results seriously no matter how it looked trivial and patiently guided me to the next step with valuable advices. I respect his aggressive attitude and enthusiasm for research.

I want to thank my committee members, Dr. Saad Khan, Dr. Orlin Velev, and Dr. Michael Dickey for the valued advices and discussion.

I am grateful to all of Parsons Research group members for their assistance. Especially, I want to show my appreciation to Dr. Jess Jur, Dr. Mark Losego, and Do Han Kim for their contributions to my published and submitted papers as co-authors. Also, I would also like to extend my thanks to Berc for his help to fabricate photoelectrodes and set up the electrodeposition station.

I thank my Korean friends, Hyungjun Koo, Ju-hee So, Daniel Seo, and Hyojeong Kim for having great time here and sharing good memories during last five years.

I would also like to thank my parents for their endless love, encouragement, and sacrifice. I thank my brother, sister, and sister-in-law, and my only niece. My family is the best motivation for me to pursue further studies.

Lastly but most importantly, I want to express my special thanks to my husband, Do Han Kim for his encouragement and love. He enjoyed a discussion about experiments and results with me whenever and wherever we were. Our awesome daughter, Averie, I love, love, love you and thank you for your smile that makes me the happiest mom in the world.

TABLE OF CONTENTS

LIST OF TABLES x

LIST OF FIGURES xi

Chapter 1. Introduction 1

1.1 Overview of Atomic Layer Deposition 2

1.1.1 ALD on polymer films 6

1.1.2 ALD on bio-templates 8

1.1.3 ALD on fibers 8

1.2 Water splitting; principles and recent research 11

1.2.1 Metal oxide nanosheets for water splitting 16

1.3 Summary 18

References 20

Chapter 2. ALD Process and Analysis Tools 34

2.1 ALD rector 35

2.2 Spectroscopic Ellipsometry 35

2.3 Contact angle goniometer 36

2.4 In situ Fourier transform infrared spectroscopy (In situ FT-IR) 37

2.5 X-ray photoelectron spectroscopy (XPS) 38

2.6 Scanning electron microscopy (SEM) 38

2.7 Transmission electron microscopy (TEM) 39

2.8 Atomic force microscopy (AFM) 39

2.9 X-ray diffraction spectrometer (XRD) 40

2.10 UV-visible spectrophotometer 40

2.11 UV lamp 41

References 42

Chapter 3. Mechanisms for Hydrophilic/Hydrophobic Wetting Transitions on Cellulose Cotton Fibers Coated using Al_2O_3 Atomic Layer Deposition 44

Abstract 45

3.1 Introduction 46

3.2 Experimental Procedure 47

3.3 Results and Discussion 49

3.4. Summary 60

References 62

Chapter 4. High Performance Photocatalytic Metal Oxide Synthetic Nanosheets Formed by Atomic Layer Deposition 67

Abstract 68

4.1 Introduction 69

4.2. Experimental process 69

4.3. Results and discussion 72

4.4. Photodegradation mechanism 83

4.5 Summary 87

References 89

Chapter 5. Effects of Sacrificial Polymers and Materials on Nanosheets Synthesis by Atomic Layer Deposition 94

Abstract 95

5.1 Introduction 96

5.2 Experimental 99

5.3 Results & Discussion 101

5.4 Summary 108

References 109

Chapter 6. Field Effect Transistor by Nanosheets Fabricated using Atomic Layer Deposition 115

6.1 Introduction 116

6.2 Experimental Procedure 117

6.3 Results and Discussion 118

6.4 Summary 120

References 121

Chapter 7. Photoeletrochemical Properties of Electrodeposited Cu_2O Film 122

7.1 Introduction 123

7.2 Experimental procedure 125

7.3 Results and Discussion 127

7.4 Summary 135

References 136

Chapter 8. The Effect of ZnO ALD film on Free-standing Cu_2O Sheets by Electrodeposition on Dye Photodegradation 140

8.1 Introduction 141

8.2 Experimental procedure 142

8.3 Results and Discussion 144

8.4 Summary 150

References 151

Chapter 9. Summary and Outlook 155

9.1 Summary 156

9.2 Outlook 158

References 160

APPENDIX 161

Atomic Layer Deposition and Abrupt Wetting Transitions on Nonwoven Polypropylene and Woven Cotton Fabrics 162

Temperature-Dependent Subsurface Growth during Atomic Layer Deposition on Polypropylene and Cellulose Fibers 164

SiNx Charge-Trap Nonvolatile Memory Based on ZnO Thin-Film Transistors 168

Wetting Properties Induced in Nano-Composite POSS-MA Polymer Films by Atomic Layer Deposited Oxides 169

Stable Anatase TiO_2 Coating on Quartz Fibers by Atomic Layer Deposition for Photoactive Light-Scattering in Dye-Sensitized Solar Cells 170

Atomic Layer Deposition of High Performance Ultrathin TiO_2 Blocking Layers for Dye-Sensitized Solar Cells 172

Mechanisms and Reactions During Atomic Layer Deposition on Polymers 174

LIST OF TABLES

Table 4.1 Rate of dye degradation. Taken from ln(C/Co) vs. time using eq. (1) for various nanosheet materials dispersed in aqueous solution. The photo intensity is fixed at I_0 = 245 μW/cm^2 and the overall surface area of the nanosheets is fixed at 160 cm^2. The TiO_2/ZnO nanosheets show more than a factor of 5 improved degradation rate compared to TiO_2 nanosheets alone.....82

Table 5.1 Fabrication methods and thickness of nanosheets.....98

LIST OF FIGURES

Figure 1.1 Schematic illustration of one ALD cycle.8 One cycle is consisted of four steps. Step 1: precursor is exposed on the surface with reactive groups; Step 2: unreacted precursor and byproducts purged with an inert purge gas; Step 3: co-reactant is exposure and reacts with the surface groups; Step 4: unreacted co-reactant and byproducts are purged. 3

Figure 1.2 Scheme of (a) an ALD processing window limited by (b) precursor condensation, (c) insufficient reactivity, (d) precursor decomposition and (e) precursor desorption. If the deposition rate is dependent on the number of available reactive sites as in (f), actual ALD window cannot be observed. 4

Figure 1.3 Model for Al_2O_3 ALD on polymer films showing (a) cross section of polymer film represented by loosely packed circles, (b) Al_2O_3 nucleation clusters forming from H_2O reaction with TMA trapped in the near surface region, (c) coalescence of Al_2O_3 clusters and closure of space between polymer chains, and (d) formation of dense Al_2O_3 film that grows on top of the polymer surface 7

Figure 1.4 Cross sectional transmission electron microscopy images of polypropylene fibers extracted from a nonwoven fiber mat after processing with aluminum oxide ALD at 60 °C with (a) 100 and (b) 1000 ALD cycles, and at 90 °C with (c) 100 and (d) 1000 cycles.[47] Uniform surface modification is observed on all samples. Processing at 60 °C (panels a and b) show nearly uniform encapsulation of the polypropylene fiber surface. When deposition is performed at 90 °C, however, (panels c and d) intermixing between the oxide and the polypropylene is observed. The cracks in the coatings and voids in the polymer result from the microtome sample preparation. 10

Figure 1.5 (a) Schematic illustration of water splitting over semiconductor photocatalyst and (b) its band energy diagram that spread over water oxidation and reduction potential. 13

Figure 1.6 Band-gap energies and relative band positions of different semiconductors relative to the water oxidation/reduction potential vs NHE..... 15

Figure 2.1 Schematic diagram of the in situ FTIR ALD/MLD reactor. In the middle part of the chamber, two gate valves are installed between the IR window and reactor chamber to prevent the deposition of ALD/MLD film on the windows. The IR beam goes through the planar sample and focused into a MCT-A detector. 37

Figure 3.1 Water contact angle on cotton fiber mats after (a) Al_2O_3 ALD and (b) ZnO ALD at 60 and 90 °C. In both cases, hydrophilic cotton fibers change to hydrophobic after a few number of ALD cycles, and come back to hydrophilic again after a certain number of ALD cycles with no significant dependence on the deposition temperature and different kinds of metal oxide film. 50

Figure 3.2 Pictures of a water drop on (a) cotton ball and (b) cotton fiber mat after changed to hydrophobic with 3 cycles of Al_2O_3 ALD at 60 ºC. (c) The magnified image that shows the interface between cotton fiber mat and water drop. (d) To test stability of hydrophobic cotton, cotton ball with 3 cycles of Al_2O_3 ALD was placed in water with bare cotton ball and it has been floated on water surface more than a month, which shows that hydrophobicity induced by ALD is a stable property. 51

Figure 3.3 Water contact angle (WCA) on cotton fiber mats after (a) a repeated sequence of 3 Al_2O_3 ALD cycles 60 ºC followed by air exposure and contact angle measurement (sequence labeled "A"); and (b) after a different procedure involving sequence "A" and sequence "Z", where "Z" corresponds to 3 ZnO ALD cycles followed by contact angle measurement in air. In both cases, the surface remains hydrophobic even after more than 10 repetitions (i.e. after more than 30 ALD cycles). Samples prepared using 30 cycles of ALD coating without breaks for air exposure produced a hydrophilic finish. 54

Figure 3.4 XPS spectra of bare cotton fiber mat (black line), cotton fiber mats after 3 cycles (red line), and 50 cycles (blue line) of Al_2O_3 ALD at 60 ºC. (a) The predominant peaks at 286.2 and 287.8 eV from bare cotton fiber mat correspond to O-C-O and C-O bonds, respectively, but the intensity of those peaks is decreased with increasing ALD cycles. (b) Al-O-C peak is shown on the cotton fiber mat after 3 cycles of ALD, whereas Al-O peak

becomes dominant with 50 cycles of ALD. (c) Al-O-C peak on cotton fiber mat after 3 cycles and Al-O peak after 50 cycles of Al_2O_3 ALD are consistent with the peaks shown in (b)..... 55

Figure 3.5 In-situ FTIR spectra collected after 1st and 10th TMA and H_2O dose at 60 ºC on cotton fiber mat with the absorption spectrum of the untreated cotton (bottom) and differential spectra after TMA and water exposure cycles. Peak changes at 1210 and 1460 cm^{-1} indicated by dot lines correspond to symmetric and asymmetric CH_3 deformations. These deformation modes are not visible during the first TMA exposures, but are visible after the 10th TMA dose. Furthermore, the broad peak change between 3080 and 3650 cm^{-1} shows a sequential decrease and increase in the bonded OH corresponding to TMA and H_2O doses, respectively. 57

Figure 3.6 FESEM images of bare cotton ball (a – c), cotton ball after 3 cycles of Al_2O_3 ALD (d – f), and 50 cycles of Al_2O_3 ALD at 60 ºC (g – i). (a, d, g) Each cotton fiber consists of a lot of fibrils. (b, e, h) The surfaces of cotton fibers look covered by Al_2O_3 film when ALD cycles increases. Some cracks on the surface of cotton fiber ball after 50 cycle of ALD are induced by the stiffness of Al_2O_3 film. (c, f, i) Higher resolution images show rougher surface after 3 cycles of Al_2O_3 ALD compared with other cotton balls. 58

Figure 4.1 Fabrication of synthetic ALD nanosheets. (a) Polymer solution of 2 wt% was spin-coated on Si substrate as a sacrificial layer. (b) Metal oxide ALD was performed onto the polymer layer with desired thickness and materials. (c) Pre-cuts were made into the polymer surface to facilitate dissolution of the polymer. (d) The polymer was removed by dipping in a solvent and ALD films were separated as nanosheets randomly dispersed in aqueous solution..... 73

Figure 4.2 Microstructure of synthetic ALD nanosheets. (a) Graph of TiO_2 nanosheet thickness collected from AFM height profiles (squares) and from ellipsometry (diamonds) as a function of the number of ALD cycles. AFM images and height profiles of TiO_2 nanosheets from 25 ALD cycles (b), Al_2O_3 nanosheets from 50 ALD cycles (c), and ZnO nanosheet

from 100 ALD cycles (d). These micrographs show the minimum nanosheet thickness achieved for each material. 74

Figure 4.3 TEM images of TiO_2 nanosheet annealed at 450 °C for 1 h (e) and ZnO nanosheet annealed at 300 °C for 1 h (f). Magnified inset images obtained from the red areas show the lattice parameter for each material. 75

Figure 4.4 Bilayer nanosheets synthesized by ALD. (a) Illustration showing deposition order and the number of ALD cycles for the ZnO/TiO_2 bilayer film. (b) EDX spectrum taken from the edge of the bilayer nanosheet shown in the inset SEM image. (c) AFM image and height profile of the bilayer nanosheet. (d) Picture of TO_2/ZnO bilayer nanosheets dispersed in DI water and nanosheets collected in a vial (inset). 76

Figure 4.5 Photocatalytic behavior of synthetic ALD nanosheets. (a) The concentration of methyl orange versus UV exposure time onto TiO_2 nanosheets of various thickness (1.3, 2.5, and 5 nm). Black squares show the control data for methyl orange concentration versus time without nanosheets present. (b) Plot of apparent rate constants (*K)* versus surface area extracted from the data shown in (a) 78

Figure 4.6 Dye degradation rate depending on UV intensity. (a) Degradation of methyl orange using photocatalytic TiO_2 nanosheets under varying UV intensity (122.50, 183.75, and 245.00 $\mu W/cm^2$). (b) Values of *K* obtained from the fits in (a) versus UV intensity. The value of k'' is 3.8×10^{-11} $s^{-1}cm^{-2}\mu W^{-1}nm^{-1}$. 79

Figure 4.7 Dye degradation rate depending on concentration of nanosheets. (a) Degradation of methyl orange using photocatalytic TiO_2 nanosheets under varying surface area of nanosheets (20, 40, and 160 cm^2). (b) k'' values versus *S* for 2.5 nm (black square) and 5 nm (red circle) thickness. The k'' is expected to decrease with increasing *S* due to scattering effects. The dashed lines are guides for the eye. (c) Illustration that shows how surface area of nanosheets affects UV light scattering. 80

Figure 4.8 (a) Schematic band energy diagram of TiO_2/ZnO bilayer nanosheets. Photogenerated holes get trapped in the ZnO layer while photogenerated electrons become trapped in the TiO_2 layer, limiting recombination and enhancing photocatalytic performance. (b) Photodegradation of methyl orange with UV-irradiation time for control solution without nanosheets (black squares), TiO_2 nanosheets (red circles), ZnO nanosheets (green triangles), and ZnO/TiO_2 bilayer nanosheets (blue diamonds) of similar nanosheet thickness (5 nm) and concentration (160 cm^2). Each number represents K ($\times 10^{-3}$)..... 81

Figure 5.1 Optical microscopic images of Al_2O_3 nanosheets from (a) 10 cycles and (b) 50 cycles, TiO_2 nanosheets from (c) 25 cycles and (d) 300 cycles, and ZnO nanosheets from (e) 100 cycles and (f) 150 cycles..... 102

Figure 5.2 TEM images of ZnO nanosheets from ALD 50 cycles. (a) ZnO nanosheets show the size less than 200 nm and (b) lattice spacing of 3.25 Å confirms ZnO crystallinity. 104

Figure 5.3 Graphs comparing the nanosheet thickness measured from AFM to the film thickness from ellipsometry depending on ALD cycles for (a) Al_2O_3, (b) ZnO, and (c) TiO_2 104

Figure 5.4 AFM image of Al_2O_3 nanosheet obtained from (a) ALD 5 cycles and (c) 100 cycles. (b) and (d) are the magnified images inside nanosheet marked with the dotted box from (a) and (b). (e) Al_2O_3 nanosheet from ALD 100 cycles with smooth surface. (f) AFM image of spin-coated PVA (Mw=16,000) used as a sacrificial layer. 107

Figure 5.5 Pictures of (a) TiO_2/PMMA bilayer sheets separated during PAA dissolution and (b) ZnO/PMMA bilayer sheets during PVA dissolution. 108

Figure 6.1 Schematic illustration of LiVO-graphene based transistor..... 117

Figure 6.2 Optical microscopic images of (a) TiO_2 nanosheet place on SiO_2/B-doped Si wafer after annealed and (b) after Au/Cr thermal evaporation on both sides of nanosheets. (c) Picture showing TiO_2 nanosheet FET with a total size of ~1.1 cm. 118

Figure 6.3 (a) I_{DS}-V_{DS} graph under various gate voltage (-4 – 4 V). (b) I_{DS}-V_G graph under V_{DS} = 1 V. 119

Figure 7.1 Conduction and valence band edges for Cu_2O and TiO_2 (vs. SHE) in comparison with redox potentials of relevant species. A solution pH of 6 was assumed. 124

Figure 7.2 Pictures of electrodeposited Cu_2O film on FTO glass with varying solution pH and deposition temperature for 10 min. 128

Figure 7.3 (a) Graph of Cu_2O film thickness electrodeposited for 10 min depending on deposition temperature with varying pH of the solution. As temperature or pH of the solution is increased, film is thicker. (b) XRD spectrum of Cu_2O film on FTO glass grown with the solution of pH 10 at 40 °C for 1 h. The peaks from Cu_2O film and FTO glass are marked with red circles and open black circles, respectively. 129

Figure 7.4 SEM images of electrodeposited Cu_2O film on FTO glass with the solution (pH 11) at 40 °C (a) for 10 min and (b) for 1 h. The Cu_2O grains grow larger (~2 um) for l h electrodeposition. (c) and (d) are Cu_2O films with the solution (pH 12) at 40 °C for 10 min and for 1 h, respectively. The grain size for 1 h electrodeposition is ~5 um which is bigger than that for 10 min electrodeposition (~2 um). Also, high pH solution produces bigger Cu_2O grains. 130

Figure 7.5 SEM images of electrodeposited Cu_2O film on FTO glass with the solution (pH 12) for 10 min at (a) 40 °C, (b) 50 °C, (c) 60 °C, and (d) 70 °C. The grain size is increased as the deposition temperature is increased. 131

Figure 7.6 (a) CV measurement and (b) chopped illumination measurement (0 V vs NHE) for electrodeposited Cu_2O film for 10 min at 40 °C (pH 11). (c) CV measurement and (d) chopped measurement (0 V vs NHE) for electrodeposited Cu_2O film for 1 h at 40 °C (pH 11). 132

Figure 7.7 (a) CV measurement and (b) chopped measurement for electrodeposited Cu_2O film for 10 min at 40 °C (pH 11) with ALD film. (c) CV measurement and (d) chopped

measurement for electrodeposited Cu_2O film for 10 min at 40 °C (pH 11) with ALD film followed by annealing at 200 °C for 45 min in air. Here, ALD film is composed of total 5 cycles of Al:ZnO (ZnO 25 cycles and Al_2O_3 1 cycle) and 210 cycles of TiO_2. 134

Figure 8.1 Pictures of ITO-PET film (a) before electrodeposition and (b) after electrodeposition for 40 °C 1 h. (c) Cu_2O film is easily separated from the substrate by bending. Inset shows the rolled-up Cu_2O sheet. (d) Picture of the isolated Cu_2O sheet that has a length of ~5 mm. 145

Figure 8.2 Photodegradation of methyl orange under UV-irradiation with (a) Cu_2O sheets and (b) Cu_2O sheets with ZnO ALD film (~17 nm) depending on UV irradiation time. (c) Absorbance spectrum of MO solution with Cu_2O sheets every 10 min for 30 min. The dotted arrow indicates decrease in absorbance at 466 nm. (d) Absorbance spectrum (250–650 nm) of MO solution with Cu_2O sheets with ZnO ALD film from 30 min to 150 min (30, 40, 50, 70, 80, 90, 100, and 150 min). The absorbance at 466 nm keeps increasing during measurement without peak shift. 146

Figure 8.3 Photodegradation of MO solution with Cu_2O sheets under UV light. Cu_2O sheets were filtered after 90 min measurement. After that, there is no change in concentration. ... 147

Figure 8.4 Linear plots of ln (C/C_0) vs UV irradiation time with (a) Cu_2O sheets and (b) Cu_2O sheets with ZnO ALD film (extracted from Figure 7.2a and b). The slopes mean the apparent rate constant. SEM images of (a) Cu_2O film electrodeposited for 1 h and (b) Cu_2O film electrodeposited for 1 h followed by ZnO ALD 100 cycles at 60 °C. 148

Figure 8.5 (a) Dye degradation under visible light with Cu_2O and Cu_2O/ZnO and (b) ln (C/C_0) vs visible light irradiation time plots calculated from (a). The apparent rate constant extracted from the slope is 0.024 min^{-1} or 0.003 min^{-1} for Cu_2O and Cu_2O/ZnO sheets, respectively. 149

Chapter 1

Introduction

1.1 Overview of Atomic Layer Deposition

Atomic layer deposition (ALD) is a very effective thin film deposition technique for growing conformal inorganic or organic films with monolayer thickness on substrates. Since initially developed in 1970s by T. Suntola,[1] ALD produces uniform, conformal, dense, and pin-hole free films even on complex 3D structures as well as a planar substrates over the entire surface.[2,3] Therefore, ALD has grown remarkably and it is expanding applications to microelectronics, nanotechnology, and optoelectronics for gate oxides, capacitors, insulators, and dielectric multilayers with scaling down to sub-nanometer dimensions.[4-6] ALD is a kind of chemical vapor deposition (CVD) but alternate dose of precursor differentiates ALD from CVD. In CVD, all reactants are dosed at the time and the reactions between them occur on the surface so that it produces high purity bulk materials.[7] On the other hand, in ALD, reactant and co-reactants are dosed in gas phase alternatively and the film is deposited in atomic scale by self-limiting reactions. In addition, CVD strongly depends on deposition temperature but ALD is affected less than CVD.

Schematic illustration of one ALD cycle which consists of four steps is shown in Figure 1.1.[8] In step 1, precursor is exposed on a substrate with reactive surface groups and reacts with them. The unreacted precursor and byproducts after reaction are purged with an inert gas in step 2. In the next two steps, a co-reactant is exposed into a reactor to form a film in atomic range followed by purging of the excess reactants and byproduct. By repeating the steps, films are grown with exact thickness control. Since ALD is based on sequential self-limiting reaction of precursor and reactant, film thickness can be precisely controlled by the

number of ALD cycles. The growth per cycle (GPC) depends on only growth temperature, substrate, pressure of reactants, and pulse time. The amount of precursor has no effect on GPC when the surface is saturated.

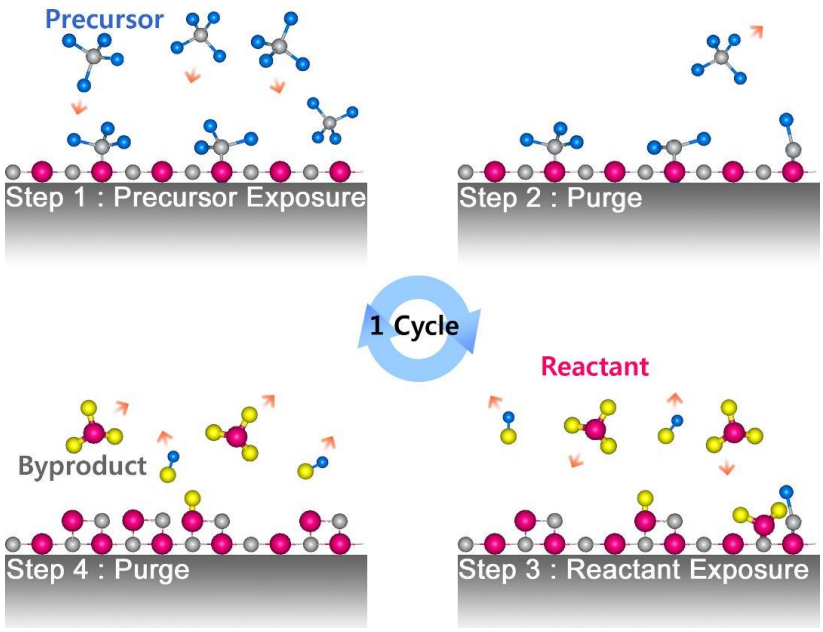

Figure 1.1 Schematic illustration of one ALD cycle.[8] One cycle is consisted of four steps. Step 1: precursor is exposed on the surface with reactive groups; Step 2: unreacted precursor and byproducts purged with an inert purge gas; Step 3: co-reactant is exposure and reacts with the surface groups; Step 4: unreacted co-reactant and byproducts are purged.

In ALD process, deposition temperature is critical for uniform and conformal film growth. The temperature range within the film is grown by surface control is called ALD window where the growth rate is constant.[9] Figure 1.2 shows scheme of (a) ALD window.[10] In lower temperature than ALD window, growth rate is limited by (b) precursor condensation

or (c) insufficient reactivity. On the other hand, as temperature is increased outside ALD window, it is limited by (d) precursor decomposition or (e) precursor desorption. If there is no constant GPC, the film growth is controlled by the available reactive site on the surface (f). ALD window depends on precursors because of the different partial pressure. If the partial pressure is not enough to saturate the surface, growth rate is below that in ALD window. For example, the ALD window for ZnO film with zinc acetate, [$Zn(CH_3COO)_2$], is found to be 280 – 350 °C while the ALD windows for diethylzinc [$Zn(C_2H_5)_2$] and dimethylzinc [$Zn(CH_3)_2$] are 100 – 180 °C and 80 – 150 °C, respectively.[11]

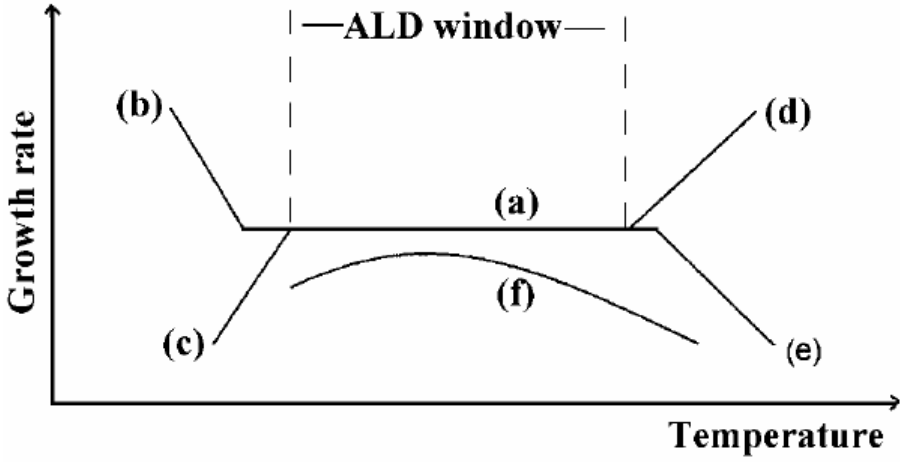

Figure 1.2 Scheme of (a) an ALD processing window limited by (b) precursor condensation, (c) insufficient reactivity, (d) precursor decomposition and (e) precursor desorption. If the deposition rate is dependent on the number of available reactive sites as in (f), actual ALD window cannot be observed.[10]

As a type of ALD, plasma enhanced ALD (PEALD), where plasma chemically activates one of the reactive species, deposits conformal and dense film with good electrical properties. Good dielectrics can be deposited by PEALD at low temperature (100 °C).[12] Also, PEALD expands ALD films to metal and its nitride films such as ruthenium[13] or tantalum nitride,[14,15] although it has conformality limitation especially on high aspect ratio structures caused by recombination of reactive radicals.[16] In addition, PEALD provides larger temperature window, high growth rate, and less purge time.[17] For example, ruthenium film grown by PEALD at 260 °C successfully acted as adhesion layer for copper interconnects.[12] Also, Mourey *et al.* fabricated high performance thin film transistor (TFT) with PEALD ZnO film deposited at 200 °C with high mobility.[18]

A variety of precursors available for ALD contributes to the rapid growth of ALD. Based on complicated surface chemistry, inorganic and metal organic from II–VI and III–V compounds (ZnS, GaAS, and CdS) to metal oxides (TiO_2, SiO_2, SnO_2, and ZnO) and nitrides (TiN, AlN, and GaN) have been widely studied at early ALD literature and for a while.[19] Precursors should satisfy several requirements. They should vaporize at lower temperature than the deposition temperature and react with the surface sites irreversibly and quickly to saturate the growth surface.[20] Also, byproducts after reaction should inert for the surface sites. As ALD reactants, many metal halides, metal alkyls, metal amides, and metal β-diketonates are satisfied these requirements.[21]

Compared to other film deposition techniques like thermal evaporation (~1000 °C)[22] or laser pulse deposition (450 °C),[23] ALD is low temperature process, which makes ALD process inexpensive and suitable for polymer, fibers, or biological substrates. Recently,

Al_2O_3, SiO_2, ZnO, and Co_3O_4 have been deposited at temperature as low as room temperature.[24-27] Lim *et al*. showed that N-doped ZnO ALD film was used as active channel layer in TFT instead of Si for transparent and flexible display.[28] While Si based TFT requires high process temperature (250 °C), TFT with N-doped ZnO film can fabricated at below 150 °C.

1.1.1 ALD on polymer films

ALD enables to coat thin films on polymer substrates because of low processing temperature. Different nucleation behaviors are also observed on a variety of polymer films. For example, Wilson et al. demonstrated that Al_2O_3 ALD at 85 °C showed different nucleation and growth depending on polymers.[29] Polystyrene (PS), polypropylene (PP), polymethyl methacrylate (PMMA), polyvinylchloride (PVC), and polyethylene (PE) showed different mass gain during the nucleation period which is generally 10 – 20 initial cycles after trimethylaluminum (TMA) exposure. Small and intermediate mass increase was measured on polyvinylchloride (PVC) and on polystyrene (PS), respectively, while polymethylmethacrylate (PMMA), polypropylene (PP) and polyethylene (PE) showed large mass gain. Similarly, they have various mass growth rates after nucleation, which are higher than that on unpolished quartz crystal microgravimetry (QCM) sensor. The authors explained that this resulted from different polymers' porosity and reactivity with the precursor. They proposed a model to explain how a diffusion layer forms within the near surface region (Figure 1.3).[29]

In addition to flat polymer surface, ALD film can be deposited on the patterned polymer film from PS-*b*-PMMA block copolymer.[30] Al_2O_3 and TiO_2 ALD on the polymer film results in the patterned nanostructure with tunable feature size and shapes after removing polymers at high temperature. It is possible because of selective and self-limited interaction for precursor like TMA or $TiCl_4$ with carboxyl group in PMMA.

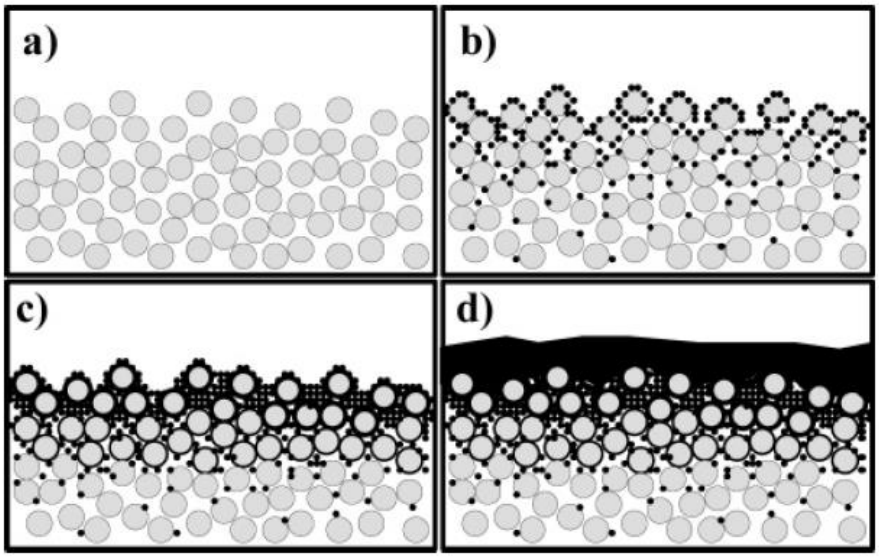

Figure 1.3 Model for Al_2O_3 ALD on polymer films showing (a) cross section of polymer film represented by loosely packed circles, (b) Al_2O_3 nucleation clusters forming from H_2O reaction with TMA trapped in the near surface region, (c) coalescence of Al_2O_3 clusters and closure of space between polymer chains, and (d) formation of dense Al_2O_3 film that grows on top of the polymer surface.[29]

1.1.2 ALD on bio-templates

Biology system provides various organic or inorganic 3D bio-templates.[31-35] In general, bio-templates are thermally weak so that low temperature ALD process is suitable to coat them. Moreover, thin film deposition of ALD in atomic range replicates their fine structure. Lee *at el*. demonstrated that eggshells as a bio-template can be coated with TiO_2 or ZnO at 70 °C and ZnO ALD of 100 cycles improves flexibility and thermal stability of eggshells.[26] Huang *at el*. obtained a replica of butterfly by Al_2O_3 ALD and showed optical properties of those replicas depend on the film thickness.[36] They also achieved efficient anti-reflections structure with Al_2O_3 ALD by replicating fine structures of fly eyes.[37] In addition, Mumm *at al*. fabricated highly ordered and aspect ratio (> 60,000) nanotubes with high chemical and thermal stability by Al_2O_3 coating on a spine of sea mouse.[38]

1.1.3 ALD on fibers

ALD is effective to evenly coat inorganic materials on 3D substrates such as nanotubes, photonic crystals, or fibers with high surface area.[39-41] Low growth temperatures in particular make ALD on fibers possible. As 3D substrates for ALD, organic or inorganic fibers have attracted interest because of their 3D structures and high surface area and applied for catalysts,[42] bio-adhesive,[43] and membranes.[44] Fibers, which have diverse uses in our lives, have high free volume such that precursors can penetrate into the substrate before formation of a diffusion barrier that blocks more penetration, resulting in modification of fibers' mechanical and chemical properties. Fiber substrates can be easily removed by calcination

leaving behind inorganic 3D structure. Kim at al. achieved free standing mats consisted of anatase TiO_2 submicrotubes by calcination poly(vinyl pyrrolidone) (PVP) fibers after TiO_2 ALD at 70 °C.[45] Peng et al. showed Al_2O_3 microtubes with controlled thickness using electrospun PVA microfiber.[39] Also, magnetic and photocatalytic nanotubes were obtained from electrospinning and calcination followed by ALD, where organic parts in electrospun fibers were removed and inorganic parts were oxidized to metal oxide.[46]

Natural or synthetic fibers can be substrates and affected by growth temperature and pulse pressure like flat substrates. On the other hand, film growth on fibers is very different from growth on planar substrate like polymer film. It depends on the type of fibers, and deposition temperature plays an important role in inorganic film growth. The surface activity with precursors decides the nucleation region during the first ALD cycles. For example, Al_2O_3 ALD at 60 °C on poly propylene fibers, which have no reactive functional group with trimethylaluminum (TMA), results in film growth at the surface showing distinct interface between fiber and Al_2O_3 film.[47] At higher temperature, 90 °C, on the other hand, TMA penetrates inside expanded fibrils so that nucleation and growth happen in near-surface region. (Figure 1.4) However, cotton fibers that have very reactive hydroxyl groups showed abrupt interface without a sub-surface growth at 80 °C. Sub-surface growth is also observed for poly amide 6 (PA6) fibers where amide bonding reacts with TMA.[48] While PA6 showed no strong dependence on deposition temperature, extended TMA dosing time produces thicker diffusion interface.

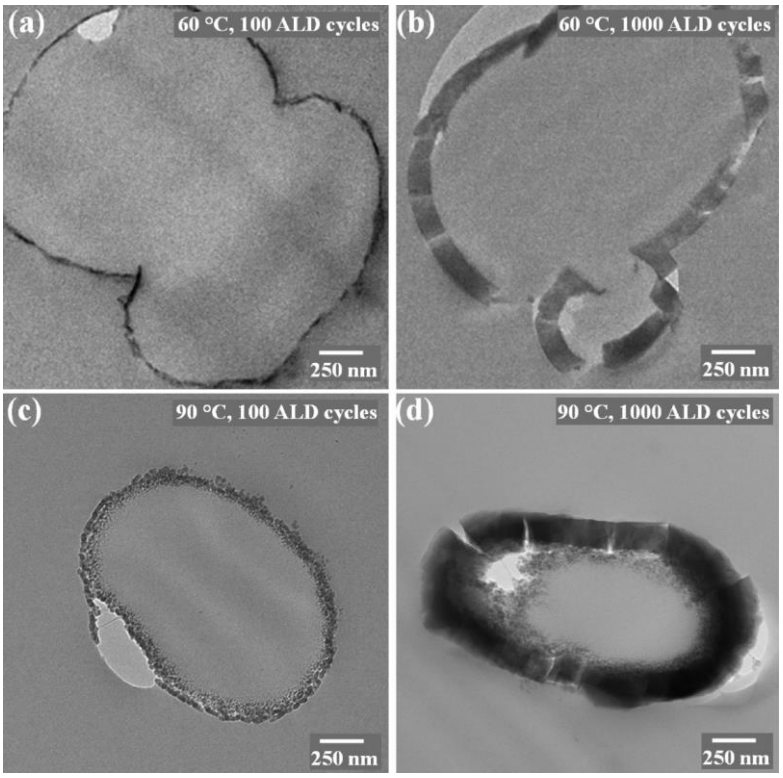

Figure 1.4 Cross sectional transmission electron microscopy images of polypropylene fibers extracted from a nonwoven fiber mat after processing with aluminum oxide ALD at 60 °C with (a) 100 and (b) 1000 ALD cycles, and at 90 °C with (c) 100 and (d) 1000 cycles.[47] Uniform surface modification is observed on all samples. Processing at 60 °C (panels a and b) show nearly uniform encapsulation of the polypropylene fiber surface. When deposition is performed at 90 °C, however, (panels c and d) intermixing between the oxide and the polypropylene is observed. The cracks in the coatings and voids in the polymer result from the microtome sample preparation.

ALD modifies mechanical or chemical properties of organic or inorganic fibers. For example, carbon fibers keep their high strength and modulus up to 2000 °C if no oxygen is present but they suffer from oxidation at high temperature with oxygen. Al_2O_3 ALD film provides cheaper and efficient way to prevent degradation compared to other methods such

as sol-gel techniques.[49] Also, mechanical properties of spider silk are improved by infiltrating precursors and by modifying molecular bonds from hydrogen bond to covalent bond.[50]

In addition, Hyde *et al*. found that wetting property of cotton and PP fiber mats significantly changes depending on the number of ALD cycles and deposition temperature.[51,52] Cotton fiber mats which are naturally hydrophilic rapidly changes to hydrophobic only with one cycle of Al_2O_3. It turns back to hydrophilic after ~10 cycles, and then wetting state keeps with longer ALD cycles. On the other hand, nonwoven PP fiber mats become hydrophilic after ~50 cycles of Al_2O_3 at 60 °C, while they stay hydrophobic after Al_2O_3 ALD at 90 °C. The difference in wetting transition between 60 °C and 90 °C is attributed to the precursor penetration and surface roughness. Since the PP fiber mats expand more at higher temperature, precursors can penetrate more deeply than at low temperature resulting in more sub-surface nucleation and growth that make the fiber mats rougher. Therefore PP fiber mats coated with Al_2O_3 at 90 °C stays in hydrophobicity according to metastable Cassie-Baxter model[8] but coating at 60 °C follows Wenzel model.[53]

1.2 Water splitting; principles and recent research

Solar energy is an inexhaustible, vast, and clean energy source. As fossil fuels like coal, petroleum, and natural gas are depleted while they produce excess greenhouse gases, demand for solar energy has grown rapidly. Solar energy cells convert light into electricity directly and have been widely studied to achieve higher efficiency. The maximum efficiency has continuously increased up to 40% for GaInP/GaInAs/Ge multijunction solar cells.[54] Also,

dye sensitized solar cell which is a kind of photochemical solar cells showed more than 12% efficiency[55] and organic solar cells with the efficiency of 12% was reported recently.[56] Although various solar cells including the common crystalline silicon solar cells are widely available commercially, low sunlight absorption and high fabrication costs make solar cells economically impractical for most users.[57-59]

Another solar energy conversion approach is photochemical water splitting to produce hydrogen and oxygen. Hydrogen gas is very light (0.08988 g/L) and has a higher energy density (~140 kJ/g) than any other fuels.[60] Furthermore, hydrogen gas emits no greenhouse gases and other pollutants from generation to end use if produced from solar energy. Hydrogen is used as a fuel for fuel cells, or as a reactant to produce liquid fuels. However, most hydrogen gas production currently relies on natural gas because of low efficiency of water splitting. Therefore, it is important to develop a solar-based water splitting process with a reasonable efficiency of at least 10%. Thermodynamic analysis indicates that splitting of water into gaseous hydrogen and oxygen requires an input of Gibbs free energy of 237 kJ/mol, so that a minimum potential of 1.23 eV/e is required to enable the reaction.[61] Although the photon energy from sunlight is enough to induce the reaction, water cannot absorb sufficient radiation from sunlight. Thus water splitting systems need to employ a photo-anode or photo-cathode to absorb photons and create electron-hole pairs. Since the separated electron should reduce hydrogen ion to gas at a cathode while the hole should oxidize water to form oxygen gas, the photo-electrode should employ a semiconductor with a conduction band higher in energy than the reduction potential of H_2O (E^o = 0 V) and the valence band lower than the oxidation potential of H_2O (E^o = 1.23 V).[62] Figure 1.5 shows

schematic illustration of water splitting with semiconductor catalysts and their band energy diagram, where conduction band and valence band cover water reduction and oxidation potential.[63] Furthermore the band gap of the semiconductor needs to be sufficiently small to ensure maximum absorption of visible light in the solar spectrum. In addition, the photo-electrode needs to be chemically stable under illumination.

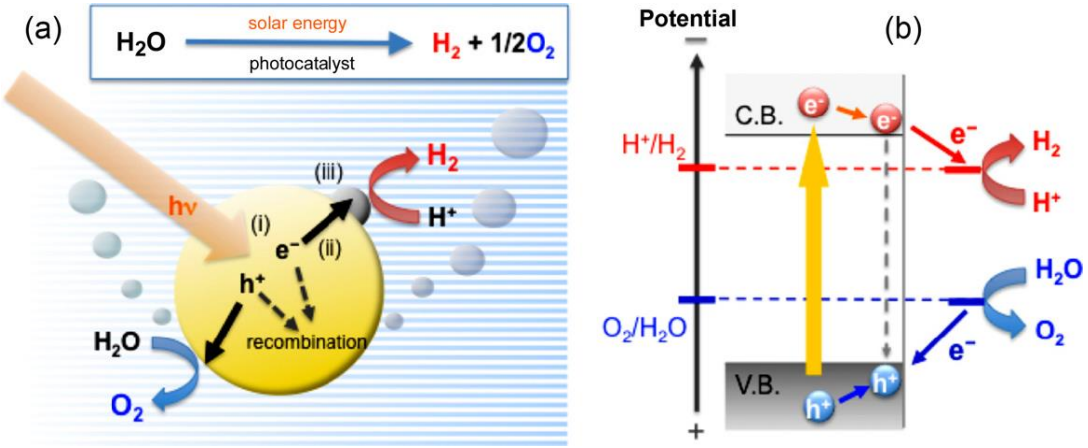

Figure 1.5 (a) Schematic illustration of water splitting over semiconductor photocatalyst and (b) its band energy diagram that spread over water oxidation and reduction potential.[63]

There are four types of water splitting systems that utilize a photoelectrode: 1) semiconductor solid state photovoltaic based systems; 2) direct semiconductor electrode structure; 3) sensitized semiconductor electrode systems; and, 4) homogeneous and microheterogeneous systems.[64] In semiconductor solid state photovoltaic based systems, p-n junction photovoltaic cells are connected with an electrolysis cell or immersed into water as an electrode and electricity generated by photovoltaic cells induces the electrolysis of water.

Although the quantum efficiency (production of fuel per absorbed photon) of 10% can be achieved with this system, making it competitive with other energy generation devices, the cost of produced hydrogen gas is not economical because of the high cost of photovoltaic cells. The most widely investigated system is the direct semiconductor electrode system where an n-type semiconductor functions as a photoanode, or p-type is used as a photocathode. Since Fujishima and Honda showed water photolysis with TiO_2 electrode in 1972,[65] TiO_2 has attracted interest as a photoanode in photoelectrochemical devices but its large band gap (3.0 eV for rutile phase and 3.2 eV for anatase phase) and low conduction band limit the efficiency and make it impractical.[66] To overcome these problems, dye sensitized semiconductors were introduced where a dye that can absorb more solar energy is attached onto the surface of the anode. The anode is often a layer of sintered TiO_2 particles. In this system, the overall efficiency (production of fuel over the entire range of incident photons) needs to be optimized relative to the anode thickness. If the dye/anode thickness is too thin, then not enough light is absorbed, whereas if the layer is too thick the photons can easily recombine resulting in low quantum efficiency. Lastly, homogeneous and micro heterogeneous systems which consist of sensitizer, catalysts, and charge accumulation sites provide high quantum efficiency for hydrogen gas evolution relative to other types of devices, focusing on a half reaction but typically not on true water splitting.[67] However, it is hard to satisfy all the requirements for the best efficiency in one.

To achieve higher efficiency, semiconductor materials for photoelectrode need to have a small band gap and balanced potential level. For many years, extensive research has been carried out on semiconductor materials such as ZrO_2, ZnO, Ta_2O_5 and TiO_2. In addition

to them, other transition or main group metal oxides such as $BiVO_4$, Bi_2WO_6, and In_2O_3 and metal sulfides such as CdS or ZnS also have been studied in recent works.[68] Figure 1.6 shows band gap energy of semiconductors relative to water oxidation and reduction.[69] Especially, TiO_2, which is the first photochemical catalyst for water splitting, has some merits as a photo electrode. For example, it is less expensive than other semiconductor materials and reactive with light. Moreover, TiO_2 has good chemical and photo chemical resistance in aqueous environment.[70]

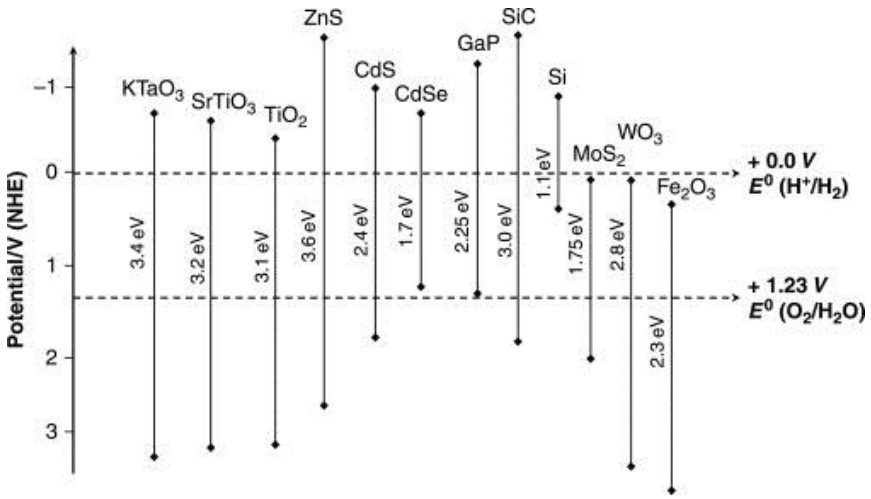

Figure 1.6 Band-gap energies and relative band positions of different semiconductors relative to the water oxidation/reduction potential vs NHE.[69]

Doping or compound with other semiconductor maximizes light absorption for semiconductor materials with narrow band gap like TiO_2.[71] For example, properties of TiO_2 are modified with doping of metal ions such as iron and copper, non-metals such as nitrogen, carbon, or boron, or metal oxides such as Nb_2O_5 or ZrO_2.[72-74] This is important in

photoelectrochemical devices to maximize solar energy absorption, since band gap of most semiconductor materials is larger than 3 eV which corresponds to wavelength less than visible light irradiation (> 420 nm). Thus, without doping, semiconductor materials mostly absorb UV light which is composed of only less than 4% of the solar energy while visible light is about 43% of solar energy cannot be used for water splitting leading to low solar efficiency.[75] Thus, many un-doped semiconductors cannot be used for water splitting due to low light collection. However, even with doping, there is no single material that can drive water splitting with a quantum efficiency larger than 10% only in the visible region of the sun spectrum. The maximum quantum efficiency under visible light is so far about 6% at 420 nm with $(Ga_{1-x}Zn_x)(N_{1-x}O_x)$ as a photocatalyst,[76] while the maximum efficiency (power out/power in) was reported as 12.4% using a monolithic photovoltaic-photoelectrochemical (PEC/PV) tandem cell to date.[77] And it is still a challenge to find the semiconductor materials or combination of them to maximize solar energy absorption and minimize energy losses.

1.2.1 Metal oxide nanosheets for water splitting

Two-dimensional nanosheets have attracted considerable attention in recent years as demands for nanoscale devices have increased due to their thickness in nanometer range, high crystallinity, and novel physical properties.[78] Graphene, which is a single atomic layer of graphite carbon, has been most widely studied in physics and electronics and synthesized by chemical vapor deposition or chemical reduction of graphite oxide since the first synthesis in 1987.[79-81] It has high crystallinity and remarkable electronic properties leading to various

applications such as nano-capacitors, batteries, or field emitters.[82,83] For example, its semiconducting gap can be tuned to ~0.3 eV in bilayer graphene and its charge carrier mobility as high as 15,000 $cm^2 V^{-1} S^{-1}$ can be explained with the Dirac equation, not with the Schrödinger equation usually applied to quantum particles.[84] In addition to graphene, various transition metal oxides can be exfoliated into nanosheets from layered compounds. For example, nanosheets of Ti oxides, Mn oxides, Ti-Nb oxides, or Ru oxides can be dispersed in a colloidal suspension after delamination with negative charges. They are suitable for nanostructure multilayer films through restacking and combining with other ionic materials. These composite films have no interface damage that happens in other physical methods.[85,86] Although the delamination from layered structure is mostly developed, other techniques such as aqueous-phase synthesis, hydrothermal growth, and thermal evaporation have been widely used for fabrication of nanosheets.[87-90]

A variety of nanosheets and their composites have unique electronic, spin-electronic, and magnetic properties, which make nanosheets promising candidates for nanoelectronics or photoelectronics. For example, titania nanosheets have received special attention due to their photochemical properties such as photo-induced hydrophilic conversion and photocatalytic oxidation.[91-93] Wang *et al*. showed that a glass coated with titania polycrystalline film has a water contact angle of 0° under UV irradiation but it showed a hydrophobic surface after removing the UV source.[94] Also, Shibata *et al*. demonstrated that titania decomposes organic substances as a photocatalyst when exposed to UV so it is promising for water splitting.[95] In addition, ZnO nanosheets which have large exciton binding energy and wide band gap showed a potential application in electro-optical devices.[56,96] $HCa_2Nb_3O_{10}$, $Ba_5Ta_4O_{15}$, and

$BiVO_4$ nasnosheets also have showed photocatalytic effects.[97-99] Moreover, hybrid nanosheets that is polymer layers combined with inorganic materials have attracted interest recently because of their flexibility and robustness,[100-103]

Nanosheets have advantages for water splitting with high surface area, shorter diffusion length, and low reflectivity.[104] Compton *et al.* showed that $Ca_2Nb_3O_{10}$ nanosheets split water into hydrogen and hydrogen peroxide under UV light.[105] Also, Yu *et al*. demonstrated the synergistic effect of (0 0 1) facets of TiO_2 nanosheet with Pt nanoparticles and surface fluorination for water splitting.[106] In addition, graphene with CdS clusters,[107] N-doped $La_2Ti_2O_7$ nanosheets,[108] and CdS/ZnS porous nanosheets[109] produce hydrogen from water splitting under UV or visible light.

ALD has merits over other nanosheet fabrication techniques if the separation from the substrate and collection of released nanosheets are successfully done, because thickness can be controlled precisely in the nanometer range and chemical composition can be varied with diverse precursors. Furthermore, it is easy to grow multiple layers with different metal oxides by successive ALD such that ALD can be used for fabrication of p-n junction as well as single material photocatalysts. Therefore, nanosheets fabricated by ALD are expected to work as photocatalysts in dye decomposition or water splitting system.

1.3 Summary

ALD is an efficient technique to deposit conformal and uniform films. In particular, many 3D structures which normally have a difficulty in uniform coating can be coated with

various kinds of inorganic or metal-organic films. Since ALD is performed at lower temperature relative to other techniques like thermal evaporations, it is useful for thermally weak substrates including polymer film, fibers, and bio-templates, where the nucleation and growth depend on the substrates, deposition temperature, and the number of cycles. ALD can change the surface properties of the substrates like wetting properties by the interaction between functional groups of the substrate and precursors. Also, ALD can be employed for 2D-nanosheets fabrication by being released from the appropriate sacrificial layers. It has advantages of precise thickness control and chemical composition compared to previous nanosheet fabrication. Furthermore, successive ALD produces multilayer nanosheets which act as p-n junctions expected to be applied for water splitting effectively.

References

(1) Suntola, T.; Antson, J. Method for producing compound thin films. US 4,058,430 (**1977**).

(2) Parsons, G. N.; George, S. M.; Knez, M. Progress and future directions for atomic layer deposition and ALD-based chemistry. *MRS Bull.* **2011,** 36, 865.

(3) George, S. M. Atomic layer deposition: an overview. *Chem. Rev.* **2009,** 110, 111.

(4) Knez, M.; Nielsch, K.; Niinistö, L. Synthesis and surface engineering of complex nanostructures by atomic layer deposition. *Adv. Mater.* **2007,** 19, 3425.

(5) Lin, H.-C.; Wang, W.-E.; Brammertz, G.; Meuris, M.; Heyns, M. Electrical study of sulfur passivated $In_{0.53}Ga_{0.47}As$ MOS capacitor and transistor with ALD Al_2O_3 as gate insulator. *Microelectron. Eng.* **2009,** 86, 1554.

(6) Biercuk, M.; Monsma, D.; Marcus, C.; Becker, J.; Gordon, R. Low-temperature atomic-layer-deposition lift-off method for microelectronic and nanoelectronic applications. *Appl. Phys. Lett.* **2003,** 83, 2405.

(7) Ritala, M.; Niinisto, J., Chapter 4 Atomic Layer Deposition. In *Chemical Vapour Deposition: Precursors*, The Royal Society of Chemistry: 2009; pp 158.

(8) Cassie, A. B. D.; Baxter, S. Wettability of porous surfaces. *Trans. Faraday Soc.* **1944,** 40, 546.

(9) Suntola, T.; Pakkala, A. J.; Lindfors, S. G. Method for performing growth of compound thin films US 4,413,022 (**1983**).

(10) Niinistö, L.; Nieminen, M.; Päiväsaari, J.; Niinistö, J.; Putkonen, M. Advanced electronic and optoelectronic materials by Atomic Layer Deposition: An overview with

special emphasis on recent progress in processing of high-k dielectrics and other oxide materials. *Phys. Status Solidi A* **2004,** 201, 1443.

(11) Guziewicz, E.; Godlewski, M.; Krajewski, T.; Szczepanik, A.; Kopalko, K.; Wójcik-Głodowska, A.; Przeździecka, E.; Paszkowicz, W.; Łusakowska, E.; Kruszewski, P. ZnO grown by atomic layer deposition: A material for transparent electronics and organic heterojunctions. *J. Appl. Phys.* **2009,** 105, 122413.

(12) Lim, J. W.; Yun, S. J. Electrical properties of alumina films by plasma-enhanced atomic layer deposition. *Electrochem. Solid-State Lett.* **2004,** 7, F45.

(13) Xie, Q.; Jiang, Y.-L.; Musschoot, J.; Deduytsche, D.; Detavernier, C.; Van Meirhaeghe, R. L.; Van den Berghe, S.; Ru, G.-P.; Li, B.-Z.; Qu, X.-P. Ru thin film grown on TaN by plasma enhanced atomic layer deposition. *Thin Solid Films* **2009,** 517, 4689.

(14) Park, J.-S.; Lee, M.-J.; Lee, C.-S.; Kang, S.-W. Plasma-enhanced atomic layer deposition of tantalum nitrides using hydrogen radicals as a reducing agent. *Electrochem. Solid-State Lett.* **2001,** 4, C17.

(15) Park, J.-S.; Park, H.-S.; Kang, S.-W. Plasma-enhanced atomic layer deposition of Ta-N thin films. *J. Electrochem. Soc.* **2002,** 149, C28.

(16) Knoops, H. C. M.; Langereis, E.; van de Sanden, M. C. M.; Kessels, W. M. M. Conformality of plasma-assisted ALD: Physical processes and modeling. *J. Electrochem. Soc.* **2010,** 157, G241.

(17) Heil, S.; Van Hemmen, J.; Hodson, C.; Singh, N.; Klootwijk, J.; Roozeboom, F.; Van de Sanden, M.; Kessels, W. Deposition of TiN and HfO in a commercial 200 mm remote plasma atomic layer deposition reactor. *J. Vac. Sci. Technol. A* **2007,** 25, 1357.

(18) Mourey, D. A.; Zhao, D. A.; Sun, J.; Jackson, T. N. Fast PEALD ZnO thin-film transistor circuits. *Electron Devices, IEEE Transactions on* **2010,** 57, 530.

(19) Leskelä, M.; Ritala, M. Atomic layer deposition (ALD): from precursors to thin film structures. *Thin Solid Films* **2002,** 409, 138.

(20) Miikkulainen, V.; Leskela, M.; Ritala, M.; Puurunen, R. L. Crystallinity of inorganic films grown by atomic layer deposition: Overview and general trends. *J. Appl. Phys.* **2013,** 113, 021301.

(21) Puurunen, R. L. Surface chemistry of atomic layer deposition: A case study for the trimethylaluminum/water process. *J. Appl. Phys.* **2005,** 97, 121301.

(22) Dai, Z. R.; Pan, Z. W.; Wang, Z. L. Novel nanostructures of functional oxides synthesized by thermal evaporation. *Adv. Funct. Mater.* **2003,** 13, 9.

(23) Yun, K. Y.; Noda, M.; Okuyama, M. Prominent ferroelectricity of $BiFeO_3$ thin films prepared by pulsed-laser deposition. *Appl. Phys. Lett.* **2003,** 83, 3981.

(24) Ferguson, J. D.; Smith, E. R.; Weimer, A. W.; George, S. M. ALD of SiO_2 at room temperature using TEOS and H_2O with NH_3 as the catalyst. *J. Electrochem. Soc.* **2004,** 151, G528.

(25) Groner, M. D.; Fabreguette, F. H.; Elam, J. W.; George, S. M. Low-temperature Al_2O_3 atomic layer deposition. *Chem. Mater.* **2004,** 16, 639.

(26) Lee, S.-M.; Grass, G.; Kim, G.-M.; Dresbach, C.; Zhang, L.; Gösele, U.; Knez, M. Low-temperature ZnO atomic layer deposition on biotemplates: flexible photocatalytic ZnO structures from eggshell membranes. *Phys. Chem. Chem. Phys.* **2009,** 11, 3608.

(27) Han, B.; Choi, K. H.; Park, K.; Han, W. S.; Lee, W.-J. Low-temperature atomic layer deposition of cobalt oxide thin films using dicobalt hexacarbonyl tert-butylacetylene and ozone. *Electrochem. Solid-State Lett.* **2011,** 15, D14.

(28) Lim, S.; Kwon, S.-j.; Kim, H.; Park, J.-S. High performance thin film transistor with low temperature atomic layer deposition nitrogen-doped ZnO. *Appl. Phys. Lett.* **2007,** 91, 183517.

(29) Wilson, C. A.; Grubbs, R. K.; George, S. M. Nucleation and growth during Al_2O_3 atomic layer deposition on polymers. *Chem. Mater.* **2005,** 17, 5625.

(30) Peng, Q.; Tseng, Y. C.; Darling, S. B.; Elam, J. W. Nanoscopic patterned materials with tunable dimensions via atomic layer deposition on block copolymers. *Adv. Mater.* **2010,** 22, 5129.

(31) Seshadri, R.; Meldrum, F. C. Bioskeletons as templates for ordered, macroporous structures. *Adv. Mater.* **2000,** 12, 1149.

(32) Chia, S. Y.; Urano, J.; Tamanoi, F.; Dunn, B.; Zink, J. I. Patterned hexagonal arrays of living cells in sol-gel silica films. *J. Am. Chem. Soc.* **2000,** 122, 6488.

(33) Li, D.; Qu, X. W.; Newton, S. M. C.; Klebba, P. E.; Mao, C. B. Morphology-controlled synthesis of silica nanotubes through pH- and sequence-responsive morphological change of bacterial flagellar biotemplates. *J. Mater. Chem.* **2012,** 22, 15702.

(34) Knez, M.; Bittner, A. M.; Boes, F.; Wege, C.; Jeske, H.; Maiss, E.; Kern, K. Biotemplate synthesis of 3-nm nickel and cobalt nanowires. *Nano Lett.* **2003,** 3, 1079.

(35) Yamashita, I.; Hayashi, J.; Hara, M. Bio-template synthesis of uniform CdSe nanoparticles using cage-shaped protein, apoferritin. *Chem. Lett.* **2004,** 33, 1158.

(36) Huang, J.; Wang, X.; Wang, Z. L. Controlled replication of butterfly wings for achieving tunable photonic properties. *Nano Lett.* **2006,** 6, 2325.

(37) Huang, J. Y.; Wang, X. D.; Wang, Z. L. Bio-inspired fabrication of antireflection nanostructures by replicating fly eyes. *Nanotechnology* **2008,** 19.

(38) Mumm, F.; Kemell, M.; Leskela, M.; Sikorski, P. A bio-originated porous template for the fabrication of very long, inorganic nanotubes and nanowires. *Bioinspir. Biomim.* **2010,** 5.

(39) Peng, Q.; Sun, X. Y.; Spagnola, J. C.; Hyde, G. K.; Spontak, R. J.; Parsons, G. N. Atomic layer deposition on electrospun polymer fibers as a direct route to Al_2O_3 microtubes with precise wall thickness control. *Nano Lett.* **2007,** 7, 719.

(40) Herrmann, C. F.; Fabreguette, F. H.; Finch, D. S.; Geiss, R.; George, S. M. Multilayer and functional coatings on carbon nanotubes using atomic layer deposition. *Appl. Phys. Lett.* **2005,** 87.

(41) Lee, J. H.; Leung, W.; Ahn, J.; Lee, T.; Park, I. S.; Constant, K.; Ho, K. M. Layer-by-layer photonic crystal fabricated by low-temperature atomic layer deposition. *Appl. Phys. Lett.* **2007,** 90.

(42) Kemell, M.; Pore, V.; Ritala, M.; Leskelä, M.; Lindén, M. Atomic layer deposition in nanometer-level replication of cellulosic substances and preparation of photocatalytic TiO_2/cellulose composites. *J. Am. Chem. Soc.* **2005,** 127, 14178.

(43) Hyde, G.; McCullen, S.; Jeon, S.; Stewart, S.; Jeon, H.; Loboa, E.; Parsons, G. Atomic layer deposition and biocompatibility of titanium nitride nano-coatings on cellulose fiber substrates. *Biomed. Mater.* **2009,** 4, 025001.

(44) Cameron, M.; Gartland, I.; Smith, J.; Diaz, S.; George, S. Atomic layer deposition of SiO_2 and TiO_2 in alumina tubular membranes: Pore reduction and effect of surface species on gas transport. *Langmuir* **2000,** 16, 7435.

(45) Kim, G.-M.; Lee, S.-M.; Michler, G.; Roggendorf, H.; Gosele, U.; Knez, M. Nanostructured pure anatase titania tubes replicated from electrospun polymer fiber templates by atomic layer deposition. *Chem. Mater.* **2008,** 20, 3085.

(46) Santala, E.; Kemell, M.; Leskelä, M.; Ritala, M. The preparation of reusable magnetic and photocatalytic composite nanofibers by electrospinning and atomic layer deposition. *Nanotechnology* **2009,** 20, 035602.

(47) Jur, J. S.; Spagnola, J. C.; Lee, K.; Gong, B.; Peng, Q.; Parsons, G. N. Temperature-dependent subsurface growth during atomic layer deposition on polypropylene and cellulose fibers. *Langmuir* **2010,** 26, 8239.

(48) Spagnola, J. C.; Gong, B.; Arvidson, S. A.; Jur, J. S.; Khan, S. A.; Parsons, G. N. Surface and sub-surface reactions during low temperature aluminium oxide atomic layer deposition on fiber-forming polymers. *J. Mater. Chem.* **2010,** 20, 4213.

(49) Roy, A.; Baumann, W.; König, I.; Baumann, G.; Schulze, S.; Hietschold, M.; Mäder, T.; Nestler, D.; Wielage, B.; Goedel, W. Atomic layer deposition (ALD) as a coating tool for reinforcing fibers. *Anal. Bioanal. Chem.* **2010,** 396, 1913.

(50) Lee, S. M.; Pippel, E.; Gosele, U.; Dresbach, C.; Qin, Y.; Chandran, C. V.; Brauniger, T.; Hause, G.; Knez, M. Greatly increased toughness of infiltrated spider silk. *Science* **2009,** 324, 488.

(51) Hyde, G. K.; Park, K. J.; Stewart, S. M.; Hinestroza, J. P.; Parsons, G. N. Atomic layer deposition of conformal inorganic nanoscale coatings on three-dimensional natural fiber systems: effect of surface topology on film growth characteristics. *Langmuir* **2007,** 23, 9844.

(52) Hyde, G. K.; Scarel, G.; Spagnola, J. C.; Peng, Q.; Lee, K.; Gong, B.; Roberts, K. G.; Roth, K. M.; Hanson, C. A.; Devine, C. K. Atomic layer deposition and abrupt wetting transitions on nonwoven polypropylene and woven cotton fabrics. *Langmuir* **2009,** 26, 2550.

(53) Wenzel, R. N. Resistance of solid surfaces to wetting by water. *Ind. Eng. Chem.* **1936,** 28, 988.

(54) King, R.; Law, D.; Edmondson, K.; Fetzer, C.; Kinsey, G.; Yoon, H.; Sherif, R.; Karam, N. 40% efficient metamorphic GaInP/GaInAs/Ge multijunction solar cells. *Appl. Phys. Lett.* **2007,** 90, 183516.

(55) Yella, A.; Lee, H.-W.; Tsao, H. N.; Yi, C.; Chandiran, A. K.; Nazeeruddin, M. K.; Diau, E. W.-G.; Yeh, C.-Y.; Zakeeruddin, S. M.; Grätzel, M. Porphyrin-sensitized solar cells with cobalt (II/III)–based redox electrolyte exceed 12 percent efficiency. *Science* **2011,** 334, 629.

(56) Chen, S. J.; Liu, Y. C.; Shao, C. L.; Mu, R.; Lu, Y. M.; Zhang, J. Y.; Shen, D. Z.; Fan, X. W. Structural and optical properties of uniform ZnO nanosheets. *Adv. Mater.* **2005,** 17, 586.

(57) Chen, L. M.; Hong, Z. R.; Li, G.; Yang, Y. Recent progress in polymer solar cells: manipulation of polymer: fullerene morphology and the formation of efficient inverted polymer solar cells. *Adv. Mater.* **2009,** 21, 1434.

(58) Wang, X.; Zhi, L. J.; Mullen, K. Transparent, conductive graphene electrodes for dye-sensitized solar cells. *Nano Lett.* **2008,** 8, 323.

(59) King, R. R.; Law, D. C.; Edmondson, K. M.; Fetzer, C. M.; Kinsey, G. S.; Yoon, H.; Sherif, R. A.; Karam, N. H. 40% efficient metamorphic GaInP/GaInAs/Ge multijunction solar cells. *Appl. Phys. Lett.* **2007,** 90.

(60) Li, Y.; Zhang, J. Hydrogen generation from photoelectrochemical water splitting based on nanomaterials. *Laser Photon. Rev.* **2010,** 4, 517.

(61) Tomkiewicz, M.; Fay, H. Photoelectrolysis of water with semiconductors. *Appl. Phys. A: Mater. Sci. Process.* **1979,** 18, 1.

(62) Sayama, K.; Arakawa, H. Photocatalytic decomposition of water and photocatalytic reduction of carbon dioxide over zirconia catalyst. *J. Phys. Chem.* **1993,** 97, 531.

(63) Abe, R. Recent progress on photocatalytic and photoelectrochemical water splitting under visible light irradiation. *J. Photochem. Photobiol. C* **2010,** 11, 179.

(64) Bard, A. J.; Fox, M. A. Artificial photosynthesis - Solar splitting of water to hydrogen and oxygen. *Acc. Chem. Res.* **1995,** 28, 141.

(65) Fujishima, A.; Honda, K. Electrochemical photolysis of water at a semiconductor electrode. *Nature* **1972,** 238, 37.

(66) Bendavid, A.; Martin, P. J.; Jamting, A.; Takikawa, H. Structural and optical properties of titanium oxide thin films deposited by filtered arc deposition. *Thin Solid Films* **1999,** 356, 6.

(67) Grätzel, M.; Jørgensen, C.; Kalyanasundaram, K.; Kiwi, J.; Reisfeld, R.; Tributsch, H.; Kiwi, J.; Kalyanasundaram, K.; Grätzel, M., Visible light induced cleavage of water into hydrogen and oxygen in colloidal and microheterogeneous systems. In *Solar Energy Materials*, Springer Berlin / Heidelberg: 1982; Vol. 49, pp 37.

(68) Osterloh, F. E. Inorganic materials as catalysts for photochemical splitting of water. *Chem. Mater.* **2008,** 20, 35.

(69) Navarro, R.; Del Valle, F.; Villoria de la Mano, J.; Álvarez-Galván, M.; Fierro, J. Photocatalytic water splitting under visible light: Concept and catalysts development. *Adv. Chem. Eng.* **2009,** 36, 111.

(70) Nowotny, J.; Sorrell, C. C.; Bak, T.; Sheppard, L. R. Solar-hydrogen: unresolved problems in solid-state science. *Solar Energy* **2005,** 78, 593.

(71) Kudo, A.; Miseki, Y. Heterogeneous photocatalyst materials for water splitting. *Chem. Soc. Rev.* **2009,** 38, 253.

(72) Park, J. H.; Kim, S.; Bard, A. J. Novel carbon-doped TiO_2 nanotube arrays with high aspect ratios for efficient solar water splitting. *Nano Lett.* **2005,** 6, 24.

(73) Diwald, O.; Thompson, T. L.; Zubkov, T.; Walck, S. D.; Yates, J. T. Photochemical activity of nitrogen-doped rutile TiO_2(110) in visible light. *J. Phys. Chem. B* **2004,** 108, 6004.

(74) Gombac, V.; De Rogatis, L.; Gasparotto, A.; Vicario, G.; Montini, T.; Barreca, D.; Balducci, G.; Fornasiero, P.; Tondello, E.; Graziani, M. TiO_2 nanopowders doped with boron and nitrogen for photocatalytic applications. *Chem. Phys.* **2007,** 339, 111.

(75) Zou, Z.; Ye, J.; Sayama, K.; Arakawa, H. Direct splitting of water under visible light irradiation with an oxide semiconductor photocatalyst. *Nature* **2001,** 414, 625.

(76) Maeda, K.; Teramura, K.; Domen, K. Effect of post-calcination on photocatalytic activity of $(Ga_{1-x}Zn_x)(N_{1-x}O_x)$ solid solution for overall water splitting under visible light. *J. Catal.* **2008,** 254, 198.

(77) Khaselev, O.; Turner, J. A. A monolithic photovoltaic-photoelectrochemical device for hydrogen production via water splitting. *Science* **1998,** 280, 425.

(78) Sasaki, T.; Ebina, Y.; Tanaka, T.; Harada, M.; Watanabe, M.; Decher, G. Layer-by-layer assembly of titania nanosheet/polycation composite films. *Chem. Mater* **2001,** 13, 4661.

(79) Mouras; S; Hamm; A; Djurado; D; Cousseins; J, C., *Synthesis of first stage graphite intercalation compounds with fluorides.* Gauthier-Villars: Paris, France, 1987; Vol. 24.

(80) Chae, S. J.; Gunes, F.; Kim, K. K.; Kim, E. S.; Han, G. H.; Kim, S. M.; Shin, H. J.; Yoon, S. M.; Choi, J. Y.; Park, M. H.; Yang, C. W.; Pribat, D.; Lee, Y. H. Synthesis of large-area graphene layers on poly-nickel substrate by chemical vapor deposition: wrinkle formation. *Adv. Mater.* **2009,** 21, 2328.

(81) Stankovich, S.; Dikin, D. A.; Piner, R. D.; Kohlhaas, K. A.; Kleinhammes, A.; Jia, Y.; Wu, Y.; Nguyen, S. T.; Ruoff, R. S. Synthesis of graphene-based nanosheets via chemical reduction of exfoliated graphite oxide. *Carbon* **2007,** 45, 1558.

(82) Lewandowski, A.; Galinski, M. Practical and theoretical limits for electrochemical double-layer capacitors. *J. Power Sources* **2007,** 173, 822.

(83) Geim, A. K. Graphene: status and prospects. *Science* **2009,** 324, 1530.

(84) Geim, A. K.; Novoselov, K. S. The Rise of graphene. *Nat. Mater.* **2007,** 6, 183.

(85) Osada, M.; Sasaki, T. Exfoliated oxide nanosheets: new solution to nanoelectronics. *J. Mater. Chem.* **2009,** 19, 2503.

(86) Izawa, K.; Yamada, T.; Unal, U.; Ida, S.; Altuntasoglu, O.; Koinuma, M.; Matsumoto, Y. Photoelectrochemical oxidation of methanol on oxide nanosheets. *J. Phys. Chem. B* **2006,** 110, 4645.

(87) Yu, T.; Lim, B.; Xia, Y. N. Aqueous-phase synthesis of single-crystal ceria nanosheets. *Angew. Chem. Int. Ed.* **2010,** 49, 4484.

(88) Wang, W. W.; Zhu, Y. J.; Yang, L. X. ZnO-SnO_2 hollow spheres and hierarchical nanosheets: hydrothermal preparation, formation mechanism, and photocatalytic properties. *Adv. Funct. Mater.* **2007,** 17, 59.

(89) Dai, Z. R.; Pan, Z. W.; Wang, Z. L. Gallium oxide nanoribbons and nanosheets. *J. Phys. Chem. B* **2002,** 106, 902.

(90) Miyamoto, N.; Yamamoto, H.; Kaito, R.; Kuroda, K. Formation of extraordinarily large nanosheets from $K_4Nb_6O_{17}$ crystals. *Chem. Commun.* **2002**, 2378.

(91) Sakai, N.; Ebina, Y.; Takada, K.; Sasaki, T. Electronic band structure of titania semiconductor nanosheets revealed by electrochemical and photoelectrochemical studies. *J. Am. Chem. Soc.* **2004,** 126, 5851.

(92) Marani, D.; D'Epifanio, A.; Traversa, E.; Miyayama, M.; Licoccia, S. Titania nanosheets (TNS)/sulfonated poly ether ether ketone (SPEEK) nanocomposite proton exchange membranes for fuel cells. *Chem. Mater.* **2009,** 22, 1126.

(93) Wang, L.; Sasaki, T.; Ebina, Y.; Kurashima, K.; Watanabe, M. Fabrication of controllable ultrathin hollow shells by layer-by-layer assembly of exfoliated titania nanosheets on polymer templates. *Chem. Mater.* **2002,** 14, 4827.

(94) Wang, R.; Hashimoto, K.; Fujishima, A.; Chikuni, M.; Kojima, E.; Kitamura, A.; Shimohigoshi, M.; Watanabe, T. Light-Induced amphiphilic surfaces. *Nature* **1997,** 388, 431.

(95) Shibata, T.; Sakai, N.; Fukuda, K.; Ebina, Y.; Sasaki, T. Photocatalytic properties of titania nanostructured films fabricated from titania nanosheets. *Phys. Chem. Chem. Phys.* **2007,** 9, 2413.

(96) Hu, J. Q.; Bando, Y.; Zhan, J. H.; Li, Y. B.; Sekiguchi, T. Two-dimensional micrometer-sized single-crystalline ZnO thin nanosheets. *Appl. Phys. Lett.* **2003,** 83, 4414.

(97) Maeda, K.; Eguchi, M.; Lee, S. H. A.; Youngblood, W. J.; Hata, H.; Mallouk, T. E. Photocatalytic hydrogen evolution from hexaniobate nanoscrolls and calcium niobate nanosheets sensitized by ruthenium(II) bipyridyl complexes. *J. Phys. Chem. C* **2009,** 113, 7962.

(98) Zhang, L.; Chen, D. R.; Jiao, X. L. Monoclinic structured $BiVO_4$ nanosheets: hydrothermal preparation, formation mechanism, and coloristic and photocatalytic properties. *J. Phys. Chem. B* **2006,** 110, 2668.

(99) Xu, T. G.; Zhang, C.; Shao, X.; Wu, K.; Zhu, Y. F. Monomolecular-layer $Ba_5Ta_4O_{15}$ nanosheets: synthesis and investigation of photocatalytic properties. *Adv. Funct. Mater.* **2006,** 16, 1599.

(100) Okamura, Y.; Kabata, K.; Kinoshita, M.; Saitoh, D.; Takeoka, S. Free-standing biodegradable poly(lactic acid) nanosheet for sealing operations in surgery. *Adv. Mater.* **2009,** 21, 4388.

(101) Endo, H.; Kado, Y.; Mitsuishi, M.; Miyashita, T. Fabrication of free-standing hybrid nanosheets organized with polymer Langmuir−Blodgett films and gold nanoparticles. *Macromolecules* **2006,** 39, 5559.

(102) Vendamme, R.; Onoue, S.-Y.; Nakao, A.; Kunitake, T. Robust free-standing nanomembranes of organic/inorganic interpenetrating networks. *Nat. Mater.* **2006,** 5, 494.

(103) Li, J.; Xu, Y.; Wu, D.; Sun, Y. Hydrothermal synthesis of novel sandwich-like structured ZnS/octylamine hybrid nanosheets. *Solid State Commun.* **2004,** 130, 619.

(104) Yang, X.; Wolcott, A.; Wang, G.; Sobo, A.; Fitzmorris, R. C.; Qian, F.; Zhang, J. Z.; Li, Y. Nitrogen-doped ZnO nanowire arrays for photoelectrochemical water splitting. *Nano Lett.* **2009,** 9, 2331.

(105) Compton, O. C.; Osterloh, F. E. Niobate nanosheets as catalysts for photochemical water splitting into hydrogen and hydrogen peroxide. *J. Phys. Chem. C* **2008,** 113, 479.

(106) Yu, J.; Qi, L.; Jaroniec, M. Hydrogen production by photocatalytic water splitting over Pt/TiO_2 nanosheets with exposed (001) facets. *J. Phys. Chem. C* **2010,** 114, 13118.

(107) Li, Q.; Guo, B.; Yu, J.; Ran, J.; Zhang, B.; Yan, H.; Gong, J. R. Highly efficient visible-light-driven photocatalytic hydrogen production of CdS-cluster-decorated graphene nanosheets. *J. Am. Chem. Soc.* **2011,** 133, 10878.

(108) Meng, F.; Hong, Z.; Arndt, J.; Li, M.; Zhi, M.; Yang, F.; Wu, N. Visible light photocatalytic activity of nitrogen-doped $La_2Ti_2O_7$ nanosheets originating from band gap narrowing. *Nano Research* **2012,** 5, 213.

(109) Zhang, J.; Yu, J.; Zhang, Y.; Li, Q.; Gong, J. R. Visible light photocatalytic H_2-production activity of CuS/ZnS porous nanosheets based on photoinduced interfacial charge transfer. *Nano Lett.* **2011,** 11, 4774.

Chapter 2

ALD Process and Analysis Tools

2.1 ALD rector

Atomic layer deposition was performed in a custom hot wall viscous flow tube reactor with stainless steel tube with inner diameter of 1.35 inch. Precursors were trimethylaluminum (TMA, 98%), diethylzinc (DEZ, 95%), and titanium tetrachloride ($TiCl_4$, 99%) for Al_2O_3, ZnO, and TiO_2, respectively with deionized (DI) water as co-reactant. All precursors were purchased from Strem Chemicals, Inc. and used as received. Each precursor was dosed alternatively with DI water at an operating pressure of 2 Torr. High purity argon or nitrogen was used as a carrier and purge gas, and they were purified before use with an inert gas filter (Gatekeeper®, Entegris Inc.). ALD sequences are consisted of [TMA/purge/H_2O/purge] = [1/30/1/60 s] and [DEZ/purge/H_2O/purge] = [2/50/2/50 s] for Al_2O_3 and ZnO coatings, respectively. The process temperature was fixed at 60 or 90 °C for Al_2O_3 and ZnO ALD. Under these conditions, the growth rate of the Al_2O_3 and ZnO on a planar silicon wafer was measured to be 1.2 – 1.3 and 1.5 – 1.7 Å/cycle, respectively, consistent with well-defined atomic layer deposition.[1,2] The sequence for TiO_2 is [$TiCl_4$/purge/H_2O/purge] = [1/40/1/40 s] at 100 °C and the growth rate is ~0.4 Å/cycle. The partial pressure of each precursor is 0.1 – 0.2 Torr for Al_2O_3 and ZnO while 0.01 – 0.02 Torr for TiO_2.

2.2 Spectroscopic Ellipsometry

Thickness of single or multilayers was measured using spectroscopic ellipsometry (Alpha-SE Ellipsometer, JA Woollam Co., Inc.). It detects a change in polarized light with

reflection on the surface or transmittance by the surface.[3] ALD film on Si/SiO_2 wafer was used for film thickness measurement as a reference for every ALD run.

2.3 Contact angle goniometer

Contact angle goniometer (Rame-Hart, Inc., model 200-F1) provides contact angle between substrate and water drop. In general, the contact angle less than 90° is considered as hydrophilic with high surface free energy that means a solid substrate has good adhesion and wettability. On the other hand, the substrate with the contact angle larger than 90° is hydrophilic with low surface free energy as well as poor adhesion and wettability. There are two models to explain contact angles, Wenzel[4] and Cassie-Baxter model.[5] Wenzel model explains hydrophobicity on the homogeneous surface and Cassie-Baxter model is applied to the heterogeneous surface.

There are two types of contact angle measurement, static and dynamic contact angles that is composed of advancing and receding contact angles. When the volume of liquid drop is increasing, advancing contact angle is obtained.[6] On the contrary, receding contact angle is measured during decrease in the volume of a liquid drop. The difference of advancing and receding contact angles is hysteresis that shows how much the surface is rough.[7] For smoother surface, hysteresis is close to 0.

2.4 In situ Fourier transform infrared spectroscopy (In situ FT-IR)

Chemical bond change was investigated using specially designed in situ Fourier transform-Infrared spectroscopy (In situ FT-IR) in transmission mode in real-time. Figure 2.1 shows a schematic diagram of the in situ FTIR ALD/MLD reactor.[8] The IR beam from FT-IR spectrometer (Nicolet 6700, Thermo Scientific) passes through the vertically mounted specimen and the reflected beam on the a gold parabolic mirror is focused onto an external MCT-A (mercury cadmium telluride type A) IR detector. ALD system is connected to in situ FT-IR system, so that IR spectra can be collected after every half-reaction to explore a change in chemical bond that happens for each precursor or co-reactant dose by comparing differential spectra.

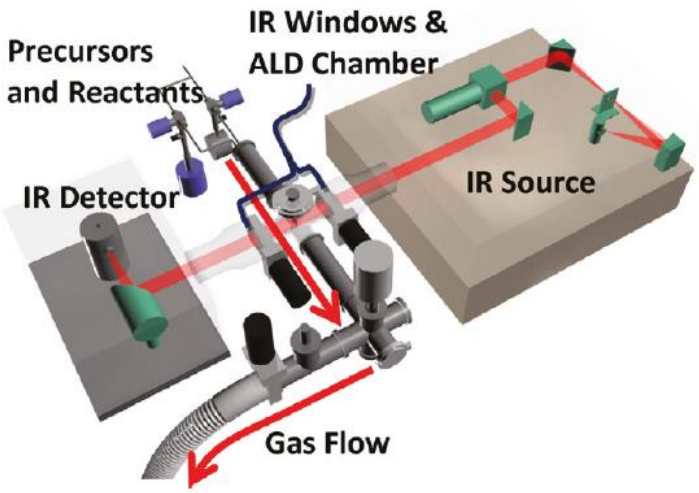

Figure 2.1 Schematic diagram of the in situ FTIR ALD/MLD reactor.[8] In the middle part of the chamber, two gate valves are installed between the IR window and reactor chamber to prevent the deposition of ALD/MLD film on the windows. The IR beam goes through the planar sample and focused into a MCT-A detector.

2.5 X-ray photoelectron spectroscopy (XPS)

Riber LAS-3000 instrument with the Al Kα line as an X-ray source was used as X-ray photoelectron spectroscopy (XPS). XPS is a technique of surface analysis that investigates chemical elements and concentration. It detects the kinetic energy of the ejected photoelectrons by irradiating the surface with soft X-ray in ultra-high vacuum state (< 10^{-9} Torr) that is needed to make the ejected electron reach at the analyzer without scattering with other gas molecules as well as to remove surface contaminations.[9] The kinetic energy of the ejected electron is determined by the equation,

$$E_k = h\nu - E_B - \phi \qquad (1)$$

where $h\nu$ is the exciting photon energy, E_B is the electron binding energy, and ϕ is the spectrometer work function. X-ray source is magnesium or aluminum and it can penetrate the surface up to ~1μm allowing the electrons emit. The depth that electrons emit depends on the energy of X-ray source. For example, if the energy of X-ray source is ~1400 eV, electrons emit in the < ~10 nm depth from the top surface.[10] The analyzer detects E_k and calculates E_B based on the eq. (a). The final spectrum is drawn intensity versus E_B where the concentration of elements can be determined by this peak intensity.

2.6 Scanning electron microscopy (SEM)

Scanning electron microscopy is image analysis tools. Accelerated electrons are generated from the electron gun by the voltage difference between cathode and anode, and then focused by condensers.[11] The detector records dissipated energy which is generated

from backscattered electrons and diffracted backscattered electrons, and photons, resulted from the interaction between electrons and the surface of specimen, and these signals form the image.

For low resolution SEM image, PHENOM™ (FEI) was used and JEOL 6400F which is field-emission scanning electron microscopy (FESEM) provides high resolution SEM image.

2.7 Transmission electron microscopy (TEM)

Transmission electron microscopy (TEM) examines a specimen with the beam of accelerated electrons.[12] The beams that pass condensers go through the specimen and are processed as an image. It is especially effective for the crystalline specimen, where the electron beams diffract resulted in contrast in the image.[13] Hitachi HF 2000 or JEOL 2000FX which is operated at 200 kV provides the ALD film images and crystalline information.

2.8 Atomic force microscopy (AFM)

DI 3000 (Digital Instruments) with tapping mode was used for atomic force microscopic (AFM) image. The laser beam detects the position of a tip in z-direction. Position of a cantilever changes by interaction between atoms on the surface and tip on the cantilever.[14] Depending on the distance between them, repulsive or attractive force is generated and this force is indirectly measured with the laser beam deflection. The

topography of the surface can be imaged by converting the force to the distance using Hook's law.

2.9 X-ray diffraction spectrometer (XRD)

XRD is a convenient tool to determine crystallinity of solid quickly and accurately. Atoms regularly arranged in a crystal of solid material diffract incoming X-ray beam resulting in constructive interference in a specific direction.[15] By measuring intensity and diffracted angle of the constructive interference, the crystalline state, magnitude of unit cell, and symmetry can be determined. In addition to peak intensity and position, the shape of the peaks is also an important factor to identify the material. To determine crystallinity of Cu_2O, Rigaku SmartLab X-ray diffractometer with Cu Ka radiation as an X-ray source (40 kV, 44 mA) was used.

2.10 UV-visible spectrophotometer

UV-Vis spectrophotometer (Evolution 300, Thermo Scientific Inc.) generates UV-visible light (wavelength of 10 – 800 nm) with xenon lamp as a source (wavelength of 190 – 1100 nm). The light passes through a cuvette containing liquid or a solid specimen attached on a holder and reaches at the detector which is silicon photodiode that measures how much light intensity is decreased compared to a reference. Absorbance, transmittance, or reflection can be measured.

2.11 UV lamp

UV-light flood system (Intelli-Ray 400, Uvitron International) provides UV irradiation for photodegradation experiment. Metal halide lamp of 400 W illuminates the curing area with UVA light (320 – 390nm). UV light intensity and irradiation time can be controlled.

References

(1) Dillon, A.; Ott, A.; Way, J.; George, S. Surface chemistry of Al_2O_3 deposition using $Al(CH_3)_3$ and H_2O in a binary reaction sequence. *Surf. Sci.* **1995,** 322, 230.

(2) Spagnola, J. C.; Gong, B.; Arvidson, S. A.; Jur, J. S.; Khan, S. A.; Parsons, G. N. Surface and sub-surface reactions during low temperature aluminium oxide atomic layer deposition on fiber-forming polymers. *J. Mater. Chem.* **2010,** 20, 4213.

(3) Fujiwara, H., *Spectroscopic ellipsometry: principles and applications.* John Wiley & Sons: 2007.

(4) Wenzel, R. N. Resistance of solid surfaces to wetting by water. *Ind. Eng. Chem.* **1936,** 28, 988.

(5) Cassie, A. B. D.; Baxter, S. Wettability of porous surfaces. *T. Faraday Soc.* **1944,** 40, 0546.

(6) Lam, C. N. C.; Wu, R.; Li, D.; Hair, M. L.; Neumann, A. W. Study of the advancing and receding contact angles: liquid sorption as a cause of contact angle hysteresis. *Adv. Colloid Interface Sci.* **2002,** 96, 169.

(7) Good, R. J. A thermodynamic derivation of Wenzel's modification of Young's equation for contact angles; Together with a theory of hysteresis1. *J. Am. Chem. Soc.* **1952,** 74, 5041.

(8) Gong, B.; Peng, Q.; Parsons, G. N. Conformal organic-inorganic hybrid network polymer thin films by molecular layer deposition using trimethylaluminum and glycidol. *J. Phys. Chem. B* **2011,** 115, 5930.

(9) Briggs, D., *Surface analysis of polymers by XPS and static SIMS.* Cambridge University Press: 1998.

(10) Brundle, C. R.; Evans Jr, C. A.; Wilson, S., *Encyclopedia of materials characterization: surfaces, interfaces, thin films.* Gulf Professional Publishing: 1992.

(11) Reimer, L. Scanning electron microscopy: physics of image formation and microanalysis. *Meas. Sci. Technol.* **2000,** 11, 1826.

(12) Williams, D. B.; Carter, C. B., *The transmission electron microscope.* Springer: 1996.

(13) Reimer, L.; Kohl, H., *Transmission electron microscopy: physics of image formation.* Springer: 2008; Vol. 36.

(14) Binnig, G.; Quate, C. F.; Gerber, C. Atomic force microscope. *Phys. Rev. Lett.* **1986,** 56, 930.

(15) Smith, F., *Industrial applications of X-ray diffraction.* CRC Press: 1999.

Chapter 3

Mechanisms for Hydrophilic/Hydrophobic Wetting Transitions on Cellulose Cotton Fibers Coated using Al_2O_3 Atomic Layer Deposition

*This chapter was published as: Lee, K,; Jur, J S,; Kim, D,; Parsons, G. *J. Vac. Sci. Technol. A* **2012,** 30, 01A163

Abstract

This report explores reactions that proceed during the first few cycles of inorganic film atomic layer deposition (ALD) on natural cellulose cotton fibers, and how surface reactions can explain the previously observed transitions in surface wetting upon ALD on cotton fibers. Atomic layer deposition of aluminum oxide and zinc oxide onto natural cotton cellulose produces a transition from hydrophilic to hydrophobic, then from hydrophobic back to hydrophilic, and we describe here the main factors that bring about. Interestingly, we show that air exposure and related adventitious carbon adsorption also affects the subsequent reactions and wetting properties obtained after subsequent ALD cycles. X-ray photoelectron microscopy and in-situ Fourier transform infrared spectroscopy data indicate Al-(O-C-)$_3$ bonding units form when trimethylaluminum interacts with surface –OH units during the first precursor doses, producing a hydrophobic finish on the cotton that remains for only a few ALD cycles. However, field-emission scanning electron microscopy (FESEM) results show that some surface roughening may occur in the first few ALD cycles, which can also contribute to the hydrophilic/hydrophobic transitions.

3.1 Introduction

Fibrous materials have recently attracted great interest for their applications in photovoltaic cells, transistors, or sensors due to their high surface area, flexibility, and low cost.[1-6] Cellulosic materials are particularly interesting because they are renewable and they degrade naturally, promoting use in sustainable design. Chemically modifying the fiber surface is important to improve appearance, chemical durability, and mechanical properties. For example, sol-gel or plasma surface treatments are known to alter surface properties of woven and nonwoven fiber mats for use in hygiene, bandages, or oil recovery functions.[7-10] Exposing fibers to reactive vapors is also known to alter the surface properties of fibers, especially their wetting characteristics.[11]

Although it is less well known than other methods in the industry, vapor phase atomic layer deposition (ALD) is known to penetrate inside complex fibrous structures such as cellulosic or wool fibers to create conformal and uniform coatings of inorganic or inorganic-organic thin films for surface modification or replicas of those structures.[12-18] As opposed to wet chemical processes, ALD leaves no liquid chemical waste and requires no expensive thermal drying steps after coating. Recently our group reported that ALD coating has a crucial effect on the wetting property of polypropylene and cotton fibers.[19,20] Hyde *et al*. showed Al_2O_3 ALD on hydrophobic polypropylene fibers significantly decreases water contact angle to 0° when deposition is performed at 60 °C, but after coating at 90 °C the surface remained hydrophobic. This was explained by formation of a uniform hydrophilic Al_2O_3 film at low temperature, whereas at higher temperature, ALD on polypropylene

produced more subsurface diffusion and growth.[21] The subsurface growth roughened the surface, promoting hydrophobicity. Moreover, Hyde *et al*. also showed that highly hydrophilic cotton fibers become hydrophobic after only a small number of Al_2O_3 ALD cycles. The fibers returned to a hydrophilic state with continued ALD coating. This wetting transition on cotton fibers was not completely understood. In this paper, we focus on the change in chemical bonding units as metal oxide ALD proceeds on the surface of cellulose cotton fibers. We demonstrate that the change in surface bonding units can explain the observed abrupt wetting transition on woven cotton fabrics. This improved insight could be important, for example, to engineer cellulose materials with controlled or variable wetting properties for advanced breathable, naturally renewable and multifunctional fibrous materials.

3.2 Experimental Procedure

Woven cotton fiber mats and cotton balls were purchased from SDL Atlas, LLC, Textile Innovators and Fisher Scientific Co., respectively, and used as received. Atomic layer deposition was performed in a custom hot wall viscous flow tube reactor where trimethylaluminum (TMA) (98%, Strem Chemicals, Inc.) and deionized (DI) water were the precursors for the Al_2O_3 film. The ZnO ALD film was deposited in the same reactor using diethylzinc (DEZ) (95%, Strem Chemicals, Inc.) and DI water. Each precursor was dosed on the substrates alternatively at an operating pressure of 2 Torr. Argon or Nitrogen was used as the carrier gas and purge gas, and they were purified before use with an inert gas filter

(Gatekeeper®, Entegris Inc.). Unless specified, ALD sequences are consisted of [TMA dose/purge/H_2O dose/purge] = [1/30/1/60 sec] and [DEZ/ purge/H_2O/purge] = [2/50/2/50 sec] for Al_2O_3 and ZnO coatings, respectively. The process temperature was fixed at 60 or 90 °C. Under these conditions, the growth rate of the Al_2O_3 and ZnO on a planar silicon wafer was measured to be ~1.2 – 1.3 and ~1.5 – 1.7 Å/cycle, respectively, consistent with well-defined atomic layer deposition.[22,23]

Some ALD coating experiments were performed a specially designed reactor equipped with in-situ Fourier transmission infrared spectroscopy. This reactor, described in detail elsewhere,[22,24] permits analysis of each ALD half cycle on porous fiber substrates, such as the woven cotton studied here.

Static water contact angle was measured at room temperature using a goniometer (Rame-Hart, Inc., model 200-F1) with DI water. For each sample, data was collected from several different positions on each substrate, and the average value was recorded. X-ray photoelectron spectroscopy (XPS) was performed with a Riber LAS-3000 instrument with the Mg Kα line as an X-ray source with energy resolution of about 0.1 eV. Fourier transform infrared (FTIR) spectra were collected by FTIR spectrometer (Thermo Scientific Nicolet 670) equipped with MCT-A detector cooled by liquid nitrogen. Each spectrum was acquired from a total of 2050 scans with a resolution of 4 cm^{-1}. Scanning electron microscopic images were taken with field-emission scanning electron microscopy (FESEM, JEOL 6400F) operating at 5 kV to examine the surface roughness.

3.3 Results and Discussion

The water contact angle on cotton fiber mats was measured after Al_2O_3 and ZnO ALD at the process temperatures of 60 and 90 °C. Bare cotton fiber mats were highly water absorbent with a contact angle of 0° before ALD. However, as shown in Figure 3.1, they abruptly changed to a hydrophobic state with a contact angle exceeding 100° after only 2 cycles of Al_2O_3 and 5 cycles of ZnO ALD. As shown in the figure, coating with more cycles also produced a hydrophobic surface, but with continued coating, contact angles decreased as the number of ALD cycles increased with large error bar from the contact angles of 0° as well as over 60° even on the same substrate. It indicates that this is a transition region passing from hydrophobic state into the next stage. Further coating produced a fully hydrophilic state. The ALD cycles at which the surface transitioned back to fully wetting (contact angle = 0°) depended on the process temperature and composition of the oxide film. Generally, though, the transitions were very similar for Al_2O_3 and ZnO coatings deposited between 60 and 90 °C. The main chemical units on the surface of the starting cellulose are C-OH groups, and the surface transitions to Al-OH upon coating with Al_2O_3 layers. Both of these surface groups are expected to produce a hydrophilic finish. To demonstrate that the cotton wetting was not affected by physical processes such as sample heating, inert gas exposure and water vapor desorption that occur during the ALD process sequence, we placed cotton fiber samples into the ALD reactor and heated under dry inert gas flow for ~40 min (i.e. typical ALD process time), without any TMA or water vapor exposure. After this treatment, the samples were highly hydrophilic as they were before heating. The surface

wetting transitions in Figure 3.1 therefore result uniquely from the chemical reactions during the TMA/water ALD treatment.

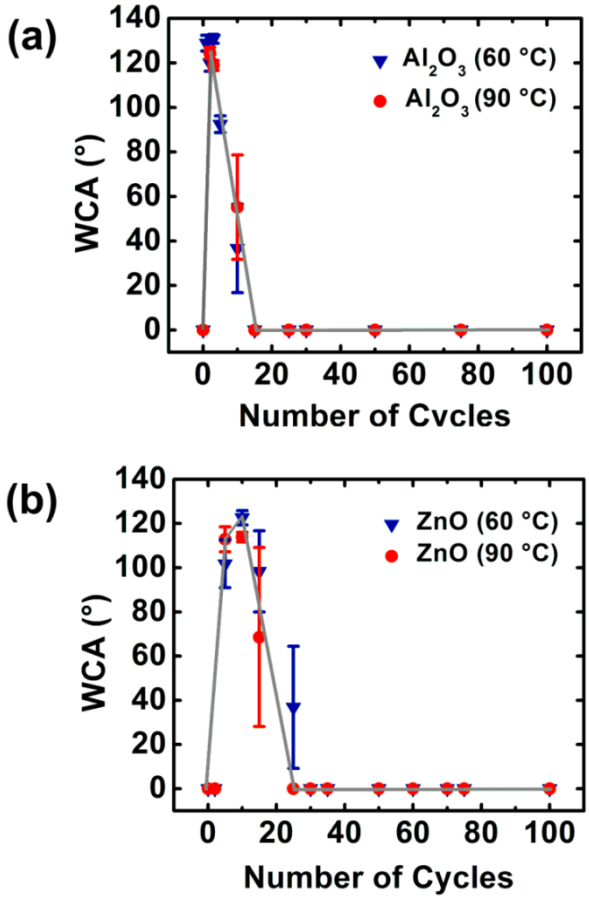

Figure 3.1 Water contact angle on cotton fiber mats after (a) Al_2O_3 ALD and (b) ZnO ALD at 60 and 90 °C. In both cases, hydrophilic cotton fibers change to hydrophobic after a few number of ALD cycles, and come back to hydrophilic again after a certain number of ALD cycles with no significant dependence on the deposition temperature and different kinds of metal oxide film.

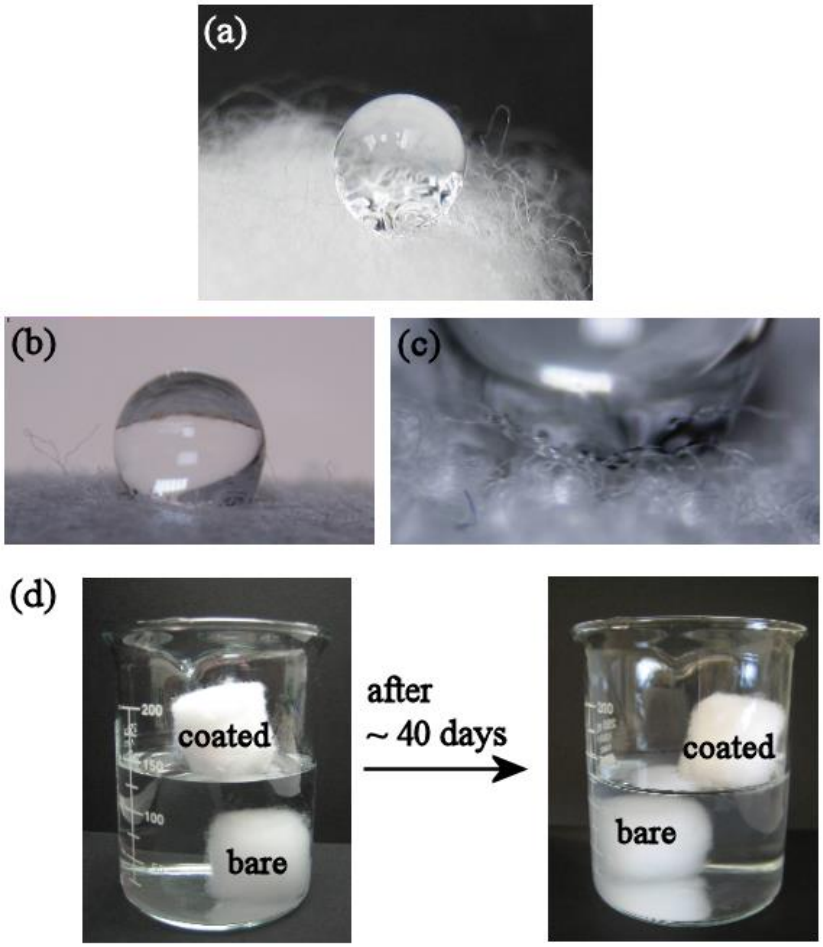

Figure 3.2 Pictures of a water drop on (a) cotton ball and (b) cotton fiber mat after changed to hydrophobic with 3 cycles of Al_2O_3 ALD at 60 ºC. (c) The magnified image that shows the interface between cotton fiber mat and water drop. (d) To test stability of hydrophobic cotton, cotton ball with 3 cycles of Al_2O_3 ALD was placed in water with bare cotton ball and it has been floated on water surface more than a month, which shows that hydrophobicity induced by ALD is a stable property.

Figures 3.2(a) and (b) show water drops on a hydrophobic cotton ball and cotton fiber mat, respectively, after coating the cotton with 3 cycles of Al_2O_3 ALD at 60 °C. A more magnified optical image of the interface between the woven cotton fiber mat and water drop,

displayed in Figure 3.2(c), shows individual fibrils from the cotton mat act to hold up the water drop. To test the long-term stability of the hydrophobicity, a cotton ball coated with 3 cycles of Al_2O_3 ALD was placed in a vessel of water alongside an uncoated cotton ball (shown in Fig. 3.2d). Upon placing the balls in the water, the bare cotton ball immediately sank down to the bottom of the vessel, but the coated cotton ball readily floated. After several weeks in this condition, the coated cotton ball remained stable on the water surface, indicating that the hydrophobicity induced by ALD is a stable property with possibility for practical applications.

In the next experiment, the water contact angle on cotton fiber mats was measured after a sequence of 3 metal oxide ALD cycles. Once the wetting was quantified in air, the substrate was returned to the reactor for another 3 ALD cycle sequence, after which the wetting was measured again. Each time the sample was removed from the reactor, it was measured quickly and returned to the reactor. The total air exposure time was ~10 minutes between each ALD coating. This procedure was repeated several times for coating samples with alumina or zinc oxide, and the results are presented in Figure 3.3. The labels "A" and "Z" in Figure 3.3 correspond to one sequence of 3 ALD cycles of Al_2O_3 (for "A") or ZnO (for "Z") at 60 °C followed by air exposure and water contact angle measurement. Each "A" sequence is 3 Al_2O_3 ALD cycles + 10 min in air, and each "Z" sequence is 3 ZnO ALD cycles + 10 min in air. After the first "A" sequence, cotton fiber mats became hydrophobic consistent with results in Figure 1. We therefore expected that repeating the coating/measurement sequence would produce a transition to fully wetting. However, as displayed in Figure 3.3(a), after 10 "A" coating/measurement steps (i.e. a total of 30 Al_2O_3

ALD cycles) the cotton fiber mats still showed a high contact angle of more than 100°. Similarly, when the cotton fiber mats were exposed to alternating "A" and "Z" cycles, the substrate remained hydrophobic even after the 10^{th} "A" + "Z" sequence, as shown in Figure 3.3(b). These results suggest that adventitious carbon adsorbed during air exposure affects surface reactions during the first few ALD cycles and therefore influences the detailed chemical structure that determines the observed water contact angle. As a control, we performed experiments that mimicked the "A" sequence, but did not produce adventitious carbon. Specifically, after each set of 3 ALD Al_2O_3 cycles, the cotton fiber mats were left in the reactor where they were exposed to a flow of N_2 at 760 Torr for 10 minutes. This is the same as "A", except the air exposure was replaced with N_2. After 10 of these "modified A" sequences, the contact angle was 0°. In other words, the cotton fiber mats turned back to being hydrophilic after the total 30 cycles of Al_2O_3 without air exposure, but they remained hydrophobic with the same number of ALD cycles if exposed to air between each sequence. Therefore, as suggested by Hyde *et al*.,[20] we conclude that adventitious carbon adsorbed on the cotton fiber surface during air exposure influences the reactions during the first few ALD cycles.

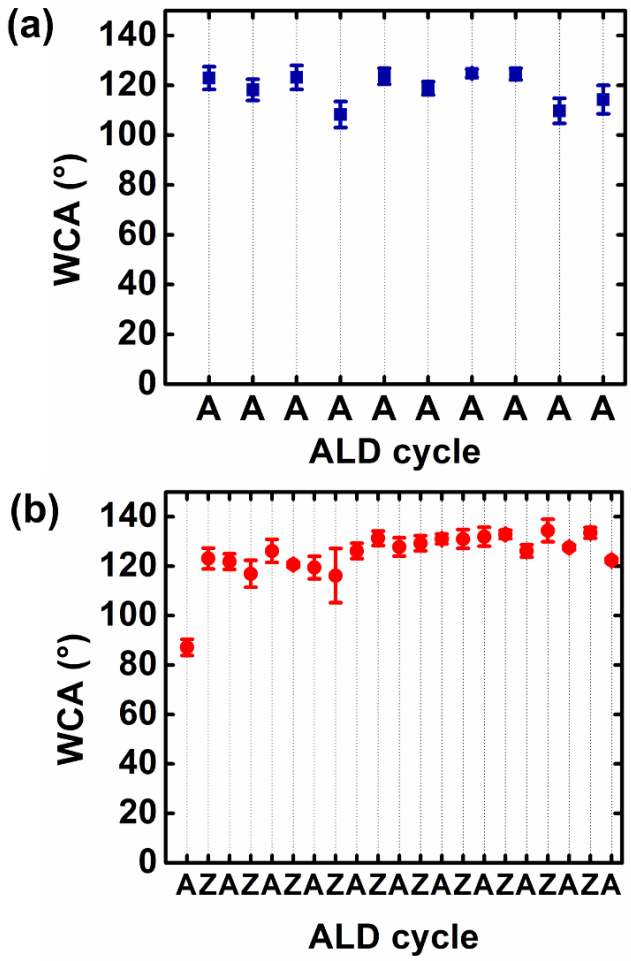

Figure 3.3 Water contact angle (WCA) on cotton fiber mats after (a) a repeated sequence of 3 Al_2O_3 ALD cycles 60 ºC followed by air exposure and contact angle measurement (sequence labeled "A"); and (b) after a different procedure involving sequence "A" and sequence "Z", where "Z" corresponds to 3 ZnO ALD cycles followed by contact angle measurement in air. In both cases, the surface remains hydrophobic even after more than 10 repetitions (i.e. after more than 30 ALD cycles). Samples prepared using 30 cycles of ALD coating without breaks for air exposure produced a hydrophilic finish.

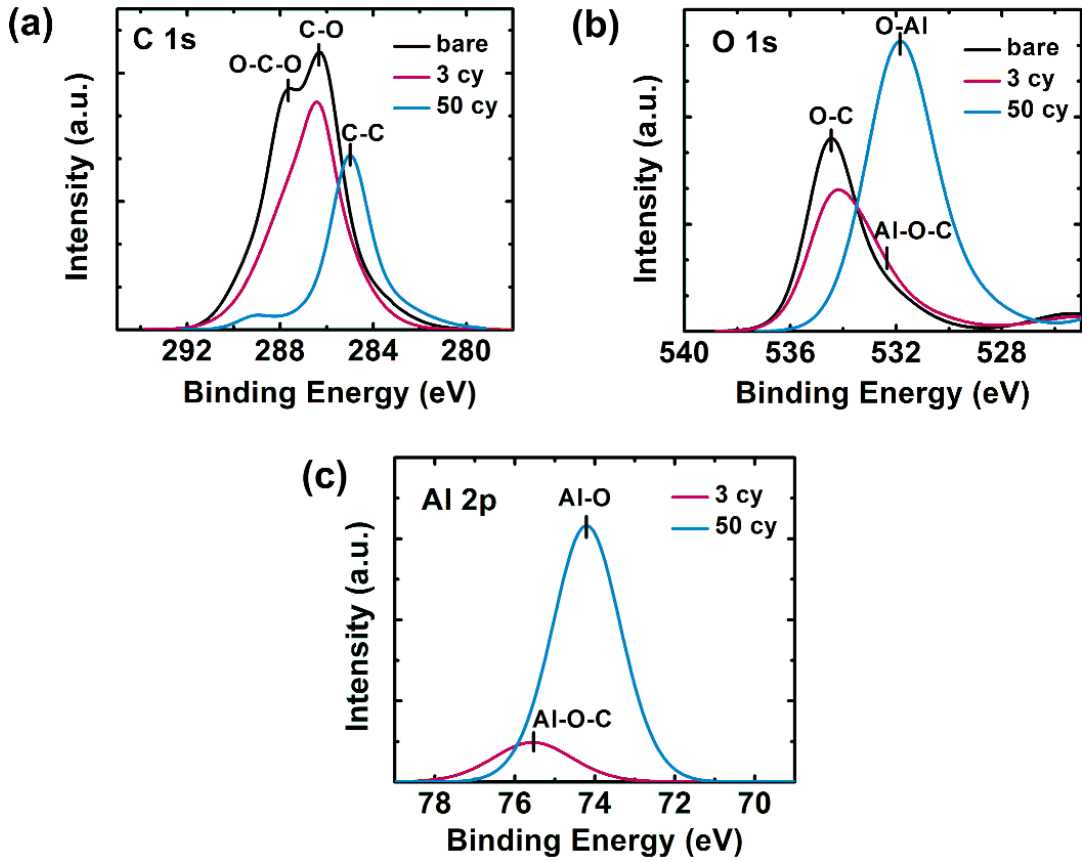

Figure 3.4 XPS spectra of bare cotton fiber mat (black line), cotton fiber mats after 3 cycles (red line), and 50 cycles (blue line) of Al_2O_3 ALD at 60 ºC. (a) The predominant peaks at 286.2 and 287.8 eV from bare cotton fiber mat correspond to O-C-O and C-O bonds, respectively, but the intensity of those peaks is decreased with increasing ALD cycles. (b) Al-O-C peak is shown on the cotton fiber mat after 3 cycles of ALD, whereas Al-O peak becomes dominant with 50 cycles of ALD. (c) Al-O-C peak on cotton fiber mat after 3 cycles and Al-O peak after 50 cycles of Al_2O_3 ALD are consistent with the peaks shown in (b).

To identify the elements and chemical bonds on the surface of hydrophobic cotton, uncoated cotton fiber mats and cotton fiber mats coated with 3 and 50 cycles of Al_2O_3 ALD at 60 °C were analyzed with XPS. The resulting C 1s, O 1s, and Al 2p spectra are shown in

Figure 3.4, which were calibrated to C-C/C-H bonding with 285 eV. In the C 1s spectra of uncoated cotton mats in Figure 3.4(a), major peaks at 286.2 and 287.8 eV indicate O-C-O and C-O bonds consistent with the cellulose molecules.[25] The intensity of the peaks decreases after 3 cycles of Al_2O_3 ALD, and the peaks decrease further after 50 ALD cycles. Also, the O 1s spectra in Figure 3.4(b) show a peak at 534.5 eV for the uncoated cotton fiber mats, confirming C-O bonds. The intensity of the C-O peak decreased after 3 cycles of Al_2O_3 ALD while a shoulder at 532.4 eV corresponding to Al-O-C bonds becomes visible. After 50 cycles, the O 1s shows a large peak at 531.9 indicating Al_2O_3 coating. This transition is consistent with the Al 2p spectra in Figure 3.4(c) that shows no peak for the starting sample, a Al-O-C peak at 75.5 eV after 3 ALD cycles, and a predominant Al-O peak at 531.9 eV after 50 ALD cycles. Therefore, XPS results show us that Al-O-C bonds were formed on hydrophobic cotton after 3 cycles of Al_2O_3 ALD and that the Al-O bonds became dominant on the cotton surface as the number of ALD cycles increased.[26,27]

The chemical bond changes on cotton fiber mats after each precursor dose was studied in more detail using in-situ FTIR spectroscopy during Al_2O_3 ALD.[22,24] For this experiment, the TMA or H_2O, was dosed for 3 sec on the cotton fiber mats and then, the chamber was isolated from the pump for 1 min to soak the fiber substrate followed by 2 min purge with Ar gas to remove extra precursors and byproducts at 60 °C. After each precursor dose/soak cycle, the FTIR spectrum was collected and the previous spectrum was subtracted from the spectrum, so that only differential peaks induced by that cycle are shown. Figure 3.5 presents the absorption spectrum of the uncoated cotton fiber mats, as well as differential spectra collected after the first and tenth ALD cycles. Considering the Al_2O_3 ALD

mechanism, TMA reacts with –OH groups on the surface leaving Al-CH_3 groups which can be confirmed by CH_3 deformation peaks in in-situ FTIR spectroscopy.[22,23] However, there is no visible peak corresponding to CH_3 deformation in the spectrum after the first TMA dose/soak on cotton fiber mats. However, the first TMA exposure produces a decrease in a broad peak between 3080 and 3650 cm^{-1} due to OH reacting with the TMA.[28] Moreover, the peak changes assigned to CH_3 symmetric and asymmetric deformation[29,30] at 1210 and 1446 cm^{-1}, are observed after the 10th TMA cycle, where they increase after the 10th TMA dose and decrease in the next H_2O exposure.

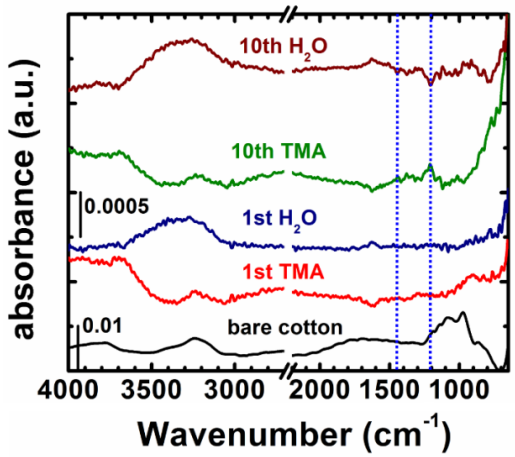

Figure 3.5 In-situ FTIR spectra collected after 1st and 10th TMA and H_2O dose at 60 ºC on cotton fiber mat with the absorption spectrum of the untreated cotton (bottom) and differential spectra after TMA and water exposure cycles. Peak changes at 1210 and 1460 cm^{-1} indicated by dot lines correspond to symmetric and asymmetric CH_3 deformations. These deformation modes are not visible during the first TMA exposures, but are visible after the 10th TMA dose. Furthermore, the broad peak change between 3080 and 3650 cm^{-1} shows a sequential decrease and increase in the bonded OH corresponding to TMA and H_2O doses, respectively.

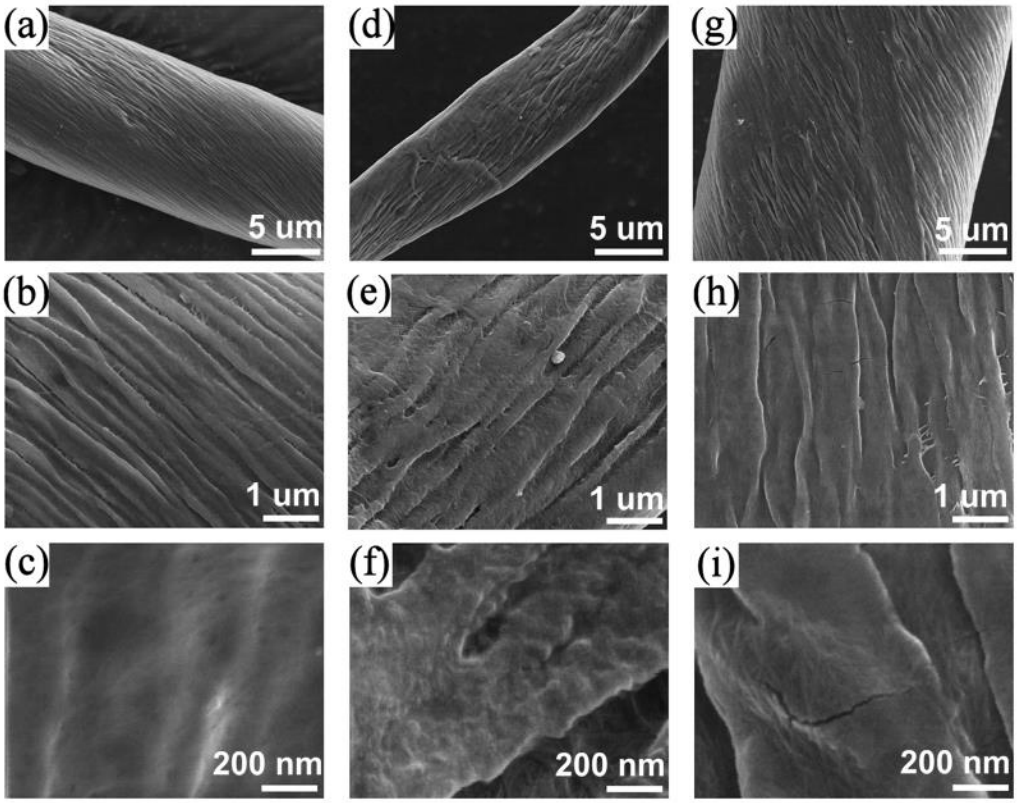

Figure 3.6 FESEM images of bare cotton ball (a – c), cotton ball after 3 cycles of Al_2O_3 ALD (d – f), and 50 cycles of Al_2O_3 ALD at 60 ºC (g – i). (a, d, g) Each cotton fiber consists of a lot of fibrils. (b, e, h) The surfaces of cotton fibers look covered by Al_2O_3 film when ALD cycles increases. Some cracks on the surface of cotton fiber ball after 50 cycle of ALD are induced by the stiffness of Al_2O_3 film. (c, f, i) Higher resolution images show rougher surface after 3 cycles of Al_2O_3 ALD compared with other cotton balls.

The XPS and FTIR results on the cellulose fibers show different reaction products after the first few TMA doses compared to after several ALD cycles. The experiments with air exposure show that adventitious carbon also affects the surface products. A previous report by Akhter *et al.*[31] shows chemical changes on heavily hydroxylated polyvinyl alcohol when the surface is exposed to TMA in ultrahigh vacuum. They showed that the TMA reacts

readily and completely with the abundant surface -OH groups, producing stable Al-(O-C-)$_3$ surface complexes. Our XPS and FTIR results are consistent with a similar reaction proceeding on the cellulose cotton, where all three methyl groups on the TMA react with available surface hydroxyl groups during the first TMA exposure steps to form Al-(O-C-)$_3$ surface units. It is reasonable to expect that a TMA molecule impinging on cellulose could react with three -OH groups because the polymer provides a nanostructured, non-planar surface with a high OH density. Steric effects on a solid planar surface impede reaction with three OH units. The Al-(O-C-)$_3$ groups on the cellulose can also explain the hydrophilic/hydrophobic transition, where the Al-(O-C-)$_3$ termination presents a more hydrophobic structure, with minimal Al-OH groups present on the surface after the first TMA cycles. Continued ALD allows aluminum oxide to nucleate and grow on the defective surface. After several cycles, the TMA/water ALD sequence becomes established and the surface transitions to predominantly hydroxylated alumina, which explains the subsequent observed hydrophobic/hydrophilic transition. The results from the air-exposure experiments show further that the adventitious carbon added onto the surface will affect the first few ALD cycles. In this case, the adventitious carbon also impedes formation of hydrophilic Al-OH, either by blocking any -OH sites available to react with TMA, or by fully reacting with TMA to form Al-O-C units, allowing the hydrophobic surface structure to be maintained for a few ALD cycles.

In addition to the chemical bonding change on cotton fiber surface, we also used FESEM to examine the effect of ALD cycles on surface nanoroughness. Figure 3.6 shows a set of FESEM images of fibers extracted from an uncoated cotton ball and from cotton balls

coated with 3 and 50 cycles of Al_2O_3 ALD at 60 °C. Each fiber is shown at three magnification scales. As seen on the uncoated fiber image in Figures 3.6(b) and (c) a cotton fiber consists of a group of fibrils that induce roughness on the fiber surface with a characteristic scale that is less than the fiber diameter. Even so, at the highest magnification, the uncoated cotton appears relatively smooth. After 3 ALD cycles, the fibril-scale roughness is still visible in panel 3.6(e), but the image in 3.6(f) suggests that the surface at the ~ 200 nm scale has become more rough after 3 ALD cycles. The image in Figures 3.6(i) collected after 50 ALD cycles shows decreased roughness in comparison to that after 3 ALD cycles, as well as small cracks within the conformal oxide coating. It is well known that an increase in micro- and nano-scale roughness on a hydrophobic or heterogeneous surface can promote the hydrophobicity.[32,33] Therefore, the surface roughness evolution displayed in Figure 3.6 contributes the hydrophobicity of cotton surface induced by chemical bonding change.

3.4. Summary

The results presented here provide new insight into the mechanisms associated with the observed hydrophilic/hydrophobic/hydrophilic transitions on cotton fibers after coating with a few ALD cycles of TMA/water and/or DEZ/water. Infrared transmission and XPS results show that during the first TMA doses on the cotton cellulose surface, TMA reacts with available –OH groups to form stable Al-(O-C-)$_3$ units that are not active during the subsequent H_2O dose. These units are proposed to help produce the visible hydrophilic/hydrophobic transition. Continued ALD cycles allow deposition of hydroxylated

aluminum oxide, resulting in the subsequent hydrophobic/hydrophilic change. The IR data shows that the first TMA dose produces a large decrease in OH groups, consistent with consumption by the TMA, but the Al-CH_3 groups that are typically observed[22] during the TMA/water ALD are not seen. After several TMA/water cycles, the Al-CH_3 deformation modes are visible showing good TMA/water ALD. In addition to the evolution in the surface chemical composition, an increase in surface nano-roughness may occur during the first few ALD cycles, which will also help support the hydrophobic surface structure on the cotton fibers. These results allow us to better understand the initial cycles of inorganic ALD films on organic surfaces. They also help to explain wetting properties of cotton and other related materials during ALD coating, and could help enable researchers to make use of these phenomena for practical applications.

References

(1) O'Connor, B.; Pipe, K. P.; Shtein, M. Fiber based organic photovoltaic devices. *Appl. Phys. Lett.* **2008,** 92, 193306.

(2) Hart, S. D.; Maskaly, G. R.; Temelkuran, B.; Prideaux, P. H.; Joannopoulos, J. D.; Fink, Y. External reflection from omnidirectional dielectric mirror fibers. *Science* **2002,** 296, 510.

(3) Hamedi, M.; Forchheimer, R.; Inganas, O. Towards woven logic from organic electronic fibres. *Nat. Mater.* **2007,** 6, 357.

(4) Lee, J. B.; Subramanian, V. Weave patterned organic transistors on fiber for e-textiles. *IEEE Trans. Electron Devices* **2005,** 52, 269.

(5) Wang, X. Y.; Drew, C.; Lee, S. H.; Senecal, K. J.; Kumar, J.; Sarnuelson, L. A. Electrospun nanofibrous membranes for highly sensitive optical sensors. *Nano Lett.* **2002,** 2, 1273.

(6) Jur, J. S.; Sweet, W. J.; Oldham, C. J.; Parsons, G. N. Atomic layer deposition of conductive coatings on cotton, paper, and synthetic fibers: conductivity analysis and functional chemical sensing using “all-fiber” capacitors. *Adv. Funct. Mater.* **2011,** 21, 1993.

(7) Zhang, J.; France, P.; Radomyselskiy, A.; Datta, S.; Zhao, J. A.; van Ooij, W. Hydrophobic cotton fabric coated by a thin nanoparticulate plasma film. *J. Appl. Polym. Sci.* **2003,** 88, 1473.

(8) Deschamps, G.; Caruel, H.; Borredon, M.-E.; Bonnin, C.; Vignoles, C. Oil Removal from water by selective sorption on hydrophobic cotton fibers. 1. Study of sorption properties and comparison with other cotton fiber-based sorbents. *Environ. Sci. Technol.* **2003,** 37, 1013.

(9) Vilcnik, A.; Jerman, I.; Vuk, A. S.; Kozelj, M.; Orel, B.; Tomsic, B.; Simonic, B.; Kovac, J. Structural properties and antibacterial effects of hydrophobic and oleophobic sol-gel coatings for cotton fabrics. *Langmuir* **2009,** 25, 5869.

(10) Meilert, K. T.; Laub, D.; Kiwi, J. Photocatalytic self-cleaning of modified cotton textiles by TiO_2 clusters attached by chemical spacers. *J. Mol. Catal. A: Chem.* **2005,** 237, 101.

(11) Cunha, A. G.; Freire, C.; Silvestre, A.; Neto, C. P.; Gandini, A.; Belgacem, M. N.; Chaussy, D.; Beneventi, D. Preparation of highly hydrophobic and lipophobic cellulose fibers by a straightforward gas-solid reaction. *J. Colloid Interface Sci.* **2010,** 344, 588.

(12) Niskanen, A.; Arstila, K.; Ritala, M.; Leskela, M. Low-temperature deposition of aluminum oxide by radical enhanced atomic layer deposition. *J. Electrochem. Soc.* **2005,** 152, F90.

(13) Niskanen, A.; Arstila, K.; Leskela, M.; Ritala, M. Radical enhanced atomic layer deposition of titanium dioxide. *Chem. Vap. Deposition* **2007,** 13, 152.

(14) Kemell, M.; Pore, V.; Ritala, M.; Leskela, M.; Linden, M. Atomic layer deposition in nanometer-level replication of cellulosic substances and preparation of photocatalytic TiO_2/cellulose composites. *J. Am. Chem. Soc.* **2005,** 127, 14178.

(15) Kemell, M.; Pore, V.; Ritala, M.; Leskela, M. Ir/oxide/cellulose composites for catalytic purposes prepared by atomic layer deposition. *Chem. Vap. Deposition* **2006,** 12, 419.

(16) Knez, M.; Niesch, K.; Niinisto, L. Synthesis and surface engineering of complex nanostructures by atomic layer deposition. *Adv. Mater.* **2007,** 19, 3425.

(17) Peng, Q.; Sun, X. Y.; Spagnola, J. C.; Hyde, G. K.; Spontak, R. J.; Parsons, G. N. Atomic layer deposition on electrospun polymer fibers as a direct route to Al_2O_3 microtubes with precise wall thickness control. *Nano Lett.* **2007,** 7, 719.

(18) King, J. S.; Heineman, D.; Graugnard, E.; Summers, C. J. Atomic layer deposition in porous structures: 3D photonic crystals. *Appl. Surf. Sci.* **2005,** 244, 511.

(19) Parsons, G. N.; Hyde, G. K.; Park, K. J.; Stewart, S. M.; Hinestroza, J. P. Atomic layer deposition of conformal inorganic nanoscale coatings on three-dimensional natural fiber systems: Effect of surface topology on film growth characteristics. *Langmuir* **2007,** 23, 9844.

(20) Hyde, G. K.; Scarel, G.; Spagnola, J. C.; Peng, Q.; Lee, K.; Gong, B.; Roberts, K. G.; Roth, K. M.; Hanson, C. A.; Devine, C. K.; Stewart, S. M.; Hojo, D.; Na, J. S.; Jur, J. S.; Parsons, G. N. Atomic layer deposition and abrupt wetting transitions on nonwoven polypropylene and woven cotton fabrics. *Langmuir* **2010,** 26, 2550.

(21) Jur, J. S.; Spagnola, J. C.; Lee, K.; Gong, B.; Peng, Q.; Parsons, G. N. Temperature-dependent subsurface growth during atomic layer deposition on polypropylene and cellulose fibers. *Langmuir* **2010,** 26, 8239.

(22) Spagnola, J. C.; Gong, B.; Arvidson, S. A.; Jur, J. S.; Khan, S. A.; Parsons, G. N. Surface and sub-surface reactions during low temperature aluminium oxide atomic layer deposition on fiber-forming polymers. *J. Mater. Chem.* **2010,** 20, 4213.

(23) Dillon, A. C.; Ott, A. W.; Way, J. D.; George, S. M. Surface chemistry of Al_2O_3 deposition using $Al(CH_3)_3$ and H_2O in a binary reaction sequence. *Surf. Sci.* **1995,** 322, 230.

(24) Gong, B.; Peng, Q.; Parsons, G. N. Conformal organic-inorganic hybrid network polymer thin films by molecular layer deposition using trimethylaluminum and glycidol. *J. Phys. Chem. B* **2011**.

(25) Cueff, R.; Baud, G.; Benmalek, M.; Besse, J. P.; Butruille, J. R.; Jacquet, M. Alumina coatings on polyethylene terephthalate: Characterisation and X-ray photoelectron spectroscopy study. *Surf. Coat. Technol.* **1996,** 80, 96.

(26) Lee, P. F.; Dai, J. Y.; Wong, K. H.; Chan, H. L. W.; Choy, C. L. Growth and characterization of Hf-aluminate high-k gate dielectric ultrathin films with equivalent oxide thickness less than 10 angstrom. *J. Appl. Phys.* **2003,** 93, 3665.

(27) Yu, H. Y.; Li, M. F.; Cho, B. J.; Yeo, C. C.; Joo, M. S.; Kwong, D. L.; Pan, J. S.; Ang, C. H.; Zheng, J. Z.; Ramanathan, S. Energy gap and band alignment for $(HfO_2)_{(x)}(Al_2O_3)_{(1-x)}$ on (100) Si. *Appl. Phys. Lett.* **2002,** 81, 376.

(28) Li, Q.; Renneckar, S. Supramolecular structure characterization of molecularly thin cellulose I nanoparticles. *Biomacromolecules* **2011,** 12, 650.

(29) Gow, T. R.; Lin, R.; Cadwell, L. A.; Lee, F.; Backman, A. L.; Masel, R. I. Decomposition of trimethylaluminum on silicon(100). *Chem. Mater.* **1989,** 1, 406.

(30) Varma, V.; Bhattacharjee, R.; Vasan, H. N.; Rao, C. N. R. Infrared and Raman spectroscopic investigations of methylammonium haloantimonates(III), $[N(CH_3)_4\text{-}nHn]_3$

Sb_2X_9 (n = 0-3, X = Cl or Br), through their phase transitions. *Spectrochim. Acta, Part A* **1992,** 48, 1631.

(31) Akhter, S.; Zhou, X. L.; White, J. M. XPS study of polymer organometallic interaction - trimethyl aluminum on polyvinyl-alcohol polymer. *Appl. Surf. Sci.* **1989,** 37, 201.

(32) Wenzel, R. N. Resistance of solid surfaces to wetting by water. *Ind. Eng. Chem.* **1936,** 28, 988.

(33) Cassie, A. B. D.; Baxter, S. Wettability of porous surfaces. *Trans. Faraday Soc.* **1944,** 40, 546.

Chapter 4

High Performance Photocatalytic Metal Oxide Synthetic Nanosheets Formed by Atomic Layer Deposition

This chapter is submitted for publication as: K. Lee; Losego, M. D.; Kim, D.; Parsons, G.

ACS Nano

Abstract

Two-dimensional nanosheet materials, including graphene, MoS_2, perovskites and others derived from naturally occurring bulk layered compounds show unique electrical and mechanical functionality. Because nanosheets are typically exfoliated from bulk materials, structures are generally limited to single-compound systems with limited control over layer dimension. Here we present a new strategy for synthesizing 2D nanosheets, including single and multi-compound structures, using atomic layer deposition (ALD) on dissolvable substrates. The synthetic nanosheets formed by ALD are distinct from exfoliated natural nanosheets in that they are ultrathin variants of common 3D materials. We have used this ALD method to synthesize TiO_2, ZnO, Al_2O_3 and TiO_2/ZnO bi-layered nanosheets that function as dispersible photocatalysts in aqueous media. We find a 5× synergistic rate enhancement in our bilayer nanosheets which is unprecedented when compared to other bi-component photocatalysts. Most importantly, we believe that this synthetic approach can be universally applied to a wide range of materials systems, revolutionizing nanosheet applicability in nanoelectronics, nano-optics, nano-catalysis, and nano-composites.

4.1 Introduction

Nanosheets are typically formed by mechanical or chemical exfoliation from a solid,[1-7] or via vapor-phase or hydrothermal growth in morphologically constrained systems[8,9] showing unique electrical and mechanical properties.[10-14] Atomic layer deposition uses a binary self-limiting reaction sequence to precisely control thin film nucleation and growth at the monolayer level[15,16] and enable formation of gradual or abrupt material junctions by adjusting the precursor exposure sequence in successive ALD cycles. While ALD thin film materials and coatings are well-known in electronic device manufacturing, we hypothesize that controlled ALD on solution-soluble substrates could expand the known benefits of ALD to create free-floating 2D materials without the constraint of a substrate, capable of functional performance analogous to natural nanosheets. Readily controlled thickness and composition in these synthetic ALD nanosheets would provide key advantages including multi-component layering, controlled electronic structuring, and modified optical response.

4.2. Experimental process

Sacrificial Polymer layer: Polyacrylic acid (PAA, M_w = 1,800 g/mol) and polyvinyl alcohol (PVA, M_w = 16,000 g/mol) were purchased from Sigma-Aldrich and Acros Organics, respectively and used without further purification. They were dissolved in deionized (DI) water with a concentration of 2 wt% followed by spin-coating onto a Si/SiO_2 substrate for 30 s at 3000 rpm. For the results shown in this manuscript, nanosheets were prepared with a PVA sacrificial layer.

Atomic Layer Deposition (ALD): The precursors for ZnO and Al_2O_3 films are diethylzinc (DEZ, 95%) and trimethylaluminum (TMA, 98%), respectively. For TiO_2 films, titanium tetrachloride ($TiCl_4$, 99%) was used as a precursor. All precursors were purchased from Strem Chemicals, Inc. ALD was performed in a custom hot wall viscous flow tube reactor where each precursor was dosed sequentially with DI water as the oxidant. The partial pressures for DEZ, TMA, and DI water was 0.1 – 0.2 Torr at the deposition temperature of 90 °C while TiO_2 ALD was performed with partial pressure 0.03 Torr of $TiCl_4$ at deposition temperature of 100 ºC. The operating pressure was 2 Torr for all ALD processes. Growth per cycles (GPC) were 1.3, 1.7, and 0.4 Å/cycle for Al_2O_3, ZnO, and TiO_2, respectively.

Film Separation: After coating the PVA sacrificial layer with ALD, the films were cut with a razor blade while still on the silicon substrate to facilitate dissolution of the sacrificial layer. Next, the wafers were immersed in DI water heated to 60 °C. After several minutes, metal oxide nanosheets were separated from the substrate and became dispersed in aqueous solution.

For AFM, SEM, or TEM investigations, the nanosheets were collected on a substrate dipped in solution. To collect nanosheets more effectively, carbon tetrachloride was added to the nanosheet dispersion followed by shaking. When a substrate such as oxidized silicon was introduced vertically in the solution, nanosheets were collected on the substrate densely to minimize total interface energy of the system.[17] For AFM, samples collected on flat SiO_2 were annealed in air at 300 ºC for 1 h to remove any residual polymer. For TEM, annealing was also performed at 300 °C to 450 ºC for 1 h to crystallize the material.

Characterization: ALD film thickness was measured with ellipsometry (Alpha-SE Ellipsometer, JA Woollam Co., Inc.) using a reference Si/SiO_2 substrate. Atomic force microscopy (AFM, DI 3000) and scanning electron microscopy (SEM, JEOL 6400) with energy dispersive X-ray analysis (EDX) was used to image nanosheets, measure thickness and analyze composition. Transmission electron microscopy (TEM, Hitachi HF 2000) operated at 200 kV was used to characterize crystallinity.

Photocatalysis Measurement: Methyl orange was purchased from Sigma-Aldrich. Nanosheets were prepared on Si/SiO_2 substrates (2×2 cm^2/ea) using a PVA sacrificial layer. A fixed volume of 10 ml DI water was used to dissolve the sacrificial layers and disperse the nanosheets. Following dispersion, 10 ppm of methyl orange was added to the volume. The concentration of TiO_2 nanosheets was controlled by changing the number of substrates dissolved in the DI water. For comparison, 10 ppm aqueous solution of methyl orange without nanosheets was also tested. UV-light irradiation was achieved using a shuttered UV-light flood system (Intelli-Ray 400, Uvitron International). The Pyrex vial was placed under the UV-lamp with constant stirring. UV-intensity was varied from 122.5 $\mu W/cm^2$ to 245 $\mu W/cm^2$. After irradiation, absorbance of the solution was measured by sampling every 30 min with UV-Vis spectrophotometer (Evolution 300, Thermo Scientific Inc.) at 466 nm, which is the major absorbance peak of methyl orange. After sampling, the solution was returned to the vial and irradiation was continued. This procedure was repeated for 3 h for each sample. Care is taken to maintain uniform and reproducible UV flux conditions during all irradiation measurements, to achieve consistent conditions for each sample analyzed.

4.3. Results and discussion

The overall procedure for ALD synthetic nanosheet production is presented in Figure 4.1. Sacrificial layers of water soluble polymers were spun-cast onto Si substrates with native SiO_2 (Figure 4.1a). We choose polyvinyl alcohol (PVA) and polyacrylic acid (PAA) for sacrificial layers because of their ability to promote ALD metal oxide nucleation[18] and their high water solubility.[19] Films of controlled thickness and composition were then deposited by ALD onto the sacrificial polymer layer (Figure 4.1b). To facilitate dissolution of the sacrificial layer, surfaces were pre-cut by hand with a razor (Figure 4.1c). Sacrificial layers were dissolved in deionized (DI) water heated to ~60 °C. After several minutes (1 – 5 min), nanosheets with lateral sizes up to ~3 mm were released into solution (Figure 4.1d). For structural analysis, nanosheets were collected on clean silicon wafers for atomic force microscopy (AFM) analysis or on molybdenum grids for transmission electron microscopy (TEM) imaging.

Figure 4.2 summarizes how the ALD process provides high fidelity control over nanosheet thickness and morphology. Figure 4.2(a) illustrates that TiO_2 nanosheet thickness, measured by ellipsometry and AFM, varies linearly with the number of ALD growth cycles. AFM profiles of released nanosheet thickness precisely match ellipsometry measurements collected from control films grown directly on silicon wafers. Figures 4.2(b) – (d) show AFM images collected from TiO_2, Al_2O_3, and ZnO nanosheets respectively. These AFM scans are collected at the minimum thickness for each composition formed under the conditions used. Below this thickness, the ALD layers tend to break apart into nanosheets with smaller lateral

dimension. For this series of ALD precursor chemistries on PAA or PVA sacrificial layers, TiO_2 exhibits the smallest layer thickness (~1.2 nm), corresponding to a length-to-thickness ratio of > 20,000.

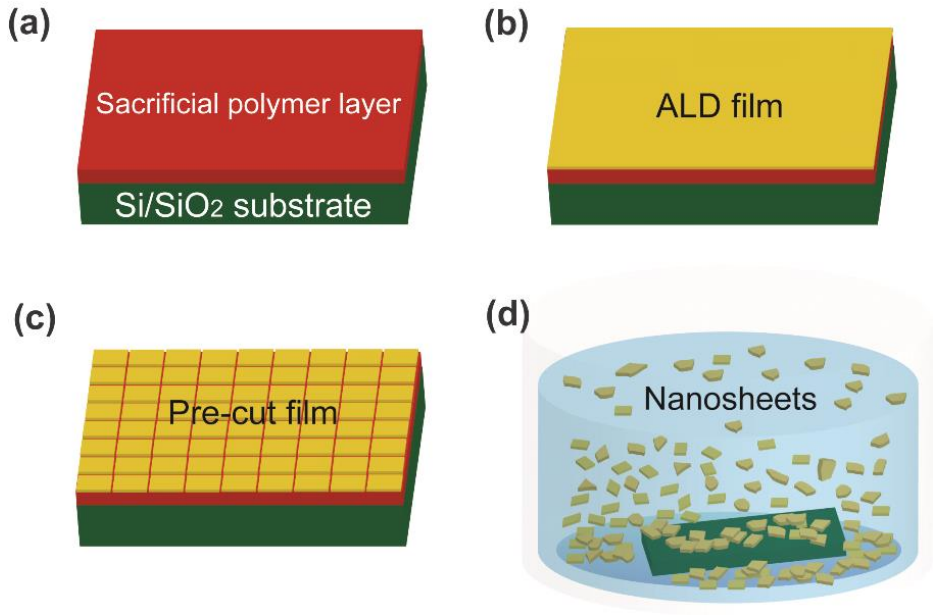

Figure 4.1 Fabrication of synthetic ALD nanosheets. (a) Polymer solution of 2 wt% was spin-coated on Si substrate as a sacrificial layer. (b) Metal oxide ALD was performed onto the polymer layer with desired thickness and materials. (c) Pre-cuts were made into the polymer surface to facilitate dissolution of the polymer. (d) The polymer was removed by dipping in a solvent and ALD films were separated as nanosheets randomly dispersed in aqueous solution.

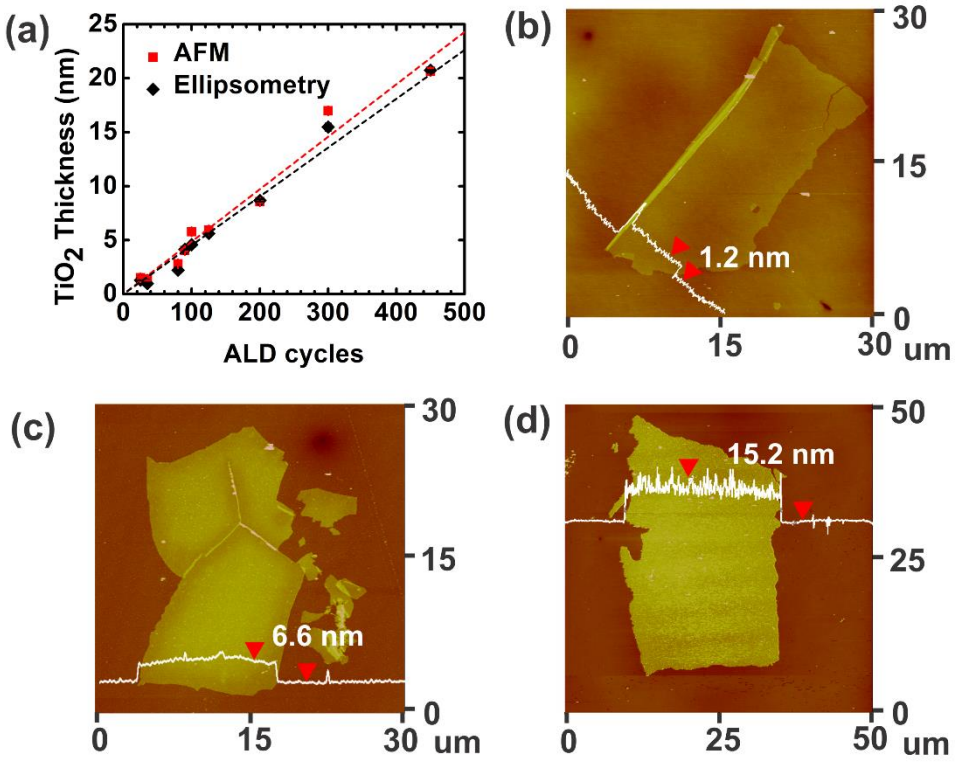

Figure 4.2 Microstructure of synthetic ALD nanosheets. (a) Graph of TiO_2 nanosheet thickness collected from AFM height profiles (squares) and from ellipsometry (diamonds) as a function of the number of ALD cycles. AFM images and height profiles of TiO_2 nanosheets from 25 ALD cycles (b), Al_2O_3 nanosheets from 50 ALD cycles (c), and ZnO nanosheet from 100 ALD cycles (d). These micrographs show the minimum nanosheet thickness achieved for each material.

To further study the resulting structure, nanosheets collected on molybdenum grids were annealed to 450 °C for TiO_2 and 300 °C for ZnO. This anneal step crystallized the TiO_2. TEM micrographs of these crystallized nanosheets are shown in Figure 4.3. In these images the thickness of the TiO_2 nanosheet is ~7.0 nm and the thickness of the ZnO nanosheet is ~17.3 nm. In Figure 4.3(a), the TiO_2 nanosheet exhibits a lattice spacing of 3.46 Å, which

corresponds to the *a* lattice parameter of the anatase phase of TiO_2.[20] The ZnO nanosheet shows a lattice spacing of 3.25 Å which matches the *a* lattice parameter for the wurtzite phase of ZnO (Figure 4.3b).[21]

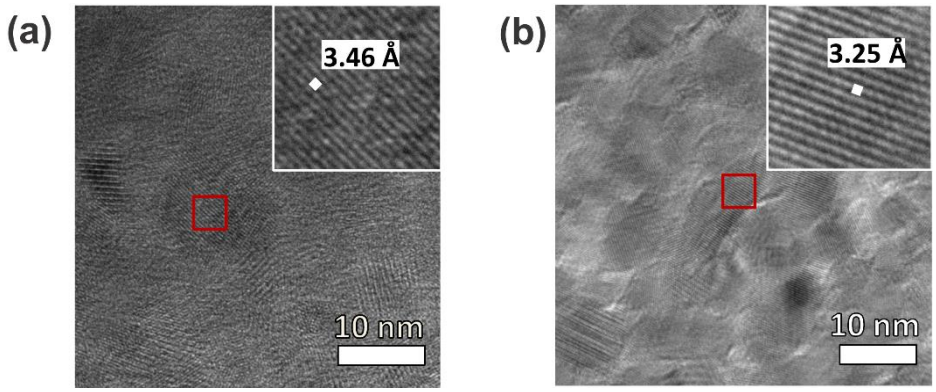

Figure 4.3 TEM images of TiO_2 nanosheet annealed at 450 °C for 1 h (e) and ZnO nanosheet annealed at 300 °C for 1 h (f). Magnified inset images obtained from the red areas show the lattice parameter for each material.

Besides single phase nanosheets, multicomponent and layered nanosheet structures can be designed by alternating ALD chemistries. As an example we have prepared bilayer nanosheets composed of TiO_2 and ZnO. Figure 4.4(a) shows the deposition scheme for these ALD nanosheet bilayers. In this experiment, PVA sacrificial layers were initially coated with ALD ZnO (150 cycles) followed by ALD TiO_2 (500 cycles). The inset in Figure 4.4(b) shows a scanning electron microscope (SEM) image of a ZnO/TiO_2 bilayer nanosheet transferred to a silicon substrate. Energy dispersive X-ray analysis (EDX) indicates the presence of Zn, Ti, and O, confirming that these bilayer structures remain intact after being

released from the sacrificial polymer. An AFM image of a similar nanosheet is shown in Figure 4.4(c), and Figure 4.4(d) shows a set of dispersed nanosheets in water. The AFM image shows the thickness is 36.9 nm where some double or triple layers result from nanosheet folding when it is collected on the planar substrate.

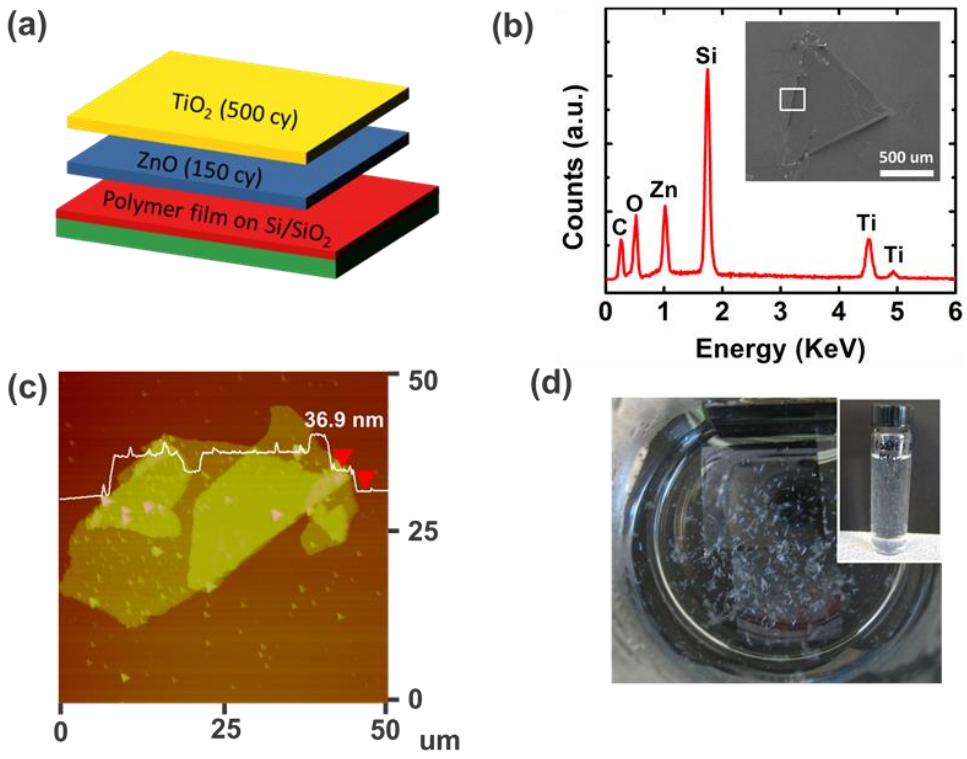

Figure 4.4 Bilayer nanosheets synthesized by ALD. (a) Illustration showing deposition order and the number of ALD cycles for the ZnO/TiO_2 bilayer film. (b) EDX spectrum taken from the edge of the bilayer nanosheet shown in the inset SEM image. (c) AFM image and height profile of the bilayer nanosheet. (d) Picture of TO_2/ZnO bilayer nanosheets dispersed in DI water and nanosheets collected in a vial (inset).

Many oxide nanomaterials can function as photocatalysts to degrade volatile organic pollutants and purify air or water.[22] Recently, multicomponent nanomaterials including TiO_2 with graphene,[23] TiO_2 nanofibers with ZnO,[24] and TiO_2 nanoparticles with carbon nanotubes[25] have shown improved performance relative to pure nano-TiO_2 evaluated under the same conditions. Improvements are typically associated with increased adsorption of organic species on the compound surface, extended range of photon absorption, and improved charge separation and transfer to the reacting species. The unique ability to control material thickness and synthesize bi-component compound nanosheets by ALD could provide new flexibility in photocatalyst materials design and preparation. Therefore, we have explored the photocatalytic performance of our TiO_2, ZnO, and TiO_2/ZnO bilayer ALD nanosheets in aqueous solution, including the scaling of photocatalytic rate processes with changing nanosheet thickness, surface area and electronic structure. We compare our experimental results to a standard analytical reaction model.

Here we use methyl orange as a prototypical pollutant. The derivation of the methyl orange photo-decomposition rate expression can be found in the section 4.4. The methyl orange concentration will scale as a log-linear function of irradiation time:

$$\ln\left(\frac{[C]}{[C]_0}\right) = -k^{"}S^2 I_0 D t = -Kt \qquad (1)$$

where $[C]$ [cm^{-3}] represents the concentration of methyl orange molecules in solution, t [s] is the irradiation time, S [cm^2] is the total surface area of TiO_2 nanosheets in the solution, I_0 [$\mu W cm^{-2}$] is the intensity of UV irradiation impinging on the nanosheets, D [nm] is the thickness of TiO_2 nanosheets, $k^{"}$ is an effective rate constant with units [$s^{-1}cm^{-2}\mu W^{-1}nm^{-1}$],

and K [s^{-1}] is the apparent rate constant. The analysis assumes that each nanosheet in solution receives the same uniform photon flux, which is best achieved for small values for S (i.e. solution with a relatively low concentration of nanosheets). The same general rate expression is expected to hold for the ZnO and bi-layer nanosheets.

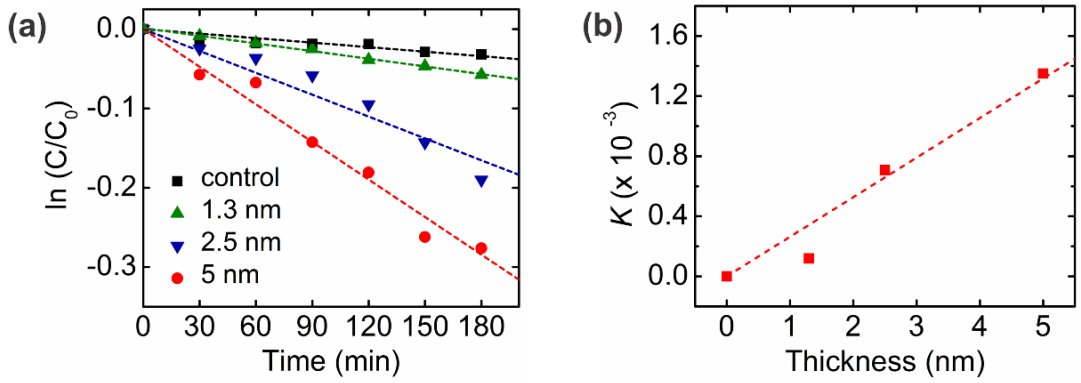

Figure 4.5 Photocatalytic behavior of synthetic ALD nanosheets. (a) The concentration of methyl orange versus UV exposure time onto TiO_2 nanosheets of various thickness (1.3, 2.5, and 5 nm). Black squares show the control data for methyl orange concentration versus time without nanosheets present. (b) Plot of apparent rate constants (*K)* versus surface area extracted from the data shown in (a).

Figure 4.5(a) shows the concentration of methyl orange as a function of UV exposure time in the presence of TiO_2 nanosheets using thickness values fixed between 1.3 and 5.0 nm. The total nanosheet surface area was 160 cm^2 and the UV flux was set at 245 $\mu W/cm^2$. All samples show dye absorbance loss upon UV exposure, with an increased rate of loss with increasing nanosheet thickness. From equation (1), the slopes of the linear fits in Figure 4.5(a) are a measure for $K = k''S^2 I_0 D$, and Figure 4.5(b) is a plot of K (from Figure 4.5a)

versus film thickness. *K* increases linearly with film thickness, as expected from equation (1). This result reflects the expected mechanistic trend where thicker nanosheets will absorb more photons and thereby boost the number of oxidizing species created. Using known values for *S* and I_o the linear fit in Figure 4.5(b) gives $k'' \approx 4.2\times10^{-11}$ $s^{-1}cm^{-2}\mu W^{-1}nm^{-1}$.

Dye decomposition rate data was also collected by irradiating TiO_2 nanosheet dispersions using various UV intensity values and nanosheet surface areas keeping other parameters fixed. Plots of ln (C/C_o) vs. time follow equation (1) (Figure 4.6a). Using S = 160 cm^2, a plot of K vs. I_o is linear with $k'' \approx 3.8\times10^{-11}$ $s^{-1}cm^{-2}\mu W^{-1}nm^{-1}$, essentially the same k'' value as from Figure 4.5(b) (Figure 4.6b).

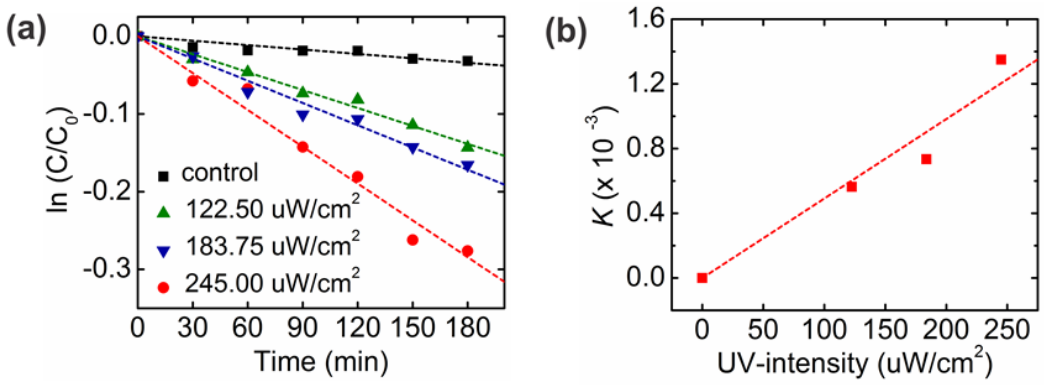

Figure 4.6 Dye degradation rate depending on UV intensity. (a) Degradation of methyl orange using photocatalytic TiO_2 nanosheets under varying UV intensity (122.50, 183.75, and 245.00 $\mu W/cm^2$). (b) Values of K obtained from the fits in (a) versus UV intensity. The value of k'' is 3.8×10^{-11} $s^{-1}cm^{-2}\mu W^{-1}nm^{-1}$.

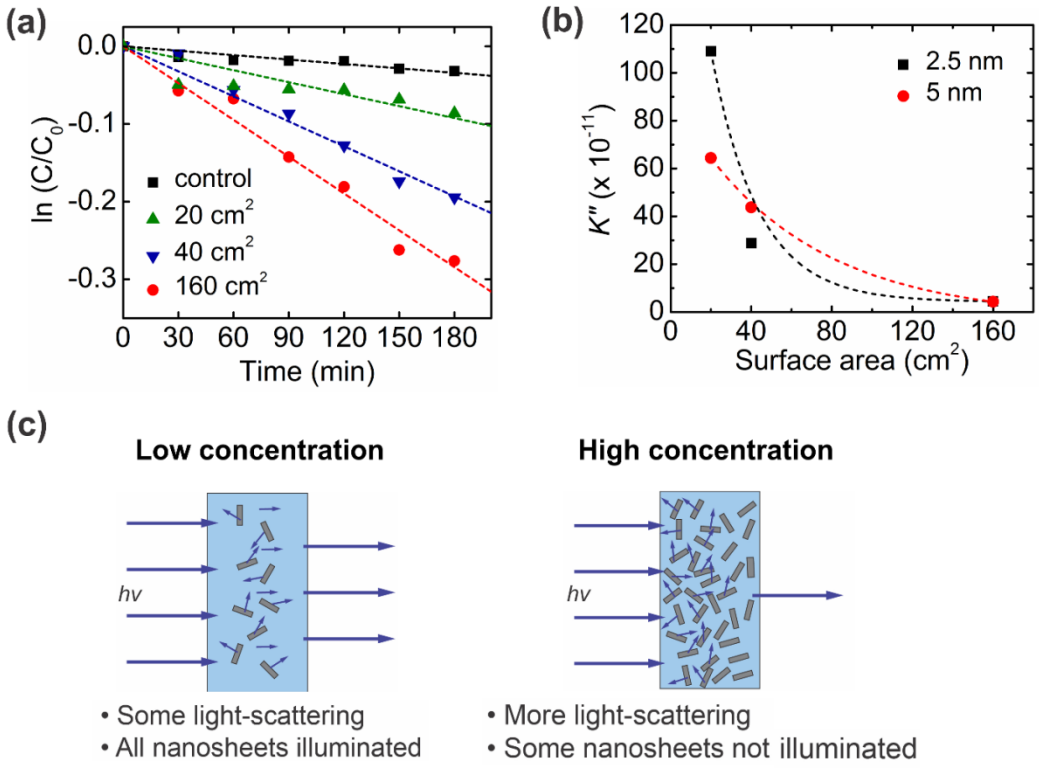

Figure 4.7 Dye degradation rate depending on concentration of nanosheets. (a) Degradation of methyl orange using photocatalytic TiO_2 nanosheets under varying surface area of nanosheets (20, 40, and 160 cm^2). (b) k'' values versus S for 2.5 nm (black square) and 5 nm (red circle) thickness. The k'' is expected to decrease with increasing S due to scattering effects. The dashed lines are guides for the eye. (c) Illustration that shows how surface area of nanosheets affects UV light scattering.

Increasing the surface area (by increasing nanosheet concentration) also affects the value of K. However, at high S (i.e., high nanosheet concentrations) we expect light scattering to decrease the photon flux on nanosheets deeper in solution. Using different S values, dye decomposition rate was measured using fixed D and I_o, and values for k'' were obtained for each condition (Figure 4.7a and b). We find larger values for k'' for smaller

values of *S* as expected from the model trend. Larger concentrations of nanosheets scatter light more strongly, decreasing the net photon flux on nanosheets deeper in the solution, thereby decreasing the effective rate of dye degradation, *k″* (Figure 4.7c).

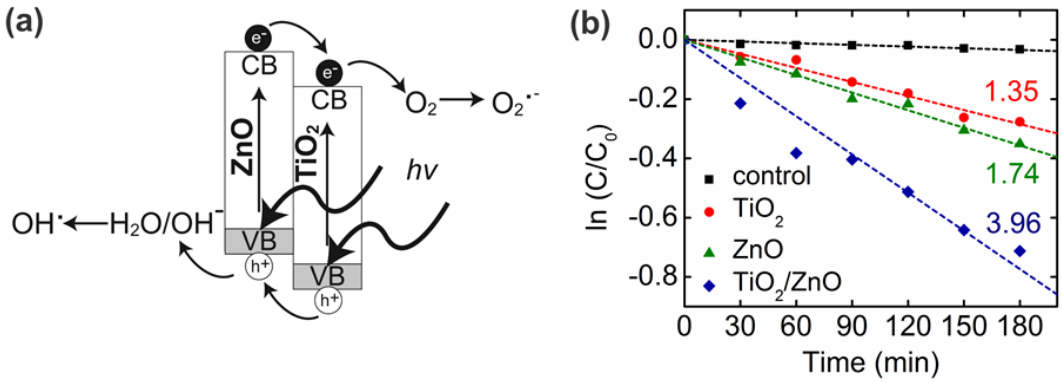

Figure 4.8 (a) Schematic band energy diagram of TiO_2/ZnO bilayer nanosheets. Photogenerated holes get trapped in the ZnO layer while photogenerated electrons become trapped in the TiO_2 layer, limiting recombination and enhancing photocatalytic performance. (b) Photodegradation of methyl orange with UV-irradiation time for control solution without nanosheets (black squares), TiO_2 nanosheets (red circles), ZnO nanosheets (green triangles), and ZnO/TiO_2 bilayer nanosheets (blue diamonds) of similar nanosheet thickness (5 nm) and concentration (160 cm^2). Each number represents *K* ($\times 10^{-3}$).

A distinctive aspect of ALD nanosheet synthesis is its facile ability to create compositional bi-layers with controlled thickness of each layer. Based on the two materials' difference in band energy levels[26], a TiO_2/ZnO bilayer structure will separate photogenerated electrons and holes as depicted in Figure 4.8(a). This charge separation should reduce recombination and increase the rate of photocatalytic degradation. Unlike other bi-component photocatalysts, our bi-layer nanosheets consist of two distinct material layers,

with the structure of a planar 'Janus nanosheet'.[27,28] Figure 4.8(b) plots methyl orange photodegradation using TiO_2, ZnO, and TiO_2/ZnO nanosheets with a thickness of 5 nm and a surface area of 160 cm^2. The *K* values extracted from these and other related degradation measurements are presented in Table 4.1. The ZnO nanosheets lead to modestly (~25%) faster organic photodegradation than TiO_2. Consistent with equation (1), the value of *K* increases linearly with nanosheet thickness.

Table 4.1 Rate of dye degradation. Taken from ln(C/Co) vs. time using eq. (1) for various nanosheet materials dispersed in aqueous solution. The photo intensity is fixed at I_0 = 245 $\mu W/cm^2$ and the overall surface area of the nanosheets is fixed at 160 cm^2. The TiO_2/ZnO nanosheets show more than a factor of 5 improved degradation rate compared to TiO_2 nanosheets alone.

Nanosheet Material	*Thickness (nm)*	*K ($\times 10^{-3} min^{-1}$)*
TiO_2	2.5	0.71
TiO_2	5	1.35
ZnO	5	1.74
TiO_2/ZnO	2.5/2.5	3.96

For the 5 nm thick bi-layer nanosheet (TiO_2/ZnO = 2.5/2.5 nm), the rate of dye degradation is >2.2× faster than for 5 nm thick TiO_2 or ZnO nanosheets and >5.5× faster than the 2.5 nm TiO_2 nanosheets alone. This result indicates that offsets between conduction band and valence band at the ZnO/TiO_2 interface are sufficient to separate photogenerated electrons and holes into the TiO_2 and ZnO layers, respectively. Even though the bi-layer structure was not optimized for relative performance, the measured rate enhancement is noteworthy when compared to other bi-component photocatalysts. For example, TiO_2/ZnO nanofibers[24] and Ag/TiO_2/ZnO composite particles[29] show rate enhancements up to 2× faster

than for TiO_2 alone. Also, adding carbon nanotubes[25,30] or graphene[23] can enhance the rate, but improvements are limited to ~3.1× better that TiO_2 alone. Therefore, the >5.5× rate enhancement obtained here for the bi-layer ALD nanosheets is notably better than previous reports.

We hypothesize that the physical symmetry of our bilayer structures contributes to the enhanced synergistic photodecomposition rates. Synthesis of most bi-component particles provides only modest control over size, shape, surface area and net amount of each component material. Our synthetic nanosheets have high surface-to-volume ratios, compositional symmetry, and individual layer thickness control to ensure that active redox species can readily access active surface sites, helping to balance the extent of the complementary surface oxidation and reduction reactions.

4.4. Photodegradation mechanism

A reasonable elementary reaction scheme for photodegradation of methyl orange on a photocatalytically active surface such as TiO_2 is given by[31,32]:

$$TiO_2 + h\nu \xrightarrow{k_1} TiO_2 + e^- + h^+$$

$$H_2O + S_v \overset{K_2}{\leftrightarrow} S\text{–}H_2O$$

$$OH^- + S_v \overset{K_3}{\leftrightarrow} S\text{–}OH^-$$

$$MO + S_v \overset{K_4}{\leftrightarrow} S\text{–}MO$$

$$S\text{–}H_2O + h^+ \xrightarrow{k_5} S\text{–}OH^\bullet + H^+$$

$S–OH^- + h^+ \xrightarrow{k_6} S–OH^\bullet$

$S–OH^\bullet + S–MO \xrightarrow{k_7}$ degradation products + $2S_v$

$S–OH^\bullet \xrightarrow{k_8} OH^\bullet + S_v$

Here, MO is methyl orange dye and Sv is a vacant adsorption site on the TiO_2 surface. $S–H_2O$, $S–OH^-$, S–MO, and $S–OH^\bullet$ represent adsorbed species on active TiO_2 surface sites. The *k*'s are rate constants for irreversible reactions, and the *K*'s represent equilibrium constants for reversible reactions. Generally, the UV photons generate electron-hole pairs in TiO_2, and the holes migrate to the surface and react with adsorbed water molecules and hydroxyl ions. The resulting hydroxyl radicals oxidize the methyl orange dye.

An overall rate expression is derived from the elementary reaction steps using the overall site balance and the steady-state approximation. The overall site balance is given by:

$$[S_t] = [S_v] + [S–H_2O] + [S–OH^-] + [S–MO]$$

where $[S_t]$ is total adsorption sites on all TiO_2 nanosheets, and $[S_v]$ is vacant adsorption sites on all TiO_2 nanosheets, and the steady state approximation is given by

$$\frac{d[H^+]}{dt} = \frac{d[S–OH^\bullet]}{dt} = 0$$

We also assume: 1) the generation of h^+ and e^- ≫ recombination of h^+ and e^-; 2) photon intensity that reaches each nanosheet surface is equal for all nanosheets in the solution; 3) the adsorption sites on the nanosheet are occupied primarily by H_2O: $[S–H_2O] \gg [S–OH^-]$ or [S–MO]; and 4) [MO] is very small and $[H_2O]$ is constant.

The rate of methyl orange decomposition is written as

$$r_{MO} = -\frac{d[MO]}{dt} = k_7[S-OH^{\bullet}][S-MO] \quad (1)$$

From the steady state approximation:

$$\frac{d[S-OH^{\bullet}]}{dt} = 0 = k_5[S–H_2O][h^+] + k_6[S–OH^-][h^+] - k_7[S–OH^{\bullet}][S–MO] - k_8[S–OH^{\bullet}]$$

$$[S-OH^{\bullet}] = \frac{k_5[S-H_2O][h^+] + k_6[S-OH^-][h^+]}{k_7[S-MO] + k_8} \quad (2)$$

$$\frac{d[H^+]}{dt} = 0 = k_1[TiO_2][hv] - k_5[S–H_2O][h^+] - k_6[S–OH^-][h^+]$$

$$[h^+] = \frac{k_1[TiO_2][hv]}{k_5[S-H_2O] + k_6[S-OH^-]} \quad (3)$$

Substituting equation (3) into equation (2),

$$[S-OH^{\bullet}] = \frac{k_5[S-H_2O] + k_6[S-OH^-]}{k_7[S-MO] + k_8} \times \frac{k_1[TiO_2][hv]}{k_5[S-H_2O] + k_6[S-OH^-]} = \frac{k_1[TiO_2][hv]}{k_7[S-MO] + k_8} \quad (4)$$

And putting (4) into (1),

$$\frac{d[MO]}{dt} = -k_7[S-OH^{\bullet}][S-MO] = -k_7[S-MO]\frac{k_1[TiO_2][hv]}{k_7[S-MO] + k_8} = \frac{-k_1[TiO_2][hv]}{1+\frac{k_8}{k_7[S-MO]}}$$

(5)

Because the adsorption sites are occupied primarily by H_2O, $[S–H_2O] \gg [S–OH^-]$ or [S–MO] (assumption 3 above):

$$[S_t] = [S_v] + [S–H_2O] + [S–OH^-] + [S–MO] = [S_v] + [S–H_2O]$$

$$K_2 = \frac{[S-H_2O]}{[H_2O][S_v]} = \frac{[S-H_2O]}{[H_2O]([S_t]-[S-H_2O])}$$

$$K_2[H_2O]([S_t] – [S–H_2O]) = [S–H_2O] \rightarrow [S–H_2O]\,(1 + K_2[H_2O]\,) = K_2[H_2O][S_t]$$

Therefore:

$$[\text{S–H}_2\text{O}] = \frac{K_2[H_2O][S_t]}{1 + K_2[H_2O]} \tag{6}$$

The equilibrium constant for the elementary reaction (4) is given by:

$$K_4 = \frac{[S-MO]}{[MO][S_v]} \rightarrow [\text{S–MO}] = K_4[\text{MO}][\text{S}_v] = K_4[\text{MO}]([\text{S}_t] - [\text{S–H}_2\text{O}])$$

We next substitute the value for [S–H_2O] from equation (6) into K_4 and obtain:

$$[S - MO] = K_4[\text{MO}]([\text{S}_t] - \frac{K_2[H_2O][S_t]}{1 + K_2[H_2O]}) = K_4[\text{MO}][\text{S}_t](1 - \frac{K_2[H_2O]}{1 + K_2[H_2O]})$$

$$= \frac{K_4[\text{MO}][\text{S}_t]}{1 + K_2[H_2O]} \tag{7}$$

Substituting (7) into (5), we obtain:

$$\frac{d[MO]}{dt} = \frac{-k_1[TiO_2][hv]}{1+\frac{k_8}{k_7[S-MO]}} = \frac{-k_1[TiO_2][hv]}{1+\frac{k_8\,(1 + K_2[H_2O])}{k_7K_4[\text{MO}][\text{S}_t]}}$$

Then, since [MO] is small (assumption 4 above),

$$\frac{d[MO]}{dt} = \frac{-k_1k_7K_4[\text{MO}][\text{S}_t][TiO_2][hv]}{k_8\,(1 + K_2[H_2O])} = -k'[S_t][TiO_2][hv][MO]$$

where, $k' \equiv \frac{K_4k_7k_1}{k_8(1 + K_2[H_2O])}$

In this expression, $[TiO_2]$ is the surface area of nanosheets per unit volume of solution [cm^2/cm^3] and $[h\nu]$ is the number of incident photons per unit area that create an electron/hole pair per unit time. The number of electron/hole pairs created per unit volume of solution per unit time is therefore $[TiO_2][hv]$. Using the Beer-Lambert Law, $I = I_0e^{-\alpha D}$ where I is the photon intensity per unit area [W/m^2], α is the absorption coefficient for TiO_2 at a given energy [nm^{-1}] and D is the thickness of the nanosheet [nm], the energy absorbed by a nanosheet within thickness D per unit area per time is $I_0(1 - e^{-\alpha D})$ [$J/cm^2 \cdot s$]. In the

energy region where the absorption coefficient is large, the number of charges generated is estimated by integrating the absorbed intensity across the film thickness *D*:

$$\int_0^D I_0(1 - e^{-\alpha D})\, dD = aI_0 \left(D + \frac{1}{\alpha}e^{-\alpha D} - \frac{1}{\alpha}\right) = I_0 D$$

where for large very α and small *D*, $\left(\frac{1}{\alpha}e^{-\alpha D} - \frac{1}{\alpha}\right) \rightarrow 0$. The photon flux versus photon energy is related to the irradiance of the light source. If *a* is the fraction of photons in the incident light with $h\nu > E_g$, then when D is small relative to 1/α, the number of photons that create electron hole pairs in the nanosheets present in solution is given by

$$[TiO_2][h\nu] = aI_0 DS/2 \text{ [μW nm]}$$

where *S* is the total surface area (front plus back) of all nanosheets in solution, and the factor of 2 arises since photons are incident on only one side of the nanosheet. Therefore:

$$\frac{d[MO]}{dt} = -k'[S_t][TiO_2][h\nu][MO] = -ak' S_t I_0 D \frac{S}{2}[MO]$$

Since $[S_t]$ is proportional to *S*, and we can write $k'' = ak'/2$, we obtain

$$\frac{d[MO]}{[MO]} = -k'' S^2 I_0 D dt$$

where, the final substitution $K \equiv k'' S^2 I_0 D$ [s^{-1}] gives

$$\boxed{\ln \frac{C}{C_0} = -k'' S^2 I_0 D t = -Kt}$$

4.5 Summary

In summary, we have shown how ALD thin film reactions can produce synthetic metal oxide nanosheets with precisely controlled thickness and aspect ratios of > 20,000:1.

Single component nanosheets composed of TiO_2 and ZnO exhibit photocatalytic activity, and the catalytic dye decomposition rate scales as expected with photodecomposition kinetic rate equations developed for the nanosheet structures. Photocatalytic decomposition rates are significantly boosted using ZnO/TiO_2 bilayer nanosheets, and the synergistic rate enhancement is larger than previously reported for other bi-component photocatalyst materials. The ALD synthesis process is unique in that it yields physically symmetric nanosheets, and the symmetry likely helps balance redox rates and thereby assists in achieving high performance. ALD also enables multi-component nanosheet junctions which modulate the nanosheet electronic band structure and synergistically enhance the rate of photocatalytic pollutant degradation. The addition of sensitizing dyes or catalytic sites before release could further expand nanosheet functionality and performance. These initial demonstrations of functional synthetic nanosheets by ALD suggest that a much broader set of materials, including metals, semiconductors, ceramics, organics and organic-inorganic hybrid materials could be produced in nanosheet form and evaluated for catalytic or other useful functions.

References

(1) Osada, M.; Sasaki, T. Exfoliated oxide nanosheets: new solution to nanoelectronics. *J. Mater. Chem.* **2009,** 19, 2503.

(2) Ebina, Y.; Sakai, N.; Sasaki, T. Photocatalyst of lamellar aggregates of RuOx-loaded perovskite nanosheets for overall water splitting. *J. Phys. Chem. B* **2005,** 109, 17212.

(3) Sasaki, T.; Watanabe, M.; Hashizume, H.; Yamada, H.; Nakazawa, H. Macromolecule-like aspects for a colloidal suspension of an exfoliated titanate. Pairwise association of nanosheets and dynamic reassembling process initiated from it. *J. Am. Chem. Soc.* **1996,** 118, 8329.

(4) Omomo, Y.; Sasaki, T.; Wang, L. Z.; Watanabe, M. Redoxable nanosheet crystallites of MnO_2 derived via delamination of a layered manganese oxide. *J. Am. Chem. Soc.* **2003,** 125, 3568.

(5) Coleman, J. N.; Lotya, M.; O'Neill, A.; Bergin, S. D.; King, P. J.; Khan, U.; Young, K.; Gaucher, A.; De, S.; Smith, R. J.; Shvets, I. V.; Arora, S. K.; Stanton, G.; Kim, H. Y.; Lee, K.; Kim, G. T.; Duesberg, G. S.; Hallam, T.; Boland, J. J.; Wang, J. J.; Donegan, J. F.; Grunlan, J. C.; Moriarty, G.; Shmeliov, A.; Nicholls, R. J.; Perkins, J. M.; Grieveson, E. M.; Theuwissen, K.; McComb, D. W.; Nellist, P. D.; Nicolosi, V. Two-dimensional nanosheets produced by liquid exfoliation of layered materials. *Science* **2011,** 331, 568.

(6) Ida, S.; Ogata, C.; Eguchi, M.; Youngblood, W. J.; Mallouk, T. E.; Matsumoto, Y. Photoluminescence of perovskite nanosheets prepared by exfoliation of layered oxides,

$K_2Ln_2Ti_3O_{10}$, $KLnNb_2O_7$, and $RbLnTa_2O_7$ (Ln : lanthanide ion). *J. Am. Chem. Soc.* **2008,** 130, 7052.

(7) Ebina, Y.; Sasaki, T.; Harada, M.; Watanabe, M. Restacked perovskite nanosheets and their Pt-loaded materials as photocatalysts. *Chem. Mater.* **2002,** 14, 4390.

(8) Chen, S. J.; Liu, Y. C.; Shao, C. L.; Mu, R.; Lu, Y. M.; Zhang, J. Y.; Shen, D. Z.; Fan, X. W. Structural and optical properties of uniform ZnO nanosheets. *Adv. Mater.* **2005,** 17, 586.

(9) Hu, J. Q.; Bando, Y.; Zhan, J. H.; Li, Y. B.; Sekiguchi, T. Two-dimensional micrometer-sized single-crystalline ZnO thin nanosheets. *Appl. Phys. Lett.* **2003,** 83, 4414.

(10) Novoselov, K. S.; Geim, A. K.; Morozov, S. V.; Jiang, D.; Zhang, Y.; Dubonos, S. V.; Grigorieva, I. V.; Firsov, A. A. Electric field effect in atomically thin carbon films. *Science* **2004,** 306, 666.

(11) Geim, A. K.; Novoselov, K. S. The Rise of graphene. *Nat. Mater.* **2007,** 6, 183.

(12) Radisavljevic, B.; Radenovic, A.; Brivio, J.; Giacometti, V.; Kis, A. Single-layer MoS_2 transistors. *Nat. Nanotechnol.* **2011,** 6, 147.

(13) Schliehe, C.; Juarez, B. H.; Pelletier, M.; Jander, S.; Greshnykh, D.; Nagel, M.; Meyer, A.; Foerster, S.; Kornowski, A.; Klinke, C.; Weller, H. Ultrathin PbS sheets by two-dimensional oriented attachment. *Science* **2010,** 329, 550.

(14) Feng, J.; Peng, L. L.; Wu, C. Z.; Sun, X.; Hu, S. L.; Lin, C. W.; Dai, J.; Yang, J. L.; Xie, Y. Giant moisture responsiveness of VS_2 ultrathin nanosheets for novel touchless positioning interface. *Adv. Mater.* **2012,** 24, 1969.

(15) Miikkulainen, V.; Leskela, M.; Ritala, M.; Puurunen, R. L. Crystallinity of inorganic films grown by atomic layer deposition: Overview and general trends. *J. Appl. Phys.* **2013,** 113, 021301.

(16) Parsons, G. N.; George, S. M.; Knez, M. Progress and future directions for atomic layer deposition and ALD-based chemistry. *MRS Bull.* **2011,** 36, 865.

(17) D'Arcy, J. M.; Tran, H. D.; Tung, V. C.; Tucker-Schwartz, A. K.; Wong, R. P.; Yang, Y.; Kaner, R. B. Versatile solution for growing thin films of conducting polymers. *Proc. Natl. Acad. Sci. USA* **2010,** 107, 19673.

(18) Peng, Q.; Sun, X. Y.; Spagnola, J. C.; Hyde, G. K.; Spontak, R. J.; Parsons, G. N. Atomic layer deposition on electrospun polymer fibers as a direct route to Al_2O_3 microtubes with precise wall thickness control. *Nano Lett.* **2007,** 7, 719.

(19) Linder, V.; Gates, B. D.; Ryan, D.; Parviz, B. A.; Whitesides, G. M. Water-soluble sacrificial layers for surface micromachining. *Small* **2005,** 1, 730.

(20) Asahi, R.; Taga, Y.; Mannstadt, W.; Freeman, A. J. Electronic and optical properties of anatase TiO_2. *Phys. Rev. B* **2000,** 61, 7459.

(21) Pan, Z. W.; Dai, Z. R.; Wang, Z. L. Nanobelts of semiconducting oxides. *Science* **2001,** 291, 1947.

(22) Gaya, U. I.; Abdullah, A. H. Heterogeneous photocatalytic degradation of organic contaminants over titanium dioxide: a review of fundamentals, progress and problems. *J. Photochem. Photobiol. C* **2008,** 9, 1.

(23) Zhang, Y. H.; Tang, Z. R.; Fu, X. Z.; Xu, Y. J. TiO_2-graphene nanocomposites for gas-phase photocatalytic degradation of volatile aromatic pollutant: Is TiO_2-graphene truly different from other TiO_2-carbon composite materials? *ACS Nano* **2010,** 4, 7303.

(24) Liu, R. L.; Ye, H. Y.; Xiong, X. P.; Liu, H. Q. Fabrication of TiO_2/ZnO composite nanofibers by electrospinning and their photocatalytic property. *Mater. Chem. Phys.* **2010,** 121, 432.

(25) Yu, Y.; Yu, J. C.; Chan, C. Y.; Che, Y. K.; Zhao, J. C.; Ding, L.; Ge, W. K.; Wong, P. K. Enhancement of adsorption and photocatalytic activity of TiO_2 by using carbon nanotubes for the treatment of azo dye. *Appl. Catal. B* **2005,** 61, 1.

(26) Mane, R. S.; Lee, W. J.; Pathan, H. M.; Han, S. H. Nanocrystalline TiO_2/ZnO thin films: Fabrication and application to dye-sensitized solar cells. *J. Phys. Chem. B* **2005,** 109, 24254.

(27) Perro, A.; Reculusa, S.; Ravaine, S.; Bourgeat-Lami, E.; Duguet, E. Design and synthesis of Janus micro-and nanoparticles. *J. Mater. Chem.* **2005,** 15, 3745.

(28) Liang, F.; Shen, K.; Qu, X.; Zhang, C.; Wang, Q.; Li, J.; Liu, J.; Yang, Z. Inorganic Janus Nanosheets. *Angew. Chem. Int. Ed.* **2011,** 50, 2379.

(29) Pant, H. R.; Pant, B.; Sharma, R. K.; Amarjargal, A.; Kim, H. J.; Park, C. H.; Tijing, L. D.; Kim, C. S. Antibacterial and photocatalytic properties of Ag/TiO_2/ZnO nano-flowers prepared by facile one-pot hydrothermal process. *Ceram. Int.* **2013,** 39, 1503.

(30) Wang, H.; Dong, S.; Chang, Y.; Faria, J. L. Enhancing the photocatalytic properties of TiO_2 by coupling with carbon nanotubes and supporting gold. *J. Hazard. Mater.* **2012,** 235–236, 230.

(31) Barka, N.; Qourzal, S.; Assabbane, A.; Ait-Ichou, Y. Kinetic modeling of the photocatalytic degradation of methyl orange by supported TiO_2. *J. Environ. Sci. Eng.* **2010,** 4, 1.

(32) Konstantinou, I. K.; Albanis, T. A. TiO_2-assisted photocatalytic degradation of azo dyes in aqueous solution: kinetic and mechanistic investigations - A review. *Appl. Catal. B* **2004,** 49, 1.

Chapter 5

Effects of Sacrificial Polymers and Materials on Nanosheets Synthesis by Atomic Layer Deposition

This chapter is being prepared for publication.

Abstract

Two dimensional nanosheets with distinctive properties have been fabricated by exfoliation, hydrothermal synthesis, or vapor phase reaction, and other synthetic methods. While these approaches are generally limited to materials with known chemical composition, we recently showed that atomic layer deposition (ALD) can be used to produce synthetic metal oxide nanosheets with controlled thickness and chemical composition, including capacity for multicomponent nanosheets.[1] Specifically, we showed that TiO_2/ZnO (2.5 nm/2.5 nm) bi-layer nanosheets could be produced, and photocatalysis experiments led to ~5 times faster dye degradation compared to single-component TiO_2 nanosheets (2.5 nm) produced by the same process, which is significant improvement compared to other bi-component photocatalytic systems. Here, we describe how the sacrificial substrate polymer affects subsequent ALD processing and the resulting nanosheet thickness and surface structure. In addition, we introduce the concept of organic/inorganic bi-layer sheets and discuss their potential application.

5.1 Introduction

Recently, many types of 2D nanosheet materials are being developed and modified for applications in nanoelectronics,[2] biomedicine,[3,4] energy storage devices,[5] or biomaterial systems.[6] Since graphene was first isolated from graphite in 2004,[7] a vast amount of research has revealed its unusual electronic and physical properties such as high electron mobility and quantum Hall effects.[8,9] While graphene has a potential application as a conductor, various oxides[10] including perovskite[11] which have naturally stacked molecular structures also show semiconducting or high κ-dielectric properties.[12]

Table 1 summarizes fabrication methods and thickness range for several natural nanosheet materials studied to date. The two primary methods for nanosheet fabrication are hydrothermal synthesis and exfoliation from layered compound.[13-17] Since exfoliation is applied for compounds with naturally stacked molecular structure, it normally produces thinner nanosheets than other methods. Other functional materials, such as Ag, Au, or Pt nanoparticles are often added to nanosheets to enhance performance in biosensor, batteries, or solar cell structures.[18-21] The unique functionality of 2D nanosheets is determined to a large extent by the electronic structure associated with full crystallinity, well-defined electronic surface termination and occupation, as well as the planar morphology and high surface area. The 2D graphene electronic structure rapidly changes with increasing layers, reaching its full 3D limit at ~10 graphene multilayers,[8] a few nanometers thick. Previously, we showed that atomic layer deposition (ALD) can be used fabricate free-floating metal oxide nanosheets with thickness in the range of 2D electronic materials.[1] While the ALD

materials do not have full crystalline morphology and well-defined regular surface structure of graphene or other 2D solids, the ALD process provides several unique advantages for 2D structure synthesis: 1) access to a wide material set, beyond known 2D crystal materials; 2) direct scalability to large areas with well controlled thickness; and 3) facile fabrication of multi-component heterojunctions and other multiple compound layered structures. We showed for example, that TiO_2 and ZnO nanosheets had photocatalytic functionality, and the rates of photocatalytic decomposition followed expected trends in light intensity and thickness. More importantly, bi-layer nanosheets composed of TiO_2/ZnO (2.5 nm/2.5 nm) improve dye degradation rate by ~5 times than TiO_2 nanosheets (2.5 nm). More detailed analysis of the ALD film nucleation, and how it is affected by precursor and substrate choice, will be important to further tune and optimize 2D ALD materials fabrication.

Here, we report in detail the effects of polymers used as a sacrificial layer and ALD materials on nanosheet synthesis. Specific sacrificial polymer substrates include poly methylmethacrylate (PMMA), poly vinyl alcohol (PVA), and poly acrylic acid (PAA). We observed that poly (vinyl alcohol) is most suitable to separate ALD film with larger size among the tested polymers. From PVA sacrificial layers, thicknesses of nanosheets are linearly fitted well with ALD film thicknesses. Also, Al_2O_3 nanosheets from 5 and 100 ALD cycles show a rough surface formed during nucleation stage in a comparable range. In addition, two sacrificial polymer layers produced organic/inorganic sheets after one polymer was dissolved.

Table 5.1 Fabrication methods and thickness of nanosheets.

Methods	Materials		Thickness	Reference
Exfoliation	Graphene		< 1 nm	[22]
	MoS_2		< 1 nm	[23,24]
	MnO_2		< 1 nm	[25]
	BN		1 – 7 nm	[26]
	perovskite	$Ca_2Nb_3O_{10}$	~1 nm	[27]
		$K_2Ln_2Ti_3O_{10}$ $KLnNb_2O_7$ $RbLnTa_2O_7$	1 – 3 nm	[28]
Hydrothermal synthesis	NiO		30 – 50 nm	[29]
	ZnO		50 nm	[30]
	TiO_2		10 – 15 nm	[16,17]
	$BiVO_4$		10 – 40 nm	[31]
Thermal evaporation	Ga_2O_3		20 – 60 nm	[32]
	ZnS		tens of nm	[33]
ALD	Al_2O_3, ZnO, TiO_2		1 – 17 nm	[1]

Here, we report in detail the effects of polymers used as a sacrificial layer and ALD materials on nanosheet synthesis. Specific sacrificial polymer substrates include poly methylmethacrylate (PMMA), poly vinyl alcohol (PVA), and poly acrylic acid (PAA). We observed that poly (vinyl alcohol) is most suitable to separate ALD film with larger size among the tested polymers. From PVA sacrificial layers, thicknesses of nanosheets are linearly fitted well with ALD film thicknesses. Also, Al_2O_3 nanosheets from 5 and 100 ALD cycles show a rough surface formed during nucleation stage in a comparable range. In

addition, two sacrificial polymer layers produced organic/inorganic sheets after one polymer was dissolved.

5.2 Experimental

Sacrificial Polymer layer: Poly (acrylic acid) (PAA, Mw = 1,800) and poly (methyl methacrylate) (PMMA, Mw = 16,000 and 350,000) were purchased from Sigma-Aldrich. Poly (vinyl alcohol) (PVA, Mw = 16,000 with 98% hydrolysis and 95,000 with 95% hydrolysis) was purchased from Acros Organics. All polymers were used without further purification. The solvent for PVA and PAA was deionized (DI) water. PMMA was dissolved in toluene (anhydrous 99.8%) or tetrahydrofuran (THF, anhydrous 99.9%) purchased from Sigma-Aldrich. After dissolved in the solvents with 2 wt% concentration, they were spin-coated onto a Si/SiO_2 substrate for 30 s at 3000 rpm.

Atomic Layer Deposition: Atomic layer deposition was performed in a custom hot wall viscous flow tube reactor where each precursor was dosed alternatively at an operating pressure of 2 Torr. Nitrogen gas as the carrier and purge gas was purified before introducing into the reactor with an inert gas filter (Gatekeeper®, Entegris Inc.). Precursors for Al_2O_3 and ZnO were Trimethylaluminum (TMA, 98%) and diethylzinc (DEZ, 95%) respectively. Titanium tetrachloride ($TiCl_4$, 99%) was the precursor for TiO_2 ALD. All precursors were purchased from Strem Chemicals, Inc. Deionized (DI) water is the co-reactant for all ALD processes. ALD sequences are consisted of $[TMA/N_2/H_2O/N_2]$ = [1/30/1/60 s] and $[DEZ/N_2/H_2O/N_2]$ = [2/50/2/50 s] for Al_2O_3 and ZnO films, respectively. Partial pressure for TMA and DEZ was 0.1 – 0.2 Torr and deposition temperature was 90 °C. TiO_2 film was

deposited with the sequence of [$TiCl_4/N_2/H_2O/N_2$] = [1/40/1/40 s]. Partial pressure of $TiCl_4$ was 0.01 – 0.02 Torr and deposition temperature was 100 °C. For each run, the polymer-coated silicon substrate with total surface area of 4 cm^2 was loaded into the ALD reactor. As a control, and to provide independent analysis of the deposited film thickness, ALD layers were simultaneously deposited on clean oxidized silicon wafer pieces.

Nanosheet separation: In order to facilitate the dissolution of the polymer, the ALD film was cut with a razor blade. Then the substrate with ALD film on the polymer layer was dipped in the solvent with the temperature of 70 °C. The solvents used were toluene for PMMA and DI water for PVA and PAA. After several minutes, the nanosheets began to separate from the substrate and visibly appear in the solvent solution. For further analysis, they were collected on a clean Si/SiO_2 substrate and annealed at 450 – 500 °C for 1 h in air to remove residual polymer.

Characterization: ALD film thickness was measured with ellipsometry (Alpha-SE Ellipsometer, JA Woollam Co., Inc.) using a reference Si/SiO_2 substrate. Thickness of nanosheets was measured from atomic force microscopy (AFM, DI 3000) image after annealed at 450 °C for 1 h to remove residual polymers. Optical microscopic images were captured with an Olympus BX60 microscope.

5.3 Results & Discussion

PVA, PAA, and PMMA were used as a sacrificial layer. PVA and PAA provide good nucleation sites for ALD process with their hydroxyl groups (-OH).[34] Precursors react with hydroxyl groups on the film surface so that where adsorptions at the surface region are dominant.[35,36] Carbonyl groups (C=O) in PMMA also reacts with a precursor to initiate nucleation.[37] In case of PMMA, however, precursors can diffuse more through the polymer layers than PVA and PAA. Therefore, ALD films were easily torn when PMMA layer is dissolved in toluene as ALD film is thinner. When PAA was used as a sacrificial layer, it dissolved so quickly because of its high water solubility and low molecular weight,[38] so that most of ALD films were separated into small pieces less than 1 μm. Among these polymers, PVA produced the nanosheets up to ~5 mm as well as good solubility in water. Despite it took more time for PVA to dissolve in water than PAA, it helped ALD films to be separated stably in larger lateral size. Also, PVA of high molecular weight (95,000) leads to longer dissolution time than that of low molecular weight (16,000), which also happens for PMMA of low and high molecular weight. As a result, PVA with low molecular weight showed the best results of ALD film separation and the results in this paper were obtained using it if not specifically indicated.

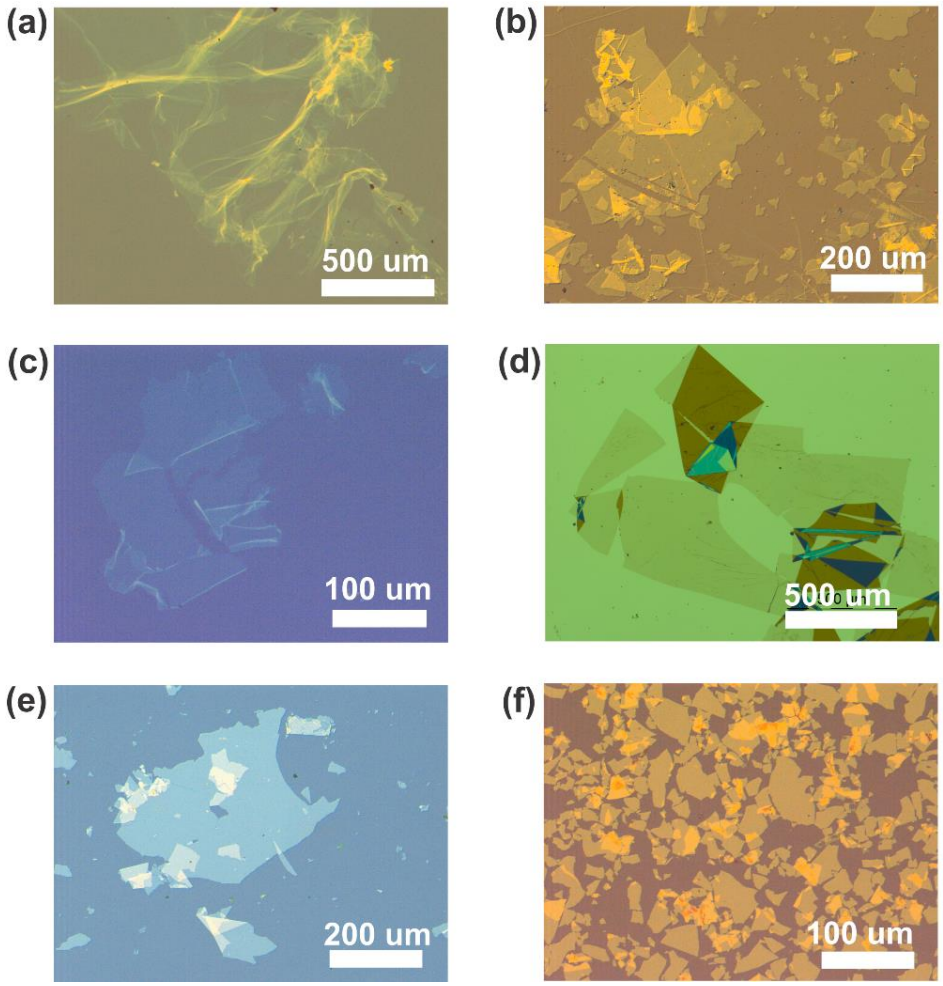

Figure 5.1 Optical microscopic images of Al_2O_3 nanosheets from (a) 10 cycles and (b) 50 cycles, TiO_2 nanosheets from (c) 25 cycles and (d) 300 cycles, and ZnO nanosheets from (e) 100 cycles and (f) 150 cycles.

Figure 5.1(a) – (f) are optical microscopic images of nanosheets. Al_2O_3 nanosheets from 10 cycles have round and flexible edges as shown in Figure 5.1(a). The flexibility of the nanosheets with ~1.1 nm thickness brings about the wrinkles and overlap in a nanosheet when collected on the new substrate. On the other hand, nanosheets from 50 cycles retain the

sharper shape generated when the ALD film is separated from the substrate (Figure 5.1b). Similarly, the edges of TiO_2 nanosheets with ~1.3 nm thickness are curved and rolled up (Figure 5.1c) while 15.5 nm-thick nanosheets have angular shape (Figure 5.1d). Difference on nanosheet color indicates how much nanosheet is overlapped. Figure 1a and 1c show the thinnest nanosheets for Al_2O_3 and TiO_2 confirmed visually with the optical microscope. We obtained Al_2O_3 nanosheets from 5 cycles which correspond to 0.8 nm and examined with AFM but it was difficult to get a microscopic image. Unlike Al_2O_3 and TiO_2, the thinnest ZnO nanosheets were 17.2 nm from 100 ALD cycles (Figure 5.1e). Below 100 cycles, the film was separated into small particles rather than sheets, which is attributed to the crystallinity of ZnO film. However, ZnO nanosheets were stably obtained as the film is thicker like other materials as shown in Figure 5.1(f).

Below 100 cycles, ZnO film was separated into small particles rather than sheets, which is attributed to the crystallinity of ZnO film. Figure 5.2(a) shows TEM image of ZnO nanosheets from ALD 50 cycles. They mostly have the size below 200 nm. Despite of the smaller size, crystallinity of ZnO is confirmed by TEM images shown in Figure 5.2(b), which shows α lattice spacing of wurtzite ZnO.[39]

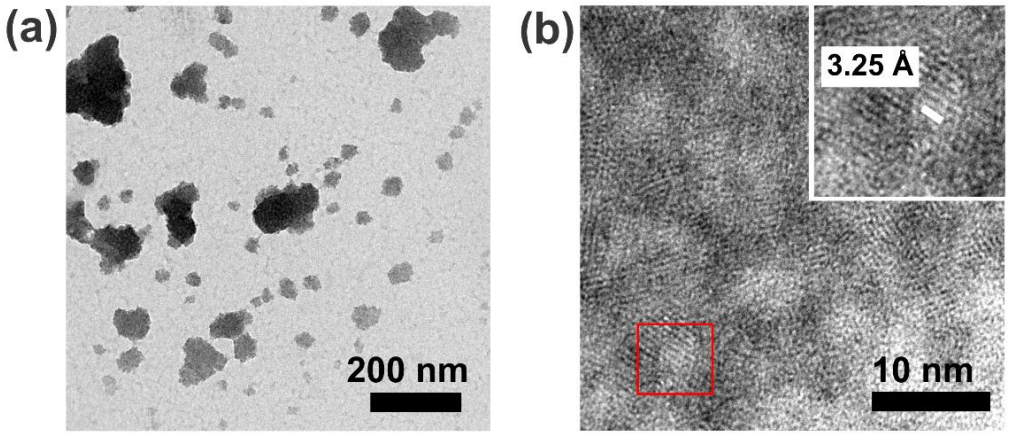

Figure 5.2 TEM images of ZnO nanosheets from ALD 50 cycles. (a) ZnO nanosheets show the size less than 200 nm and (b) lattice spacing of 3.25 Å confirms ZnO crystallinity.

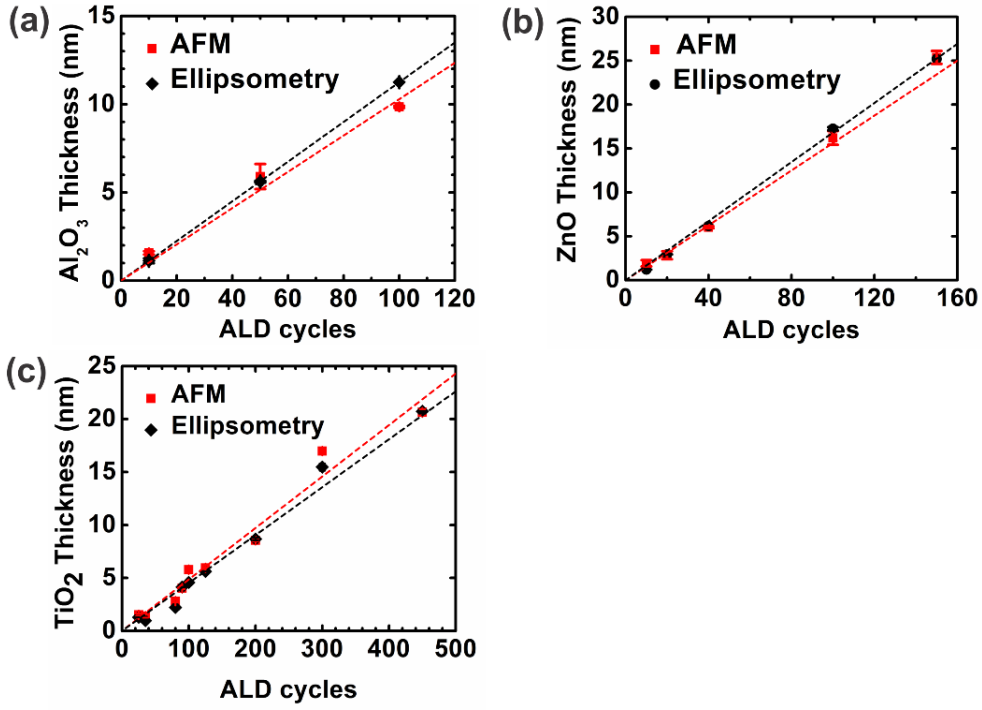

Figure 5.3 Graphs comparing the nanosheet thickness measured from AFM to the film thickness from ellipsometry depending on ALD cycles for (a) Al_2O_3, (b) ZnO, and (c) TiO_2

Thickness of nanosheet was obtained from the depth profile in AFM image. ALD film thickness was measured with a Si/SiO_2 wafer by ellipsometry for each ALD run. Figure 5.3 shows plots of thickness measured by AFM and ellipsometry as a function of ALD cycle number for Al_2O_3, ZnO, and TiO_2. In all cases, nanosheet thicknesses are fitted well with ALD film thicknesses. Even though ZnO ALD films below 100 cycles were separated into small particles so that they do not look like sheets, their thicknesses are still matched with ALD film thicknesses measured by ellipsometry (Figure 5.3b). These graphs indicate that ALD is an effective way for controlling nanosheet thickness regardless of the materials.

Figure 5.4(a) is an AFM image of Al_2O_3 nanosheet obtained after 5 ALD cycles with depth profile where the thickness of nanosheet is ~1.7 nm. The magnified scan image from the white dotted box in Figure 5.4(a) shows RMS roughness of 2.0 nm (Figure 5.4b). The Al_2O_3 nanosheet from ALD 100 cycles has rough surface as shown in an AFM depth profile (Figure 5.4c) and similar RMS of 1.8 nm with the nanosheet from ALD 5 cycles (Figure 5.4d). However, another nanosheet from the same ALD process shows a quite flat surface (Figure 5.4e). The RMS roughness measured with inside nanosheet is ~1.1 nm. Figure 5.4(f) is the AFM image of sacrificial PVA layer after spin coating with RMS of 0.5 nm. Therefore, Al_2O_3 nanosheets roughness does not resulted from the roughness of polymer layer. They may show a different side of Al_2O_3ALD film. During nucleation that happens for the first 20 cycles, small Al_2O_3 clusters form at the surface.[35,36] After these clusters cover and block the surface, a smooth film forms on that. Despite PVA has hydroxyl group reactive with precursor on the surface, so that precursor diffusion through PVA film is much less than other polymer like polypropylene or polyethylene, the diffusion in several nm could happen

on PVA film. Therefore, the nanosheet from 5 cycles which is in a nucleation stage has uneven surface in either side but freestanding nanosheets from 100 cycles have even and uneven surface from the top and bottom of ALD film. Since there is no preferable side when the nanosheets were collected on the new Si/SiO_2 substrate, both side can be shown as the surface.

We also explored creation of organic/inorganic bi-layer heterojunction nanosheets. The process started with a thin (~100 nm) sacrificial polymer (PVA) dissolved in DI water and spin-coated with a second solvent-resistant polymer (PMMA) dissolved in THF. Because the PVA and PMMA dissolve in different solvents, they are expected to be immiscible. The polymer stack is then exposed to 100 cycles of ALD TiO_2 at 100 °C. In this case, organic-inorganic hybrid film can be obtained during dissolution of one polymer. Figure 5.5(a) is TiO_2/PMMA bilayer sheets separated from the substrate when PVA layer was dissolved. Only with the edge and one cut inside the film, two large bilayer sheets were obtained. Also, when the film was cut in small rectangular shape, the bilayer sheets composed of ZnO (30 cycles) and PMMA layers were separated along the cut lines during PVA dissolution as shown in Figure 5.5(b). Many kinds of inorganic materials have been coordinated with organic materials to form organic-inorganic hybrid films based on synergetic interaction between organic and inorganic materials.[40] Stoock *et al*. demonstrated that free-standing polymer film with well-defined size and shape as well as controlled thickness.[41] Also, as organic/inorganic thin film, Vendemme *et al*. showed free-standing ~35 nm nanomembrane consisted of 5 nm PVA film and ~30 nm inorganic layers.[42] Our result first introduced ALD

as organic/inorganic hybrid films and they have potential for application in the fields of optics or biology.[43,44]

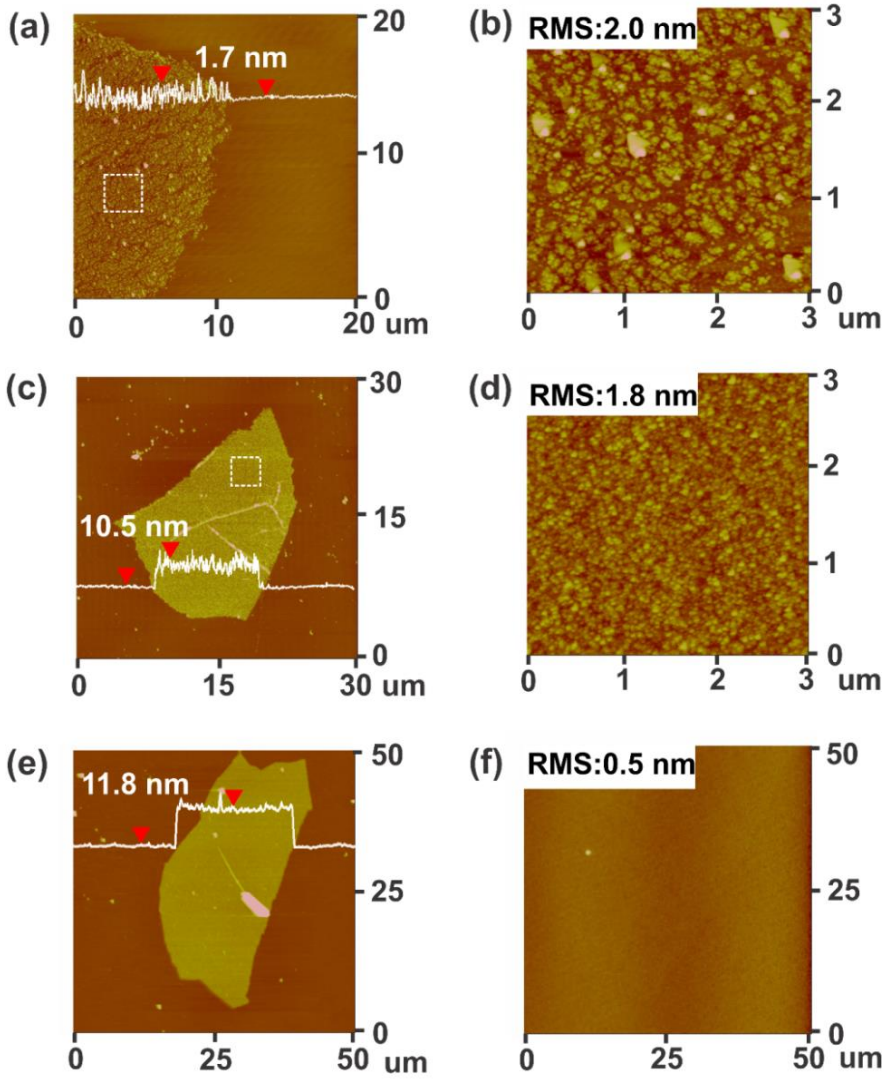

Figure 5.4 AFM image of Al_2O_3 nanosheet obtained from (a) ALD 5 cycles and (c) 100 cycles. (b) and (d) are the magnified images inside nanosheet marked with the dotted box from (a) and (b). (e) Al_2O_3 nanosheet from ALD 100 cycles with smooth surface. (f) AFM image of spin-coated PVA (Mw=16,000) used as a sacrificial layer.

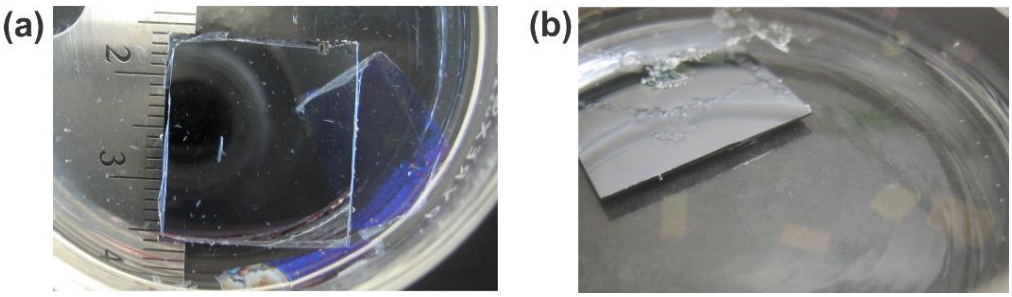

Figure 5.5 Pictures of (a) TiO_2/PMMA bilayer sheets separated during PAA dissolution and (b) ZnO/PMMA bilayer sheets during PVA dissolution.

5.4 Summary

In summary, we presented the effects of ALD materials, sacrificial polymers, and ALD cycles on the nanosheets synthesized by ALD. When PVA with Mw = 16,000 was used as a sacrificial polymer, TiO_2 nanosheets with high aspect ratio (up to 20,000) were stably obtained. Due to various crystallinity of ALD films, the minimum thickness of nanosheets that have lateral size of > ~1 μm depends on materials. ZnO ALD film that has high crystallinity produced nanosheets with the minimum thickness of ~17 nm, which is thicker than ~1 nm of TiO_2 or ~1.7 nm of Al_2O_3. Also, we introduced organic-inorganic sheets using double polymer layers before ALD, which can expand the application of ALD nanosheets to biomedicine or optics.

References

(1) Lee, K.; Losego, M. D.; Kim, D.; Parsons, G. N. High performance photocatalytic metal oxide synthetic nanosheets formed by atomic layer deposition. *Submitted* **2013**.

(2) Osada, M.; Sasaki, T. 2D oxide nanosheets: Controlled assembly and applications. *ECS Trans.* **2013,** 50, 111.

(3) Ventrelli, L.; Ricotti, L.; Menciassi, A.; Mazzolai, B.; Mattoli, V. Nanoscaffolds for guided cardiac repair: The new therapeutic challenge of regenerative medicine. *J. Nanomater.* **2013,** 2013.

(4) Miao, W.; Shim, G.; Lee, S.; Lee, S.; Choe, Y. S.; Oh, Y.-K. Safety and tumor tissue accumulation of pegylated graphene oxide nanosheets for co-delivery of anticancer drug and photosensitizer. *Biomaterials* **2013,** 34, 3402.

(5) Mhamane, D.; Suryawanshi, A.; Banerjee, A.; Aravindan, V.; Ogale, S.; Srinivasan, M. Non-aqueous energy storage devices using graphene nanosheets synthesized by green route. *AIP Advances* **2013,** 3, 042112.

(6) Nabetani, Y.; Takamura, H.; Hayasaka, Y.; Sasamoto, S.; Tanamura, Y.; Shimada, T.; Masui, D.; Takagi, S.; Tachibana, H.; Tong, Z.; Inoue, H. An artificial muscle model unit based on inorganic nanosheet sliding by photochemical reaction. *Nanoscale* **2013,** 5, 3182.

(7) Novoselov, K. S.; Geim, A. K.; Morozov, S.; Jiang, D.; Zhang, Y.; Dubonos, S.; Grigorieva, I.; Firsov, A. Electric field effect in atomically thin carbon films. *Science* **2004,** 306, 666.

(8) Geim, A. K.; Novoselov, K. S. The rise of graphene. *Nat. Mater.* **2007,** 6, 183.

(9) Neto, A. C.; Guinea, F.; Peres, N.; Novoselov, K.; Geim, A. The electronic properties of graphene. *Rev. Mod. Phy.* **2009,** 81, 109.

(10) Ma, R. Z.; Sasaki, T. Nanosheets of oxides and hydroxides: Ultimate 2D charge-bearing functional crystallites. *Adv. Mater.* **2010,** 22, 5082.

(11) Takagaki, A.; Sugisawa, M.; Lu, D. L.; Kondo, J. N.; Hara, M.; Domen, K.; Hayashi, S. Exfoliated nanosheets as a new strong solid acid catalyst. *J. Am. Chem. Soc.* **2003,** 125, 5479.

(12) Osada, M.; Ebina, Y.; Funakubo, H.; Yokoyama, S.; Kiguchi, T.; Takada, K.; Sasaki, T. High-κ dielectric nanofilms fabricated from titania nanosheets. *Adv. Mater.* **2006,** 18, 1023.

(13) Coleman, J. N.; Lotya, M.; O'Neill, A.; Bergin, S. D.; King, P. J.; Khan, U.; Young, K.; Gaucher, A.; De, S.; Smith, R. J.; Shvets, I. V.; Arora, S. K.; Stanton, G.; Kim, H. Y.; Lee, K.; Kim, G. T.; Duesberg, G. S.; Hallam, T.; Boland, J. J.; Wang, J. J.; Donegan, J. F.; Grunlan, J. C.; Moriarty, G.; Shmeliov, A.; Nicholls, R. J.; Perkins, J. M.; Grieveson, E. M.; Theuwissen, K.; McComb, D. W.; Nellist, P. D.; Nicolosi, V. Two-dimensional nanosheets produced by liquid exfoliation of layered materials. *Science* **2011,** 331, 568.

(14) Stankovich, S.; Dikin, D. A.; Piner, R. D.; Kohlhaas, K. A.; Kleinhammes, A.; Jia, Y.; Wu, Y.; Nguyen, S. T.; Ruoff, R. S. Synthesis of graphene-based nanosheets via chemical reduction of exfoliated graphite oxide. *Carbon* **2007,** 45, 1558.

(15) Ma, R.; Liu, Z.; Li, L.; Iyi, N.; Sasaki, T. Exfoliating layered double hydroxides in formamide: a method to obtain positively charged nanosheets. *J. Mater. Chem.* **2006,** 16, 3809.

(16) Xiang, Q.; Lv, K.; Yu, J. Pivotal role of fluorine in enhanced photocatalytic activity of anatase TiO_2 nanosheets with dominant (0 0 1) facets for the photocatalytic degradation of acetone in air. *Appl. Catal. B* **2010,** 96, 557.

(17) Yu, J.; Fan, J.; Lv, K. Anatase TiO_2 nanosheets with exposed (001) facets: improved photoelectric conversion efficiency in dye-sensitized solar cells. *Nanoscale* **2010,** 2, 2144.

(18) Liu, J.; Fu, S.; Yuan, B.; Li, Y.; Deng, Z. Toward a universal "adhesive nanosheet" for the assembly of multiple nanoparticles based on a protein-induced reduction/decoration of graphene oxide. *J. Am. Chem. Soc.* **2010,** 132, 7279.

(19) Guo, S.; Wen, D.; Zhai, Y.; Dong, S.; Wang, E. Platinum nanoparticle ensemble-on-graphene hybrid nanosheet: one-pot, rapid synthesis, and used as new electrode material for electrochemical sensing. *ACS Nano* **2010,** 4, 3959.

(20) Liang, J.; Chen, Z.; Guo, L.; Li, L. Electrochemical sensing of l-histidine based on structure-switching DNAzymes and gold nanoparticle–graphene nanosheet composites. *Chem. Commun.* **2011,** 47, 5476.

(21) Shen, J.; Shi, M.; Li, N.; Yan, B.; Ma, H.; Hu, Y.; Ye, M. Facile synthesis and application of Ag-chemically converted graphene nanocomposite. *Nano Research* **2010,** 3, 339.

(22) Guo, H.-L.; Wang, X.-F.; Qian, Q.-Y.; Wang, F.-B.; Xia, X.-H. A green approach to the synthesis of graphene nanosheets. *ACS Nano* **2009,** 3, 2653.

(23) Yin, Z.; Li, H.; Li, H.; Jiang, L.; Shi, Y.; Sun, Y.; Lu, G.; Zhang, Q.; Chen, X.; Zhang, H. Single-layer MoS_2 phototransistors. *ACS Nano* **2011,** 6, 74.

(24) Radisavljevic, B.; Radenovic, A.; Brivio, J.; Giacometti, V.; Kis, A. Single-layer MoS_2 transistors. *Nat. Nanotechnol.* **2011,** 6, 147.

(25) Wang, L.; Omomo, Y.; Sakai, N.; Fukuda, K.; Nakai, I.; Ebina, Y.; Takada, K.; Watanabe, M.; Sasaki, T. Fabrication and characterization of multilayer ultrathin films of exfoliated MnO_2 nanosheets and polycations. *Chem. Mater.* **2003,** 15, 2873.

(26) Lin, Y.; Williams, T. V.; Connell, J. W. Soluble, exfoliated hexagonal boron nitride nanosheets. *J. Phys. Chem. Lett.* **2010,** 1, 277.

(27) Ebina, Y.; Sasaki, T.; Harada, M.; Watanabe, M. Restacked perovskite nanosheets and their Pt-loaded materials as photocatalysts. *Chem. Mater.* **2002,** 14, 4390.

(28) Ida, S.; Ogata, C.; Eguchi, M.; Youngblood, W. J.; Mallouk, T. E.; Matsumoto, Y. Photoluminescence of perovskite nanosheets prepared by exfoliation of layered oxides, $K_2Ln_2Ti_3O_{10}$, $KLnNb_2O_7$, and $RbLnTa_2O_7$ (Ln : lanthanide ion). *J. Am. Chem. Soc.* **2008,** 130, 7052.

(29) Zou, Y.; Wang, Y. NiO nanosheets grown on graphene nanosheets as superior anode materials for Li-ion batteries. *Nanoscale* **2011,** 3, 2615.

(30) Wang, Y.; Fan, X.; Sun, J. Hydrothermal synthesis of phosphate-mediated ZnO nanosheets. *Mater. Lett.* **2009,** 63, 350.

(31) Zhang, L.; Chen, D.; Jiao, X. Monoclinic structured $BiVO_4$ nanosheets: hydrothermal preparation, formation mechanism, and coloristic and photocatalytic properties. *J. Phys. Chem. B* **2006,** 110, 2668.

(32) Dai, Z. R.; Pan, Z. W.; Wang, Z. L. Gallium oxide nanoribbons and nanosheets. *J. Phys. Chem. B* **2002,** 106, 902.

(33) Liang, C.; Shimizu, Y.; Sasaki, T.; Umehara, H.; Koshizaki, N. Au-mediated growth of wurtzite ZnS nanobelts, nanosheets, and nanorods via thermal evaporation. *J. Phys. Chem. B* **2004,** 108, 9728.

(34) Hyde, G. K.; Scarel, G.; Spagnola, J. C.; Peng, Q.; Lee, K.; Gong, B.; Roberts, K. G.; Roth, K. M.; Hanson, C. A.; Devine, C. K.; Stewart, S. M.; Hojo, D.; Na, J. S.; Jur, J. S.; Parsons, G. N. Atomic layer deposition and abrupt wetting transitions on nonwoven polypropylene and woven cotton fabrics. *Langmuir* **2010,** 26, 2550.

(35) Jur, J. S.; Spagnola, J. C.; Lee, K.; Gong, B.; Peng, Q.; Parsons, G. N. Temperature-dependent subsurface growth during atomic layer deposition on polypropylene and cellulose fibers. *Langmuir* **2010,** 26, 8239.

(36) Wilson, C. A.; Grubbs, R. K.; George, S. M. Nucleation and growth during Al_2O_3 atomic layer deposition on polymers. *Chem. Mater.* **2005,** 17, 5625.

(37) Peng, Q.; Tseng, Y. C.; Darling, S. B.; Elam, J. W. Nanoscopic patterned materials with tunable dimensions via atomic layer deposition on block copolymers. *Adv. Mater.* **2010,** 22, 5129.

(38) Linder, V.; Gates, B. D.; Ryan, D.; Parviz, B. A.; Whitesides, G. M. Water-soluble sacrificial layers for surface micromachining. *Small* **2005,** 1, 730.

(39) Pan, Z. W.; Wang, Z. L. Nanobelts of semiconducting oxides. *Science* **2001,** 291, 1947.

(40) Hagrman, P. J.; Hagrman, D.; Zubieta, J. Organic–inorganic hybrid materials: From "simple" coordination polymers to organodiamine-templated molybdenum oxides. *Angew. Chem. Int. Ed.* **1999,** 38, 2638.

(41) Stroock, A. D.; Kane, R. S.; Weck, M.; Metallo, S. J.; Whitesides, G. M. Synthesis of free-standing quasi-two-dimensional polymers. *Langmuir* **2003,** 19, 2466.

(42) Vendamme, R.; Onoue, S.-Y.; Nakao, A.; Kunitake, T. Robust free-standing nanomembranes of organic/inorganic interpenetrating networks. *Nat. Mater.* **2006,** 5, 494.

(43) Kagan, C. R.; Mitzi, D. B.; Dimitrakopoulos, C. D. Organic-inorganic hybrid materials as semiconducting channels in thin-film field-effect transistors. *Science* **1999,** 286, 945.

(44) Sanchez, C.; Julian, B.; Belleville, P.; Popall, M. Applications of hybrid organic-inorganic nanocomposites. *J. Mater. Chem.* **2005,** 15, 3559.

Chapter 6

Field Effect Transistor by Nanosheets Fabricated using Atomic Layer Deposition

6.1 Introduction

Ultra-thin two dimensional (2D) nanosheets have showed unique mechanical, optical, or electrical properties such as high thermal conductivity or high stiffness.[1] Especially, unique electrical properties of nanosheets come from confinement of electrons in 2D plane. Field effect transistor (FET) is a transistor using electrical field to flow electron where output current is controlled by electrical field. When metal oxide semiconductor is applied in FET as a channel, it is called in metal oxide semiconductor FET (MOSFET). Since the performance of FET depends on the electrical properties of metal oxide film, transistor has been fabricated to demonstrate unique electrical properties of ultra-thin nanosheets. Figure 6.1 shows one kind of a transistor with lithium vanadate graphene (LiVO-graphene) nanosheet using bottom gate.[2] Zhu *et al*. demonstrated carrier type of graphene layer could be modified by the position of lithium atoms and conductivity of nanosheets could be controlled by external electric field. Also, Lee *et al*. fabricated a phototransistor with a few layers of MoS_2 nanosheet as transparent gate electrode.[3] Dogan *et al*. showed a few nanometer height of PbS nanosheets has photoconductivity.[4]

Here, we fabricated bottom gate transistor with TiO_2 nanosheet using atomic layer deposition (ALD) and measured the current between source and drain by sweeping gate and drain voltage. Unlike we expected, the results did not show the typical properties of n-type semiconductor and we attribute it to defects between nanosheet and SiO_2 substrate.

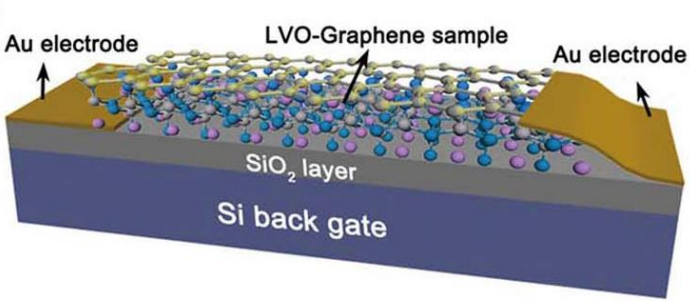

Figure 6.1 Schematic illustration of LiVO-graphene based transistor.[2]

6.2 Experimental Procedure

Boron doped p-type Si substrate with resistivity < 0.1 Ω·cm was used as gate electrode. SiO_2 gate dielectric layer (100 nm) was thermally formed on gate electrode and one corner of SiO_2/B-doped Si electrode was etched in HF solution (10 %) for 30 sec for gate contact. Titania nanosheets with thickness of ~5 nm were fabricated using ALD as the same method presented in chapter 4. After released in deionized (DI) water, TiO_2 nanosheets were placed on SiO_2 (100 nm)/B-doped Si electrodes followed by annealing at 450 °C for 1 h in air. As source and drain electrodes, Au (100 nm) and Cr (10 nm) were deposited on both side of TiO_2 nanosheet by thermal evaporation using a mask. The space between electrodes was 300 μm and height of electrodes was 1 mm. The general structure is similar with the transistor with bottom gate and top contact shown in Figure 6.1.

Semiconductor parameter analyzer (HP 4156A) was used for I-V characterization. The gate contact was established through the etched surface with a probe. By sweeping V_{SD} or V_G, the current between source and drain (I_{SD}) was monitored.

6.3 Results and Discussion

Figure 6.2(a) shows TiO_2 nanosheet collected on SiO_2/B-doped Si substrate and annealed at 450 °C for 1 h. Figure 6.2(b) is an optical microscopic image of the same nanosheet after source/drain electrodes deposition by thermal evaporation with the space of 300 μm. The overall picture of TiO_2 nanosheet transistor is shown in figure 6.2(c). One corner was etched before TiO_2 nanosheet collection for gate contact.

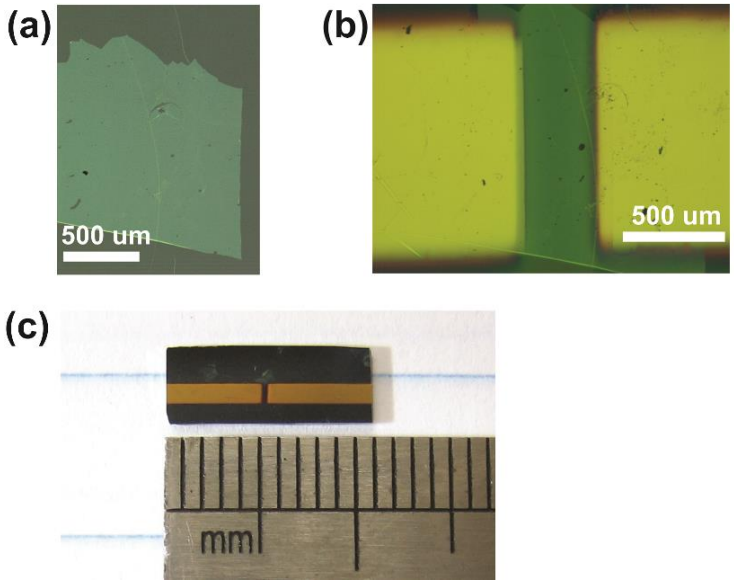

Figure 6.2 Optical microscopic images of (a) TiO_2 nanosheet place on SiO_2/B-doped Si wafer after annealed and (b) after Au/Cr thermal evaporation on both sides of nanosheets. (c) Picture showing TiO_2 nanosheet FET with a total size of ~1.1 cm.

Figure 6.3(a) is I_{DS}-V_{DS} graph under sweeping gate voltage (V_G) from -4 to 4 V. As n-type semiconductor,[5,6] I_{DS} should be increased with increased V_G with TiO_2 channel but

they present no dependence on gate voltage. In addition, I_{DS} is decreased as V_G is increased from -20 V to 20 V under V_{DS} = 1 V as shown in Figure 6.3(b). This is a behavior of p-type channel rather than that of n-type channel.[7]

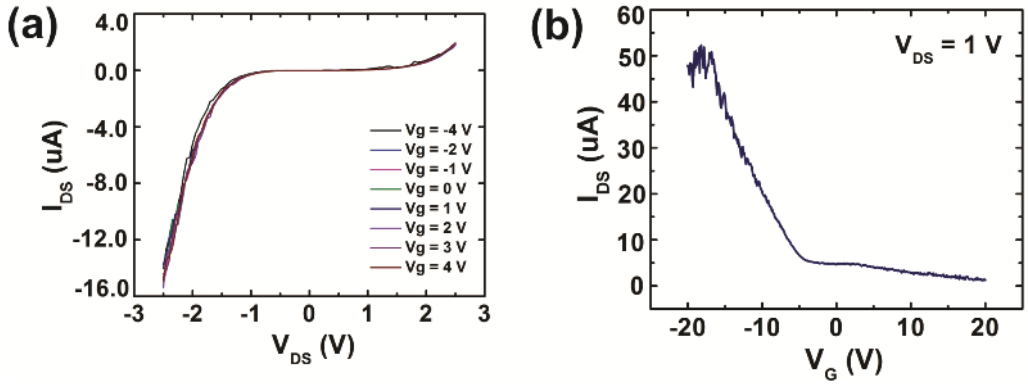

Figure 6.3 (a) I_{DS}-V_{DS} graph under various gate voltage (-4 – 4 V). (b) I_{DS}-V_G graph under V_{DS} = 1 V.

We believed that one main reason why the device did not show n-type field effect with TiO_2 channel is interface defects between a nanosheet and SiO_2/Si electrode brought about during nanosheet collection from the solvent. To overcome a drawback of interfacial defects, we annealed the device under vacuum or air. In addition, Ti/Au or Ti/Al was used as source/drain electrodes instead of Cr/Au. However, no improvement of the devices was observed with TiO_2 nanosheets. The increase in nanosheet thickness that can provide enough carriers or decrease in interfacial defects between electrodes and nanosheet would be expected to improve the characteristics of FET with TiO_2 nanosheets.

6.4 Summary

In conclusion, we have fabricated bottom gate MOFET with 5 nm thick-TiO_2 nanosheet to demonstrate electrical properties of nanosheet using ALD. Despite of n-type channel, it was found that the device did not show I-V characteristics from typical n-type field effect, which might be resulted from high density of defects that present between SiO_2/Si electrode and nanosheet. Also, 5 nm thickness of TiO_2 nanosheet would not be enough to provide carriers. We expect that the optimization of nanosheet thickness and decrease in interfacial defects can improve the TiO_2 nanosheet FET to show n-type field effect.

References

(1) Stankovich, S.; Dikin, D. A.; Dommett, G. H. B.; Kohlhaas, K. M.; Zimney, E. J.; Stach, E. A.; Piner, R. D.; Nguyen, S. T.; Ruoff, R. S. Graphene-based composite materials. *Nature* **2006,** 442, 282.

(2) Zhu, H.; Qin, X.; Sun, X.; Yan, W.; Yang, J.; Xie, Y. Rocking-chair configuration in ultrathin lithium vanadate-graphene hybrid nanosheets for electrical modulation. *Sci. Rep.* **2013,** 3.

(3) Lee, H. S.; Min, S. W.; Chang, Y. G.; Park, M. K.; Nam, T.; Kim, H.; Kim, J. H.; Ryu, S.; Im, S. MoS_2 nanosheet phototransistors with thickness-modulated optical energy gap. *Nano Lett.* **2012,** 12, 3695.

(4) Dogan, S.; Bielewicz, T.; Cai, Y. X.; Klinke, C. Field-effect transistors made of individual colloidal PbS nanosheets. *Appl. Phys. Lett.* **2012,** 101, 073102.

(5) Wobkenberg, P. H.; Ishwara, T.; Nelson, J.; Bradley, D. D. C.; Haque, S. A.; Anthopoulos, T. D. TiO_2 thin-film transistors fabricated by spray pyrolysis. *Appl. Phys. Lett.* **2010,** 96, 082116.

(6) Chua, L. L.; Zaumseil, J.; Chang, J. F.; Ou, E. C. W.; Ho, P. K. H.; Sirringhaus, H.; Friend, R. H. General observation of n-type field-effect behaviour in organic semiconductors. *Nature* **2005,** 434, 194.

(7) Liao, L.; Zhang, Z.; Yan, B.; Zheng, Z.; Bao, Q. L.; Wu, T.; Li, C. M.; Shen, Z. X.; Zhang, J. X.; Gong, H.; Li, J. C.; Yu, T. Multifunctional CuO nanowire devices: p-type field effect transistors and CO gas sensors. *Nanotechnology* **2009,** 20, 085203.

Chapter 7

Photoeletrochemical Properties of Electrodeposited Cu_2O Film

This chapter will be considered for publication.

7.1 Introduction

Cu_2O is p-type semiconductor with a direct bandgap of ~2.0 eV.[1] This narrow bandgap allows the film to absorb visible light as well as UV light, which is suitable for solar cells, water splitting, or photocatalysts.[2-5] When Cu_2O forms heterostructures with n-type semiconductor such as ZnO or TiO_2, the possibility of recombination of electron-hole pairs is decreased by facilitating separation and transfer of photoinduced charge enhancing the efficiency.[6-8] Cu_2O film has been deposited with various techniques such as thermal oxidation of copper,[9,10] sol-gel-like dip methods,[11] vacuum evaporation,[12] chemical vapor deposition[13], or hydrothermal synthesis.[14] Compared to other techniques, electrodeposition is very useful to easily and accurately control their morphology or thickness depending on applied potential, magnetic field, concentration, and pH of the deposition solution.[15-19] Proposed mechanism of Cu_2O electrodeposition is,[20]

$$2Cu^{2+} + 2e^{-} + H_2O \rightarrow Cu_2O + 2H^{+}$$

Although Cu_2O has great potential for use in solar cells and water splitting, the most challenge is its chemical and mechanical instability in the solution including water or at high temperature. Under those conditions, Cu_2O is oxidized to CuO or reduced to Cu.[21,22] Therefore, the maximum efficiency of Cu_2O solar cells to date is still 2%[4] even though the theoretical efficiency is 14% to 20%.[23] The reason for degradation in water splitting is that the redox potential of Cu_2O is placed between its bandgap ranges as shown in Figure 7.1.[24] Recently, Paracchino *et al*. showed that TiO_2 film as a protective layer with Al-doped ZnO (Al:ZnO) film as a buffer layer deposited by atomic layer deposition (ALD) efficiently

protected Cu_2O for photoelectrochemical (PEC) water splitting.[2] They also found that higher efficiency could be achieved with the optimal thickness of Al:ZnO and TiO_2 ALD layer after annealing at 200 °C in air.

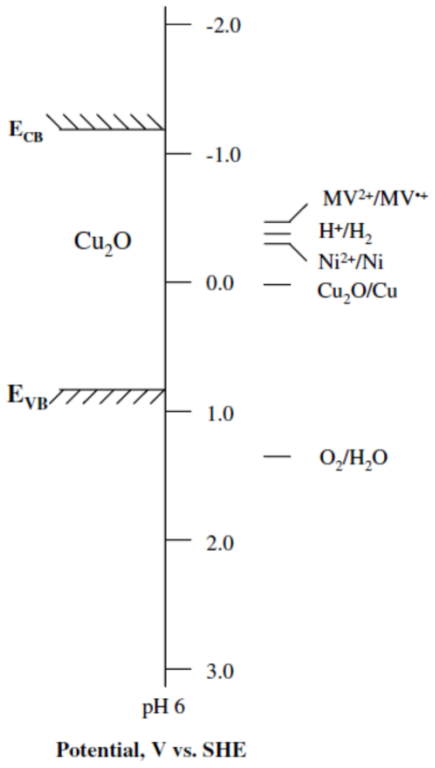

Figure 7.1 Conduction and valence band edges for Cu_2O and TiO_2 (vs. SHE) in comparison with redox potentials of relevant species.[24] A solution pH of 6 was assumed.

We present here that morphology and thickness of electrodeposited Cu_2O are varied with pH of the solution, deposition temperature, and deposition time. Moreover, we investigated the electrochemical behavior of Cu_2O film with different thickness. As buffer layer and protective layer, Al:ZnO and TiO_2 ALD films were deposited on the Cu_2O film as

Paracchino *et al*. demonstrated.[2] The results, however, showed no improvement in photochemical stability with ALD films in the same thickness.

7.2 Experimental procedure

The deposition solution is 0.3 M $CuSO_4$ and 3 M lactic acid in DI water. The solutions are adjusted to pH 9 – pH 13 with 0.1M KOH aqueous solution. All chemicals were purchased from Sigma-Aldrich and used without further purification. Cu_2O films were grown using Wavenow50 (Pine Instrument) potentiostat with copper wire as a counter electrode and an Ag/AgCl reference electrode (Broadley-James). The films were electrodeposited at -0.45 V vs Ag/AgCl reference electrode (-0.253 V vs NHE) at temperature range between 30 °C and 70 °C. The substrate for electrodeposition was fluorine-doped tin oxide (FTO) glass substrates (TEC 8, Pilkington) after cleaning with ethanol and deionized (DI) water followed by drying out residual solvents with nitrogen stream. Platinum nanoparticles were electrodepsosited in dark on Cu_2O on FTO glass using 1 mM H_2PtCl_6 and 0.5 M Na_2SO_4 aqueous solution with Pt mesh as a counter electrode. During deposition, current density was fixed at 200 $\mu A/cm^2$ for 10 s.

Cu_2O film thickness was measured with surface profilometry (Dektak D150, Veeco) and surface morphology was investigated with scanning electron microscopy (PHENOM™, FEI). Crystallinity of Cu_2O was determined using the Rigaku SmartLab X-ray diffractometer with Cu Ka radiation as an X-ray source (40 kV, 44 mA).

ALD was performed in a custom hot wall viscous flow tube. The precursors for ZnO, Al_2O_3, TiO_2 films are diethylzinc (DEZ, 95%), trimethylaluminum (TMA, 98%), and ($TiCl_4$, 99%) respectively, with deionized (DI) water as co-reactant. All precursors were purchased from Strem Chemicals, Inc. Nitrogen was used as the carrier and purge gas and purified before use with an inert gas filter (Gatekeeper®, Entegris Inc.). ALD sequence for TiO_2 films was [$TiCl_4/N_2/H_2O/N_2$] = [1/40/1/40 s] at 100 °C. Al-doped ZnO film (Al:ZnO) was grown with the sequences of [$TMA/N_2/H_2O/N_2$] = [1/30/1/30 s] and [$DEZ/N_2/H_2O/N_2$] = [2/50/2/50 s], respectively at process temperature of 60 °C. One cycle for Al:ZnO film was consisted of 25 cycles of ZnO followed by 1 cycle of Al_2O_3. Operating pressure was 2 Torr and partial pressure of DEZ, TMA, and DI water was 0.1 – 0.2 Torr. The partial pressure of $TiCl_4$ was 0.02 Torr.

For photoelectrochemical measurement, electrical connection was made to the sample by contacting FTO glass with a copper wire (0.064 in in diameter) with silver paste (Pelco, conductive silver 187). Glass tube was put through the Cu wire, so that the surface-normal of the substrate was perpendicular to the glass tube. Non-conductive epoxy (Hysol 9462, Loctitte) was used for sealing at the end of the glass tube as well as around the sides of the FTO glass to prevent the FTO layer being exposed to the electrolyte. After that, they were cured under a heating gun at ~80 °C in ambient environment. The active area of the photoelectrode was measured with ImageJ software from the photo images of the electrodes. All electrochemical measurements under light were performed in a custom fabricated glass cell with quartz window on one side using a three-electrode configuration under front illumination AM 1.5. A potentiostat (VersaSTAT 3, Princeton Applied Research) was used

for cyclic voltammetry (CV) measurement where the potential was swept from -0.2 to 0.9 V vs Ag/AgCl reference electrode (Broadley-James) at a scan rate of 10 mV/s under dark and then under light. Also, the stability of photocurrent was measured under chopped light illumination (light for 40 s and dark for 20 s). Platinum mesh was served as the counter electrode. All electrodes were tested in 1 M Na_2SO_4 at pH 4.9, which was continuously bubbled with ultrahigh purity Ar to remove oxygen and H_2 from the solution.

7.3 Results and Discussion

Figure 7.2 shows electrodeposited Cu_2O films on FTO glass for 10 min with various deposition temperature and pH of the solutions. When the solutions have pH range from 9 to 11, Cu_2O films show bright yellow color. The color is gradually changed to red as the temperature is increased. The Cu_2O films from the pH 9 solution have reddish yellow color from 60 °C while the similar color appeared from 40 °C in the films electrodeposited from pH 10 or pH 11 solution. The film from the pH 12 solution shows red color from 30 °C but the uniform film is shown from 50 °C. The pH 13 solution is not suitable for 10 min deposition at this temperature range to get uniform Cu_2O film. At 30 and 40 °C, no film deposition was observed, and Cu_2O was deposited partially and non-uniformly even at higher temperature. The Cu_2O films obtained from pH 11 solution at 60 and 70 °C shows cloudy surface, which is resulted from high scattering from larger crystal sizes.[25] When compared to the films deposited from higher pH solution (pH 12 – pH 13), lower pH solutions produce more uniform films.

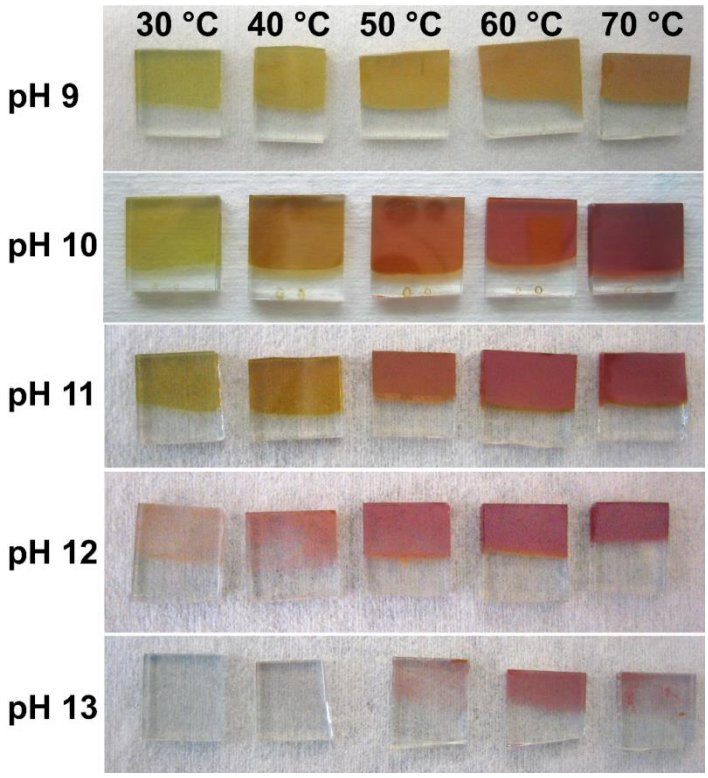

Figure 7.2 Pictures of electrodeposited Cu_2O film on FTO glass with varying solution pH and deposition temperature for 10 min.

Figure 7.3(a) shows dependence of Cu_2O film thickness on the deposition temperature from pH 9 to pH 12. In general, thickness of Cu_2O film is increased with increasing pH but the films deposited from pH 10 and pH 11 solutions show similar thickness for all temperature range. At pH 9, the film thickness is very slowly increased depending on the deposition temperature while the films from higher pH show stronger temperature dependency. In particular, thickness increases faster after 50 °C than below 50 °C for pH 10 – pH 12. Figure 7.3(b) is XRD spectra of the film electrodeposited at 40 °C from the solution with pH 10 for 1 h confirming Cu_2O.

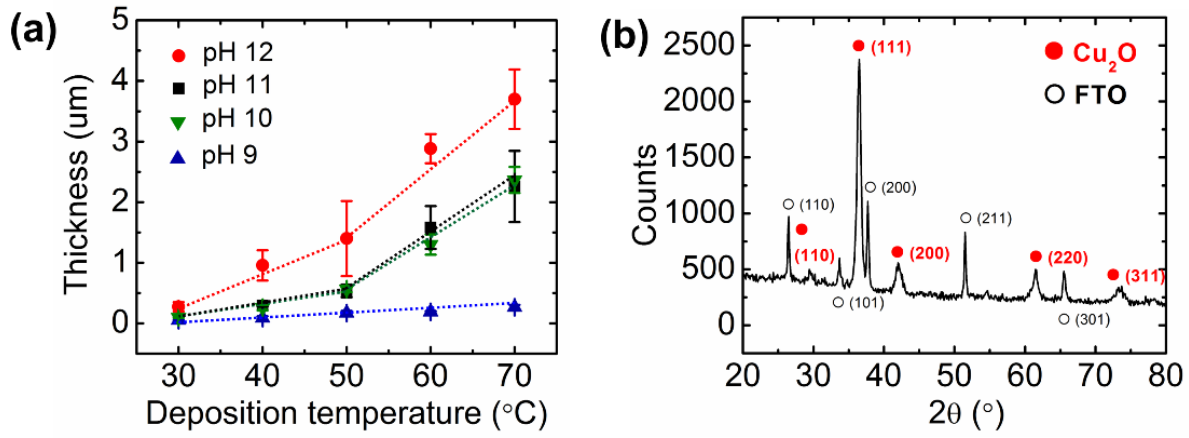

Figure 7.3 (a) Graph of Cu_2O film thickness electrodeposited for 10 min depending on deposition temperature with varying pH of the solution. As temperature or pH of the solution is increased, film is thicker. (b) XRD spectrum of Cu_2O film on FTO glass grown with the solution of pH 10 at 40 °C for 1 h. The peaks from Cu_2O film and FTO glass are marked with red circles and open black circles, respectively.

Figure 7.4 shows SEM images of Cu_2O films on FTO glass deposited at constant temperature, 40 °C with different pH and deposition time. All grains have triangular pyramidal shapes densely packed. The size of a grain is larger with longer deposition time. At pH 11, the film for 1 h deposition shows grains with ~2 um size (Figure 7.4b) which is much larger than that for 10 min deposition, less than 1 um (Figure 7.4a). Similarly, Cu_2O film deposited for 1 h from pH 12 solution has larger grain size with up to 10 μm but 10 min deposition produces ~2 μm gains (Figure 7.4c and d). When compare Figure 7.4(a) and 7.4(c), the solution with high pH grows larger grains than the solution with low pH for 10 min deposition. Also, Cu_2O film deposited for 1h shows an increase in grain size when pH of

the solution is increased from pH 11 to pH 12. The Cu_2O grain size from the solution with pH 11 for 1 h deposition is similar that from the solution with pH 12 for 10 min deposition.

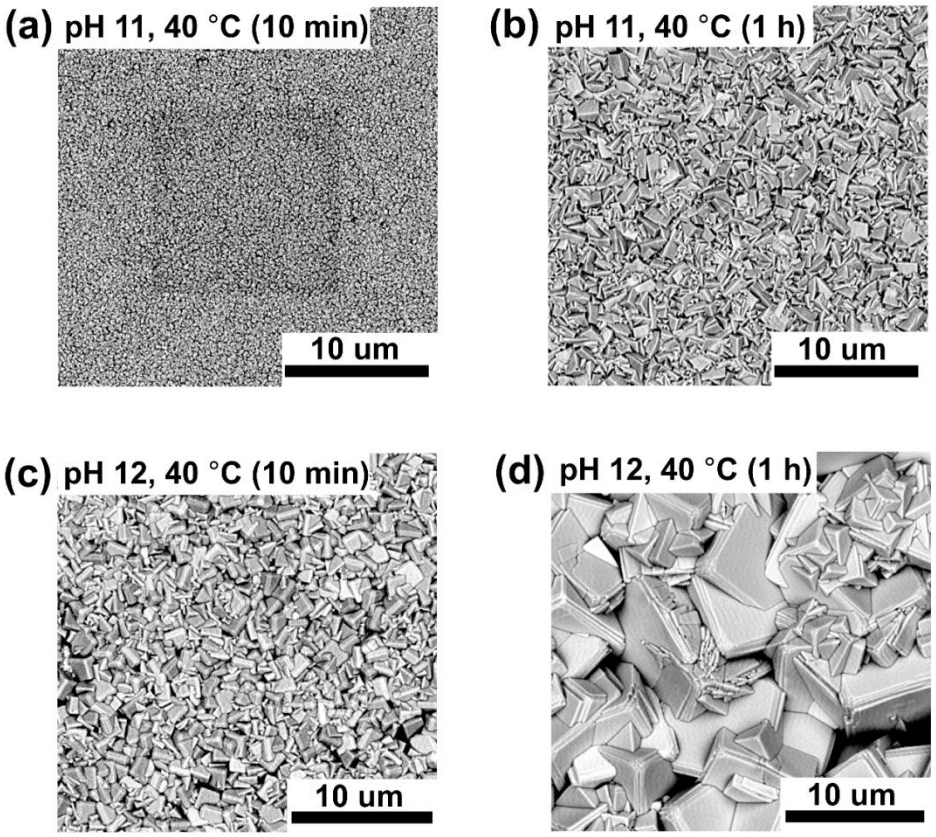

Figure 7.4 SEM images of electrodeposited Cu_2O film on FTO glass with the solution (pH 11) at 40 °C (a) for 10 min and (b) for 1 h. The Cu_2O grains grow larger (~2 um) for l h electrodeposition. (c) and (d) are Cu_2O films with the solution (pH 12) at 40 °C for 10 min and for 1 h, respectively. The grain size for 1 h electrodeposition is ~5 um which is bigger than that for 10 min electrodeposition (~2 um). Also, high pH solution produces bigger Cu_2O grains.

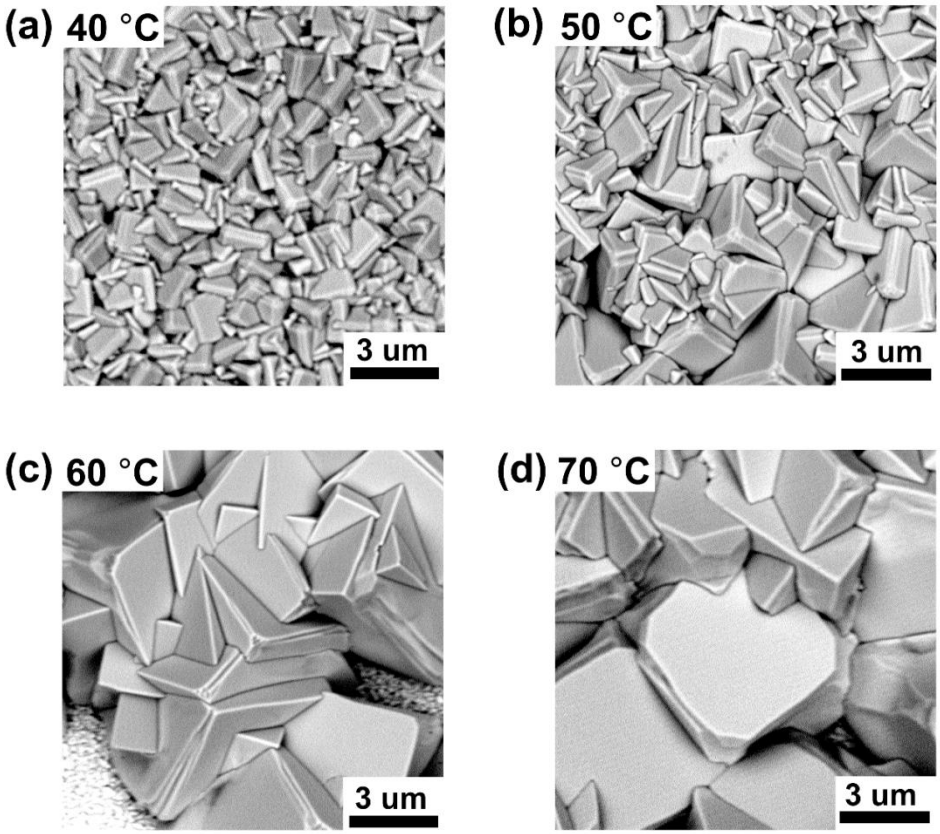

Figure 7.5 SEM images of electrodeposited Cu_2O film on FTO glass with the solution (pH 12) for 10 min at (a) 40 °C, (b) 50 °C, (c) 60 °C, and (d) 70 °C. The grain size is increased as the deposition temperature is increased.

To confirm the effect of the deposition temperature clearly, Cu_2O films were deposited from the solution with pH 12 for 10 min with different temperature. Figure 7.5 is SEM images of Cu_2O film deposited at the deposition temperature from 40 °C to 70 °C. They clearly show temperature dependency of morphology, that is, the grain size becomes larger as the deposition temperature is increased. At 40 °C, grain size is 1 μm – 1.5 μm and it is increased to ~4 μm at 70 °C, but there is no change observed in the shape of grains. They all

show pyramidal triangular shapes and two or more particles aggregate. The deposition temperature and the pH of the solution dependency is also observed by Bijani *et al.*[26] He explored modification of Cu_2O morphology on titanium substrate by bath pH, bath temperature, and applied potential. There is an increase in grain size of Cu_2O when bath pH is increased from 9 to 12 which are similar with our results. Also, they obtained large grain size when bath temperature goes up from 30 °C to 60 °C at -300 mV without morphological change but at the potential -600 mV, there are grain size increases as well as obvious morphological change.

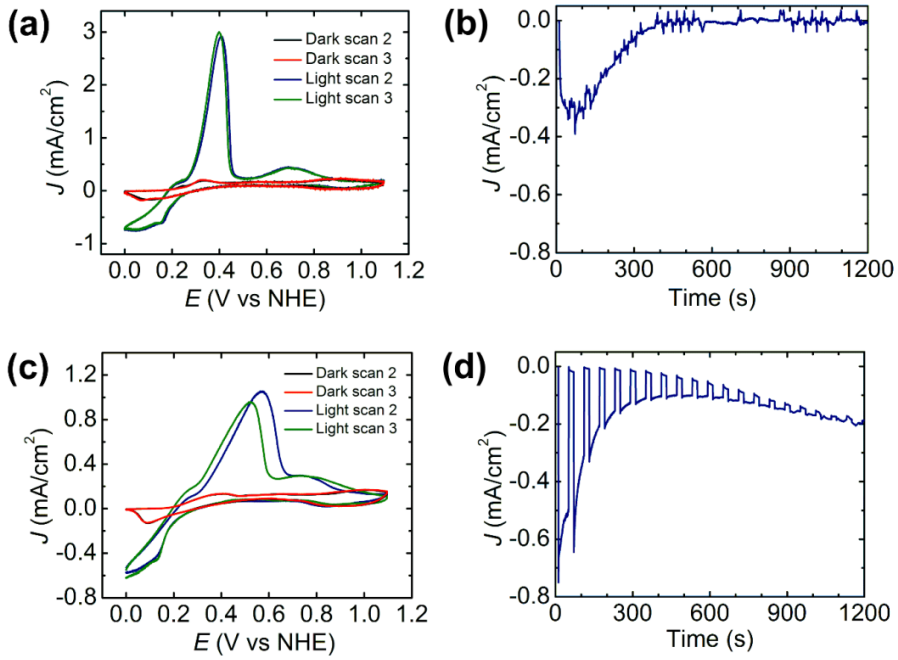

Figure 7.6 (a) CV measurement and (b) chopped illumination measurement (0 V vs NHE) for electrodeposited Cu_2O film for 10 min at 40 °C (pH 11). (c) CV measurement and (d) chopped measurement (0 V vs NHE) for electrodeposited Cu_2O film for 1 h at 40 °C (pH 11).

Figure 7.6 is cyclic voltammetry (CV) and photoelectrochemical response of 10 min-electrodeposited Cu_2O film (pH 11, 40 °C). As a bare film, it exhibits photooxidation at 0.4 V and 0.7 V under light. (Figure 7.6a) Photoreduction of water is shown with -0.75 mA/cm^2 vertical offset. (Figure 7.6b) Under chopped light, the photoelectrode shows photocurrent of -0.3 mA/cm^2 at initial illumination but no clear response to chopped light. Also, the reduction decomposes Cu_2O to Cu gradually within ~7 min during photoelectrochemical response, which is confirmed by color change of the surface to black. On the other hand, 1 h-electrodeposited film shows photooxidation at 0.5 V and 0.75 V which are shifted to positive potential when compared to 10 min-electrodeposited film (Figure 7.6c and d). But the current density of the highest peak (0.5 V) is much lower than that (0.4 V) in Figure 7.5(a). Photoreduction of water is observed with -0.6 mA/cm^2 vertical offset. Regarding photocurrent stability, 1 h electrodeposited film also shows reduction of Cu_2O to Cu for 20 min although it clearly responses to chopped light.

To protect Cu_2O film from photooxidation and photoreduction, TiO_2 ALD layer and Al:ZnO buffer layer were deposited on 10 min-electrodeposited Cu_2O film. Total ALD layer is composed of 11 nm TiO_2 (210 cycles at 100 °C) and 21 nm Al:ZnO film (60 °C) with the ratio of $ZnO:Al_2O_3$ as 4.2 nm:0.12 nm, which follow the best results from the literature.[2] Figure 7.7(a) shows the CV result of the Cu_2O photoelectrode with ALD layers. Similar to the bare Cu_2O, there are two photooxidation peaks at 0.38 V and 0.75 V but the intensities of the peaks are much lower than those of bare Cu_2O films. Also, the photoreduction of water shows a vertical offset of 0.1 mA/cm^2. The initial photocurrent under chopped illumination is -0.06 mA/cm^2 but it decays quickly with time (Figure 7.7b). Figure 7.7(c) and (d) show the

effect of post annealing of ALD layers at 200 °C for 45 min in air. The photooxidation peaks appear at the same potential with before annealing. However, Cu_2O photoelectrode with ALD after annealing retains initial photocurrent value for 20 min although it is decreased to -0.02 mA/cm^2.

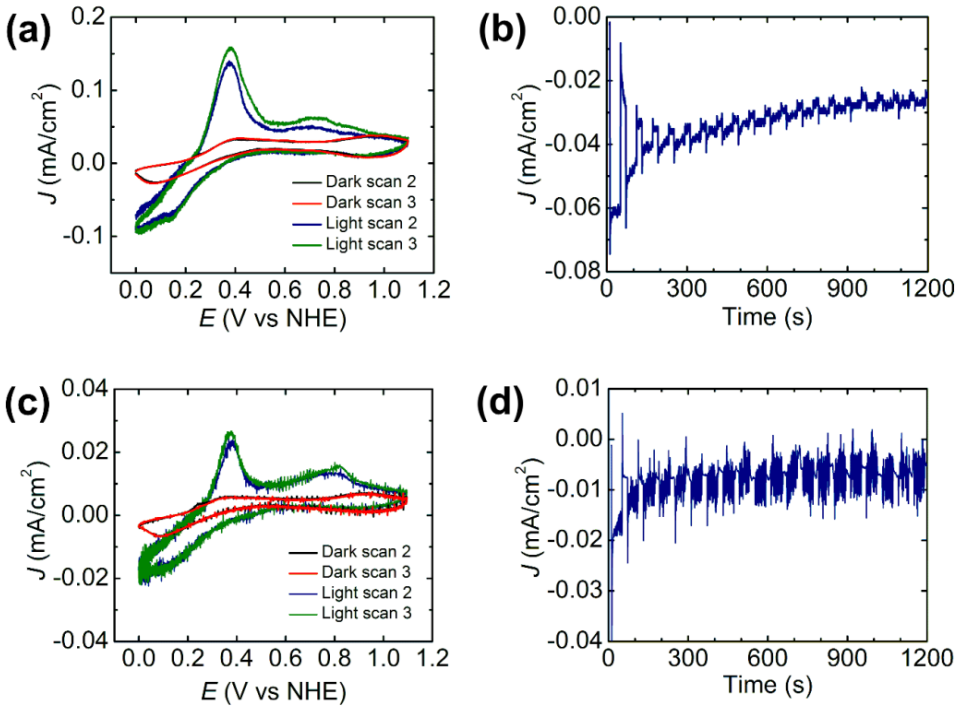

Figure 7.7 (a) CV measurement and (b) chopped measurement for electrodeposited Cu_2O film for 10 min at 40 °C (pH 11) with ALD film. (c) CV measurement and (d) chopped measurement for electrodeposited Cu_2O film for 10 min at 40 °C (pH 11) with ALD film followed by annealing at 200 °C for 45 min in air. Here, ALD film is composed of total 5 cycles of Al:ZnO (ZnO 25 cycles and Al_2O_3 1 cycle) and 210 cycles of TiO_2.

7.4 Summary

In summary, we showed that thickness of Cu_2O film depends on pH of the solution and deposition temperature, and deposition time. High pH and temperature as well as longer deposition time make Cu_2O film thicker. Also, the grain size of Cu_2O showed the same trend of dependency on them. The Cu_2O film deposited 1 h shows obvious photoresponse to the chopped light while the film from 10 min electrodeposition does not respond to that. Both films quickly degrade in 7-20 min. As protective and buffer layers, TiO_2 and Al:ZnO ALD films was expected to prevent photooxidation under light during CV measurement and stably respond to the chopped light. However, Cu_2O photoelectrodes with ALD layers still shows photooxidation peaks regardless of post annealing.

References

(1) Ghijsen, J.; Tjeng, L. H.; Vanelp, J.; Eskes, H.; Westerink, J.; Sawatzky, G. A.; Czyzyk, M. T. Electronic-structure of Cu_2O and CuO. *Phys. Rev. B* **1988,** 38, 11322.

(2) Paracchino, A.; Laporte, V.; Sivula, K.; Grätzel, M.; Thimsen, E. Highly active oxide photocathode for photoelectrochemical water reduction. *Nat. Mater.* **2011,** 10, 456.

(3) Kondo, J. Cu_2O as a photocatalyst for overall water splitting under visible light irradiation. *Chem. Commun.* **1998**, 357.

(4) Mittiga, A.; Salza, E.; Sarto, F.; Tucci, M.; Vasanthi, R. Heterojunction solar cell with 2% efficiency based on a Cu_2O substrate. *Appl. Phys. Lett.* **2006,** 88, 163502.

(5) Mahalingam, T.; Chitra, J.; Chu, J. P.; Moon, H.; Kwon, H. J.; Kim, Y. D. Photoelectrochemical solar cell studies on electroplated cuprous oxide thin films. *J. Mater. Sci.: Mater. Electron.* **2006,** 17, 519.

(6) Jiang, T.; Xie, T.; Zhang, Y.; Chen, L.; Peng, L.; Li, H.; Wang, D. Photoinduced charge transfer in ZnO/Cu_2O heterostructure films studied by surface photovoltage technique. *Phys. Chem. Chem. Phys.* **2010,** 12, 15476.

(7) Hou, Y.; Li, X.; Zou, X.; Quan, X.; Chen, G. Photoeletrocatalytic activity of a Cu_2O-loaded self-organized highly oriented TiO2 nanotube array electrode for 4-chlorophenol degradation. *Environ. Sci. Technol.* **2008,** 43, 858.

(8) Liu, L.; Gu, X.; Sun, C.; Li, H.; Deng, Y.; Gao, F.; Dong, L. In situ loading of ultra-small Cu_2O particles on TiO_2 nanosheets to enhance the visible-light photoactivity. *Nanoscale* **2012,** 4, 6351.

(9) Mani, S.; Jang, J. I.; Ketterson, J. B.; Park, H. Y. High-quality Cu_2O crystals with various morphologies grown by thermal oxidation. *J. Cryst. Growth* **2009,** 311, 3549.

(10) Musa, A.; Akomolafe, T.; Carter, M. Production of cuprous oxide, a solar cell material, by thermal oxidation and a study of its physical and electrical properties. *Sol. Energy Mater. Sol. Cells* **1998,** 51, 305.

(11) Ray, S. C. Preparation of copper oxide thin film by the sol–gel-like dip technique and study of their structural and optical properties. *Sol. Energy Mater. Sol. Cells* **2001,** 68, 307.

(12) Yanagimoto, H.; Akamatsu, K.; Gotoh, K.; Deki, S. Synthesis and characterization of Cu_2O nanoparticles dispersed in NH_2-terminated poly (ethylene oxide). *J. Mater. Chem.* **2001,** 11, 2387.

(13) Markworth, P.; Liu, X.; Dai, J.; Fan, W.; Marks, T.; Chang, R. Coherent island formation of Cu_2O films grown by chemical vapor deposition on MgO (110). *J. Mater. Res.* **2001,** 16, 2408.

(14) Yu, H.; Yu, J.; Liu, S.; Mann, S. Template-free hydrothermal synthesis of CuO/Cu_2O composite hollow microspheres. *Chem. Mater.* **2007,** 19, 4327.

(15) Kuo, C.-H.; Huang, M. H. Morphologically controlled synthesis of Cu_2O nanocrystals and their properties. *Nano Today* **2010,** 5, 106.

(16) Li, H.; Liu, R.; Zhao, R.; Zheng, Y.; Chen, W.; Xu, Z. Morphology control of electrodeposited Cu_2O crystals in aqueous solutions using room temperature hydrophilic ionic liquids. *Cryst. Growth Des.* **2006,** 6, 2795.

(17) Daltin, A.-L.; Addad, A.; Baudart, P.; Chopart, J.-P. Morphology of magneto-electrodeposited Cu_2O microcrystals. *CrystEngComm* **2011,** 13, 3373.

(18) Liu, R.; Oba, F.; Bohannan, E. W.; Ernst, F.; Switzer, J. A. Shape control in epitaxial electrodeposition: Cu_2O nanocubes on InP (001). *Chem. Mater.* **2003,** 15, 4882.

(19) Mahalingam, T.; Chitra, J.; Rajendran, S.; Sebastian, P. Potentiostatic deposition and characterization of Cu_2O thin films. *Semicond. Sci. Technol.* **2002,** 17, 565.

(20) De Jongh, P.; Vanmaekelbergh, D.; Kelly, J. J. d. Photoelectrochemistry of Electrodeposited Cu2 O. *J. Electrochem. Soc.* **2000,** 147, 486.

(21) Celino, M.; Cleri, F.; D'Agostino, G.; Rosato, V. Mechanical instability of oxidized metal clusters. *Phys. Rev. Lett.* **1996,** 77, 2495.

(22) Wu, L.; Tsui, L.-k.; Swami, N.; Zangari, G. Photoelectrochemical stability of electrodeposited Cu_2O films. *J. Phys. Chem. C* **2010,** 114, 11551.

(23) Olsen, L.; Addis, F.; Miller, W. Experimental and theoretical studies of Cu_2O solar cells. *Solar cells* **1982,** 7, 247.

(24) Somasundaram, S.; Raman Nair Chenthamarakshan, C.; de Tacconi, N. R.; Rajeshwar, K. Photocatalytic production of hydrogen from electrodeposited film and sacrificial electron donors. *Int. J. Hydrogen Energy* **2007,** 32, 4661.

(25) Kuo, C. H.; Chen, C. H.; Huang, M. H. Seed-mediated synthesis of monodispersed Cu_2O nanocubes with five different size ranges from 40 to 420 nm. *Adv. Funct. Mater.* **2007,** 17, 3773.

(26) Bijani, S.; Martínez, L.; Gabás, M.; Dalchiele, E.; Ramos-Barrado, J.-R. Low-temperature electrodeposition of Cu_2O thin films: modulation of micro-nanostructure by

modifying the applied potential and electrolytic bath pH. *J. Phys. Chem. C* **2009,** 113, 19482.

Chapter 8

The Effect of ZnO ALD film on Free-standing Cu_2O Sheets by Electrodeposition on Dye Photodegradation

This chapter contains preliminary results that can be expanded for publication.

8.1 Introduction

Copper (I) oxide (Cu_2O) has attracted considerable attention with great potentials in solar cells, water splitting, or photocatalysts.[1-3] It is p-type semiconductor with a direct band of ~2.0 eV, which allows Cu_2O to absorb visible light as well as UV light.[4] Cu_2O film composes p-n junction with n-type semiconductor such as TiO_2 or ZnO to enhance efficiency since they increase electron-hole separation as well as absorbing more photons from the light source.[5-8] In addition to n-type semiconductor, Cu_2O recently hybridizes with reduced graphene oxide (rGO) for hydrogen generation where rGO acts as electron acceptor like p-type semiconductor[4] or with carbon nanotubes for Li-ion batteries.[9] These heterojuction structures of Cu_2O with other materials enhance the efficiency. For example, phenol is degraded ~12 times faster with Cu_2O nanoparticles on TiO_2 nanosheets than with only TiO_2 nanosheets.[5] Similarly, Cu_2O/ZnO compounds degrade ~70% of methyl orange dye in 3 h while ~30% of dye is decomposed with ZnO. Also, no hydrogen production is observed only with TiO_2 but Cu_2O/TiO_2 catalysts produce 290 μmol/h hydrogen from water.[7] In addition, hydrogen production is increased by more than 13 times with Cu_2O/TiO_2 catalysts compared to TiO_2 catalysts.

Cu_2O can be grown with various techniques such as chemical deposition,[10,11] sputtering,[12,13] electrodeposition,[14,15] and hydrothermal synthesis.[16,17] Among these techniques, electrodeposition is effective and inexpensive way for Cu_2O growth in controllable morphology, crystal size, and film thickness depending on pH of the deposition solution,[15,18] addition of ionic liquid,[19] or concentration of the surfactant.[20] In particular, there

are growing interests on morphology control since Cu_2O has high dependence of reactivity on the morphology. For example, Ho *et al*. demonstrated that various Cu_2O structures have effects on photocatalytic activity depending on dye solutions.[21] The {1 1 1} faces have active photocatalytic effect for negatively charged molecules but not for positively charged modules while the {1 0 0} faces are neutral with no interaction for charged molecules. This different activity of facets also results in selective Au deposition.[22] Xu *et al*. showed that octahedral Cu_2O particles with exposed {1 1 1} faces have much higher photocatalytic activity than cubic Cu_2O particles.[23]

We present here free standing Cu_2O sheets grown by electrodeposition and their photocatalytic activity with methyl orange (MO) solution under UV and visible light. The effect of ZnO ALD layer on Cu_2O film is also investigated.

8.2 Experimental procedure

The deposition solution was prepared by 0.3 M $CuSO_4$ and 3 M lactic acid in DI water. The solution was adjusted to pH 12 with 0.1 M KOH aqueous solution. All chemicals were purchased from Sigma-Aldrich and used without further purification. Cu_2O films were grown using Wavenow50 (Pine Instrument) potentiostat with copper wire as a counter electrode and an Ag/AgCl reference electrode (Broadley-James). The substrate was indium oxide coated polyethylene terephthalate (PET) film (surface resistivity $\leq$ 10 Ω/sq, Sigma-Aldrich). The films were electrodeposited at constant potential, -0.45 V vs SCE or at constant current density, -0.4 mA/cm^2 at 40 °C for 1 h. After deposition, the films were washed with

fresh DI water and blown with N_2. Cu_2O film thickness was measured with surface profilometry (Dektak D150, Veeco) and surface morphology was investigated with scanning electron microscopy (PHENOM™, FEI).

ALD on eletrodeposited Cu_2O film was performed in a custom hot wall viscous flow tube. Precursor was diethylzinc (DEZ, 95%, Strem Chemicals, Inc) with deionized (DI) water as co-reactant. Nitrogen was used as a carrier and purge gas and purified before use with an inert gas filter (Gatekeeper®, Entegris Inc.). ALD sequence is consisted of [$DEZ/N_2/H_2O/N_2$] = [2/50/2/50 s] at process temperature of 60 °C. Operating pressure was 2 Torr and partial pressure of DEZ and DI water was 0.1 – 0.2 Torr. Under this condition, ZnO growth rate was 1.7 Å/cy.

To investigate photocatalytic effect, Cu_2O or Cu_2O/ZnO sheets were separated from indium oxide coated PET film by bending with hand and then collected in Pyrex vial. The surface area of sheets was fixed at 160 cm^2 if not indicated. Methyl orange (MO) solution of 10 ppm was used as organic dye. Before measurement, MO solution with Cu_2O sheets were stirred under dark for 30 min. Absorbance of methyl orange solution was measured using UV-vis spectrophotometer (Evolution 300, Thermo Scientific Inc.) at 466 nm every 10 or 30 min after UV irradiation with UV flood system (Intelli-Ray 400, Uvitron International). Visible light was irradiated from solar simulator (M-9119, Newport) equipped with a 300 W xenon lamp where light intensity was adjusted to AM 1.5 G with a calibrated Si standard solar cell (91150V, Newport).

8.3 Results and Discussion

Figure 8.1(a) shows bare ITO-PET film. After electrodeposition for 1 h, uniform Cu_2O film was formed on the ITO-PET film (Figure 8.1b). The film thickness measured by profilometry was ~1 μm. Simple bending with hands isolates Cu_2O film from the substrate as shown in Figure 8.1(c) into sheets and they were easily rolled up because of bending (inset image). After separation, ITO-PET substrates are still conductive, which means only Cu_2O films were detached from the substrate. The sheets have various size and shape since they are separated randomly without control on shape or size. Figure 8.1(d) shows one Cu_2O sheet that have ~5 mm in lateral size.

Cu_2O sheets can be directly collected in the vial for photocatalysis experiment. The photocatalytic effect of Cu_2O sheets is examined with MO aqueous solution (10 ppm). Separated Cu_2O sheets with total surface area of 160 cm^2 are collected in Pyrex vial with MO aqueous solution. Figure 8.2(a) shows dye degradation with Cu_2O sheets depending on irradiation time under UV-light. The absorbance is measured at 466 nm which is prominent peak of MO dye and decrease in the peak intensity means MO decomposition or oxidation. The concentration of the solution is decreased for 30 min but after that, it is increased again up to 120 min. Once it reaches at the initial value at 120 min, the concentration does not change from the initial value at 150 min. On the other hand, when ZnO ALD film (17 nm from 100 cycles) is deposited on Cu_2O film at 60 °C before isolation, the dye keeps degrading for 150 min as shown in Figure 8.2(b). Even though the mechanism about MO recovery is not clear now, ZnO as an n-type semiconductor protects Cu_2O from reducing. To

investigate that increase in absorbance at 466 nm is resulted from any chemical bond change, UV-vis spectrum between 250−650 nm was obtained. Figure 8.2(c) and (d) show that there are only absorbance decrease for 30 min and increase between 30 and 150 min (30, 40, 50, 70, 80, 90, 100, and 150 min) without peak shift. Therefore, MO molecules are oxidized by Cu_2O, but after some time, it is recovered to the initial concentration. Further analysis like mass spectrometry is needed to find out what happens in MO solution during UV irradiation.

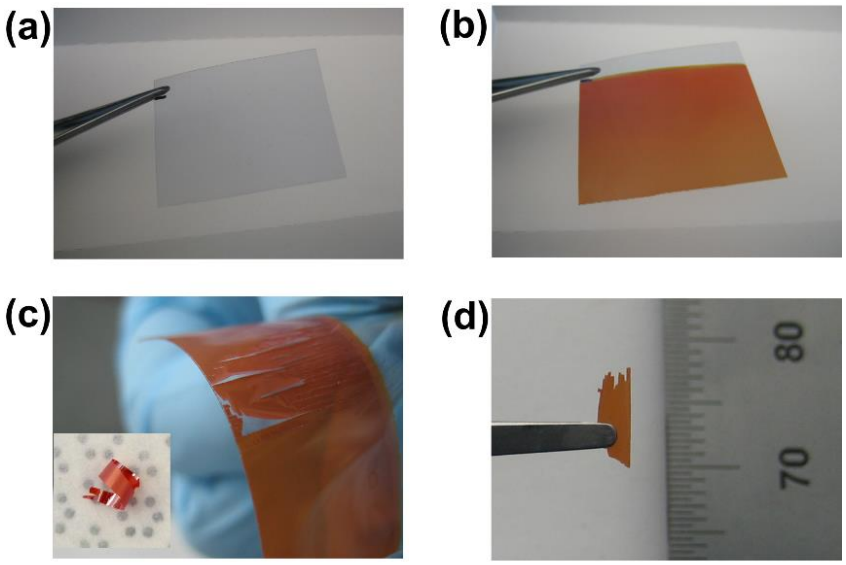

Figure 8.1 Pictures of ITO-PET film (a) before electrodeposition and (b) after electrodeposition for 40 °C 1 h. (c) Cu_2O film is easily separated from the substrate by bending. Inset shows the rolled-up Cu_2O sheet. (d) Picture of the isolated Cu_2O sheet that has a length of ~5 mm.

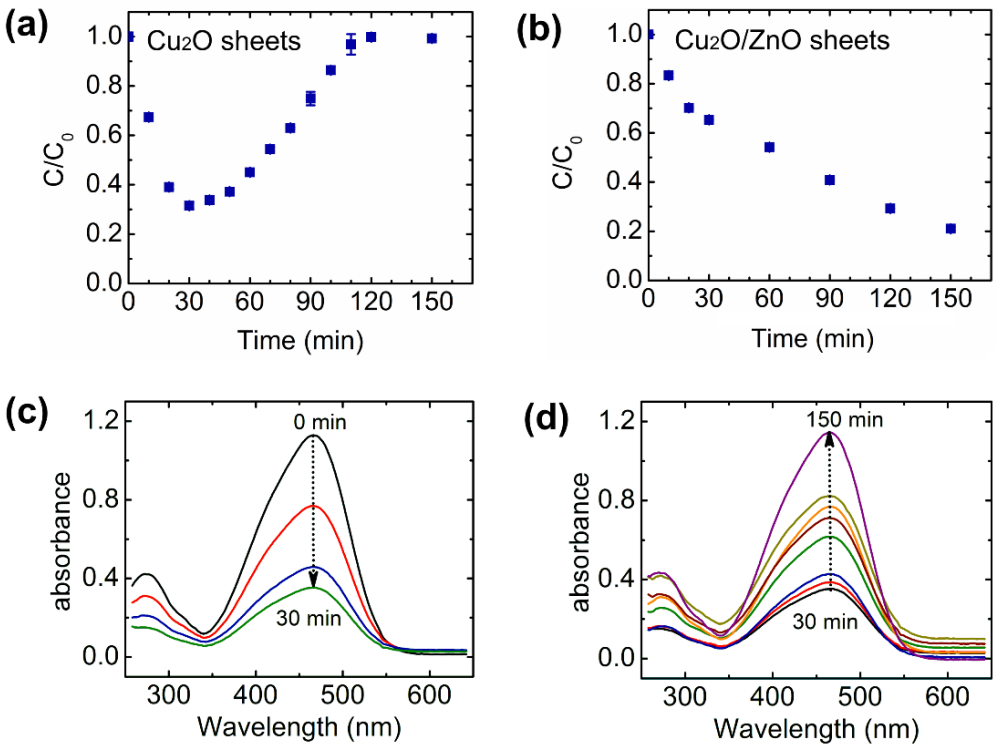

Figure 8.2 Photodegradation of methyl orange under UV-irradiation with (a) Cu_2O sheets and (b) Cu_2O sheets with ZnO ALD film (~17 nm) depending on UV irradiation time. (c) Absorbance spectrum of MO solution with Cu_2O sheets every 10 min for 30 min. The dotted arrow indicates decrease in absorbance at 466 nm. (d) Absorbance spectrum (250–650 nm) of MO solution with Cu_2O sheets with ZnO ALD film from 30 min to 150 min (30, 40, 50, 70, 80, 90, 100, and 150 min). The absorbance at 466 nm keeps increasing during measurement without peak shift.

To confirm absorbance increase is resulted from Cu_2O sheets, the same experiment was done with small amount of Cu_2O sheets. In this case, however, Cu_2O sheets were removed from the MO solution after 90 min using filter paper. Since less amount of Cu_2O sheets was used for this measurement (< 160 cm^2), photodegradation rate is much slower

than Figure 8.2(a), but Figure 8.3 shows the same trend before filtering. Also, there is no change in absorbance after filtering of Cu_2O sheets. Therefore, absorbance increase during UV-irradiation observed with Cu_2O sheets is attributed to Cu_2O sheets, not to MO solution alone.

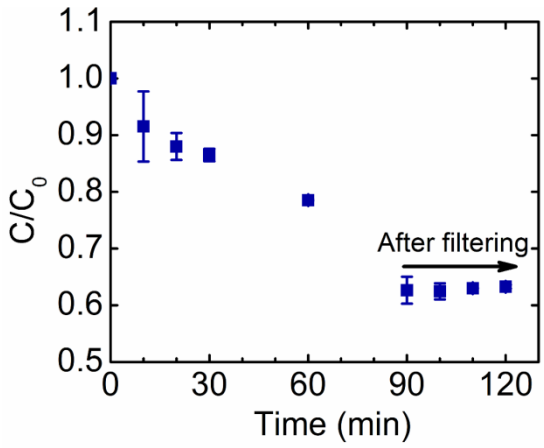

Figure 8.3 Photodegradation of MO solution with Cu_2O sheets under UV light. Cu_2O sheets were filtered after 90 min measurement. After that, there is no change in concentration.

In general, Cu_2O/ZnO composites combined as p-n junction accelerates dye degradation by effective separation of electron-hole pairs.[24] The slopes of Figure 8.2(a) and (b) means the apparent rate constants and show dye photodegradation rate of Cu_2O sheets and Cu_2O/ZnO sheets, respectively. The apparent rate constant for Cu_2O sheets obtained the data before increase in concentration is 0.041 min^{-1}, while Cu_2O/ZnO sheets have ~0.011 min^{-1} that is much slower than that of only Cu_2O sheets (Figure 8.4a and b). Figure 8.4(c) is the SEM image of as-deposited Cu_2O film where Cu_2O crystals in triangular shape are

packed densely with ~500 nm as well as with larger size with ~2 um. Exposed facets of the crystals are photoactive (1 1 1).[25] Interestingly, larger Cu_2O crystals are removed from the film after 100 cycles of ZnO ALD leaving holes on the surface as shown in Figure 8.4(d). They might be removed during purge in the ALD reactor and the decreased Cu_2O density may result in reduced activity after ZnO ALD.

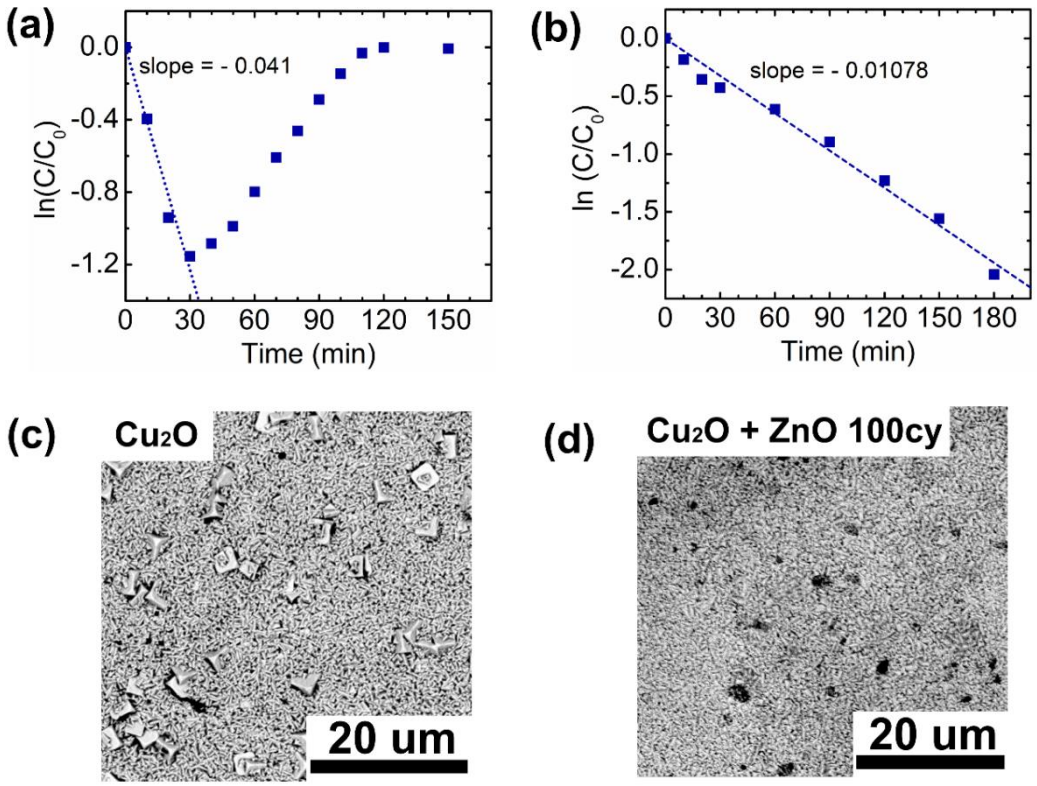

Figure 8.4 Linear plots of ln (C/C_0) vs UV irradiation time with (a) Cu_2O sheets and (b) Cu_2O sheets with ZnO ALD film (extracted from Figure 8.2a and b). The slopes mean the apparent rate constant. SEM images of (a) Cu_2O film electrodeposited for 1 h and (b) Cu_2O film electrodeposited for 1 h followed by ZnO ALD 100 cycles at 60 °C.

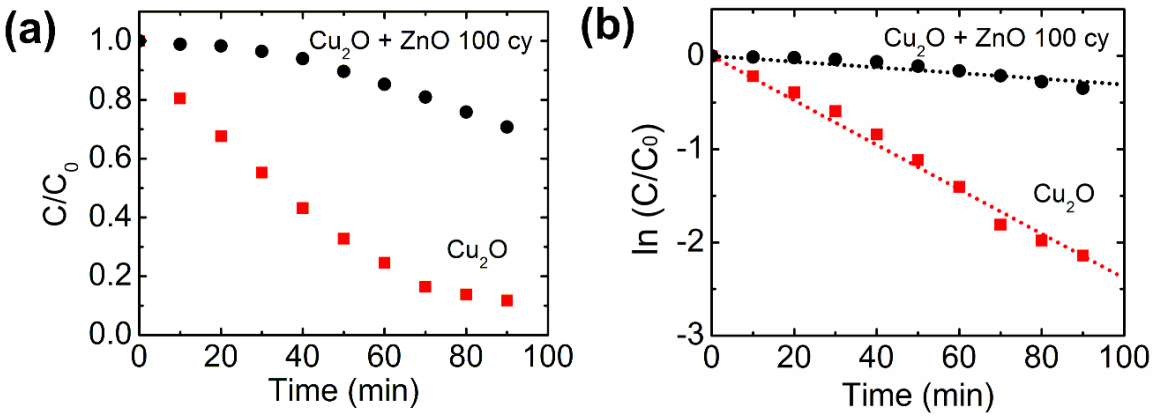

Figure 8.5 (a) Dye degradation under visible light with Cu_2O and Cu_2O/ZnO and (b) ln (C/C_0) vs visible light irradiation time plots calculated from (a). The apparent rate constant extracted from the slope is 0.024 min^{-1} or 0.003 min^{-1} for Cu_2O and Cu_2O/ZnO sheets, respectively.

Photocatalytic activity of Cu_2O was also examined under visible light. Figure 8.5(a) shows that MO solution is gradually degraded with Cu_2O or Cu_2O/ZnO sheets. Unlike under UV light, MO solution continues degradation even with only Cu_2O sheets under visible light. When compared to Cu_2O sheets (apparent rate constant = 0.024 min^{-1}), Cu_2O/ZnO sheets has slower dye degradation with apparent rate constant of 0.003 min^{-1}, as happened under UV-light. The different effect of UV light and Visible light on dye degradation with Cu_2O sheets would be explained after more analysis.

8.4 Summary

In summary, we presented that free-standing Cu_2O sheets from electrodeposition using flexible ITO-PET substrates have photocatalytic effect on dye solutions. Under UV light, Cu_2O sheets degrade dye molecules for 30 min but after that, the concentration of dye solution was increased. This dye recovery was not observed for Cu_2O sheets with ZnO ALD layer. On the other hand, dye solution kept being degraded with Cu_2O sheets under visible light. When compared Cu_2O sheets, Cu_2O sheets with ZnO ALD layer showed slower dye degradation rate under UV or visible light. It may be resulted from Cu_2O damage during ALD despite of low process temperature. Also, SEM images of Cu_2O films before and after ALD shows that some loss of Cu_2O grain during ALD could contribute to decrease in dye degradation rate. Further analysis is required to figure out the mechanism for concentration increase in dye solution with Cu_2O sheets under UV light.

References

(1) Paracchino, A.; Laporte, V.; Sivula, K.; Grätzel, M.; Thimsen, E. Highly active oxide photocathode for photoelectrochemical water reduction. *Nat. Mater.* **2011,** 10, 456.

(2) Kondo, J. Cu_2O as a photocatalyst for overall water splitting under visible light irradiation. *Chem. Commun.* **1998**, 357.

(3) Mittiga, A.; Salza, E.; Sarto, F.; Tucci, M.; Vasanthi, R. Heterojunction solar cell with 2% efficiency based on a Cu_2O substrate. *Appl. Phys. Lett.* **2006,** 88, 163502.

(4) Tran, P. D.; Batabyal, S. K.; Pramana, S. S.; Barber, J.; Wong, L. H.; Loo, S. C. J. A cuprous oxide–reduced graphene oxide (Cu_2O–rGO) composite photocatalyst for hydrogen generation: employing rGO as an electron acceptor to enhance the photocatalytic activity and stability of Cu_2O. *Nanoscale* **2012,** 4, 3875.

(5) Liu, L.; Gu, X.; Sun, C.; Li, H.; Deng, Y.; Gao, F.; Dong, L. In situ loading of ultra-small Cu_2O particles on TiO_2 nanosheets to enhance the visible-light photoactivity. *Nanoscale* **2012,** 4, 6351.

(6) Jiang, T.; Xie, T.; Zhang, Y.; Chen, L.; Peng, L.; Li, H.; Wang, D. Photoinduced charge transfer in ZnO/Cu_2O heterostructure films studied by surface photovoltage technique. *Phys. Chem. Chem. Phys.* **2010,** 12, 15476.

(7) Lalitha, K.; Sadanandam, G.; Kumari, V. D.; Subrahmanyam, M.; Sreedhar, B.; Hebalkar, N. Y. Highly stabilized and finely dispersed Cu_2O/TiO_2: a promising visible sensitive photocatalyst for continuous production of hydrogen from glycerol: water mixtures. *J. Phys. Chem. C* **2010,** 114, 22181.

(8) Musselman, K. P.; Marin, A.; Wisnet, A.; Scheu, C.; MacManus-Driscoll, J. L.; Schmidt-Mende, L. A Novel buffering technique for aqueous processing of zinc oxide nanostructures and interfaces, and corresponding improvement of electrodeposited ZnO-Cu2O photovoltaics. *Adv. Funct. Mater.* **2011,** 21, 573.

(9) Goyal, A.; Reddy, A. L.; Ajayan, P. M. Flexible carbon nanotube–Cu_2O hybrid electrodes for Li-ion batteries. *Small* **2011,** 7, 1709.

(10) Serin, N.; Serin, T.; Horzum, Ş.; Çelik, Y. Annealing effects on the properties of copper oxide thin films prepared by chemical deposition. *Semicond. Sci. Technol.* **2005,** 20, 398.

(11) Hameş, Y.; Eren San, S. CdO/Cu_2O solar cells by chemical deposition. *Solar energy* **2004,** 77, 291.

(12) Chandra, R.; Taneja, P.; Ayyub, P. Optical properties of transparent nanocrystalline Cu_2O thin films synthesized by high pressure gas sputtering. *Nanostruct. Mater.* **1999,** 11, 505.

(13) Yang, W.-Y.; Kim, W.-G.; Rhee, S.-W. Radio frequency sputter deposition of single phase cuprous oxide using Cu_2O as a target material and its resistive switching properties. *Thin Solid Films* **2008,** 517, 967.

(14) Rakhshani, A.; Varghese, J. Potentiostatic electrodeposition of cuprous oxide. *Thin Solid Films* **1988,** 157, 87.

(15) De Jongh, P.; Vanmaekelbergh, D.; Kelly, J. Cu_2O: electrodeposition and characterization. *Chem. Mater.* **1999,** 11, 3512.

(16) Yu, H.; Yu, J.; Liu, S.; Mann, S. Template-free hydrothermal synthesis of CuO/Cu_2O composite hollow microspheres. *Chem. Mater.* **2007,** 19, 4327.

(17) Zhao, H. Y.; Wang, Y. F.; Zeng, J. H. Hydrothermal synthesis of uniform cuprous oxide microcrystals with controlled morphology. *Cryst. Growth Des.* **2008,** 8, 3731.

(18) Liu, R.; Oba, F.; Bohannan, E. W.; Ernst, F.; Switzer, J. A. Shape control in epitaxial electrodeposition: Cu_2O nanocubes on InP (001). *Chem. Mater.* **2003,** 15, 4882.

(19) Li, H.; Liu, R.; Zhao, R.; Zheng, Y.; Chen, W.; Xu, Z. Morphology control of electrodeposited Cu_2O crystals in aqueous solutions using room temperature hydrophilic ionic liquids. *Cryst. Growth Des.* **2006,** 6, 2795.

(20) Sun, F.; Guo, Y.; Song, W.; Zhao, J.; Tang, L.; Wang, Z. Morphological control of Cu_2O micro-nanostructure film by electrodeposition. *J. Cryst. Growth* **2007,** 304, 425.

(21) Ho, J.-Y.; Huang, M. H. Synthesis of submicrometer-sized Cu_2O crystals with morphological evolution from cubic to hexapod structures and their comparative photocatalytic activity. *J. Phys. Chem. C* **2009,** 113, 14159.

(22) Read, C. G.; Steinmiller, E. M.; Choi, K.-S. Atomic plane-selective deposition of gold nanoparticles on metal oxide crystals exploiting preferential adsorption of additives. *J. Am. Chem. Soc.* **2009,** 131, 12040.

(23) Xu, H.; Wang, W.; Zhu, W. Shape evolution and size-controllable synthesis of Cu_2O octahedra and their morphology-dependent photocatalytic properties. *J. Phys. Chem. B* **2006,** 110, 13829.

(24) Deo, M.; Shinde, D.; Yengantiwar, A.; Jog, J.; Hannoyer, B.; Sauvage, X.; More, M.; Ogale, S. Cu2O/ZnO hetero-nanobrush: hierarchical assembly, field emission and photocatalytic properties. *J. Mater. Chem.* **2012,** 22, 17055.

(25) Golden, T. D.; Shumsky, M. G.; Zhou, Y.; VanderWerf, R. A.; Van Leeuwen, R. A.; Switzer, J. A. Electrochemical deposition of copper (I) oxide films. *Chem. Mater.* **1996,** 8, 2499.

Chapter 9

Summary and Outlook

9.1 Summary

ALD has been exploited over 50 years. However, its ability to deposit film uniformly and conformally in atomic range even on the surface with high aspect ratio is becoming more important with scale-down to nanometer range in electronics. ALD films are employed as insulating layer[1] or high-k dielectrics[2,3] in nanoelectronics. On the other hand, the limitation of ALD which is slow deposition rate is becoming less important.[4] Low process temperature allows ALD on thermally weak substrates such as fibers, bio-materials, and polymer film. In particular, a thermal or chemical removal of bio-templates after ALD mimics natural fine 3D structures and readily adopted in nanofabrication. In this work, we showed the mechanism of wetting transitions of PP and cotton fibers after Al_2O_3 ALD. Also, we fabricated metal oxide nanosheet with ALD and carried out Cu_2O electrodeposition with ZnO ALD film as a protective layer.

ALD nucleation and growth on fiber substrates depend on the functional groups on fibers and result in surface property change of fibers. We showed that wetting transitions on PP and cotton fabrics by Al_2O_3 ALD are noticeable. PP fibers abruptly become hydrophilic after a certain Al_2O_3 ALD cycles at 60 °C but it is deposition temperature dependent. Wetting property change of PP at 60 °C could be explained by an increase in hydrophilic Al_2O_3 film on the surface but at higher temperature, 90 °C, precursors penetrate deeply inside expanded fibers. This results in more subsurface growth and exposed surface carbon leaving the PP fibers hydrophobic. Cotton fibers changes from complete wetting to hydrophobic only after 3 Al_2O_3 ALD cycles and then turns back to complete wetting with more ALD cycles. We

found out that hydrophobic transition of cotton fibers may be resulted from Al-(O-C-)$_3$ bonding remained only for the several initial ALD cycles. Also, surface roughness on the hydrophobic cotton surface promotes surface nonwetting properties.

We first reported 2D metal oxide nanosheets by ALD. ALD films with controlled thickness and chemical composition were released from the sacrificial polymer layer in the solvent. The nanosheets have up to ~5 mm lateral size but with only a few nm in thickness that are matched with the ALD film thickness. The size of nanosheets depends on the sacrificial polymers and ALD materials. TiO_2 and ZnO nanosheets showed their photocatalytic activity with organic dye degradation. Especially, TiO_2/ZnO bi-layer nanosheets (2.5 nm/2.5 nm) showed 5 times faster dye photodegradation than TiO_2 nanosheets (2.5 nm), which puts emphasis on the advantage of ALD to fabricate multilayer nanosheets like p-n junctions.

Also, we deposited Cu_2O films which are p-type semiconductor by electrodeposition with various temperatures, pH of the solution, and deposition time. There was no change on the Cu_2O morphology but grain size was increased with high deposition temperature, high pH of the solution, and longer deposition time. To protect Cu_2O films from the electrolyte during electrochemical measurements, TiO_2 ALD films with Al:ZnO buffer layer were deposited on Cu_2O films. However, we did not observe the similar enhancement that Paracchino *et al.* observed with the same thickness of each layer.[5] As isolated sheets, electrodeposited Cu_2O films were separated from flexible ITO-PET substrates by simple bending. Cu2O sheets with the thickness of ~1 μm were shown their photocatalytic activity under UV and visible light. But under UV, the dye solution showed recovery after some

degradation, which was not observed under visible light. Thin ZnO ALD layer on Cu_2O film before separation prevented dye recovery. However, even performed at low temperature, 60 °C, ALD damaged Cu_2O film resulting in slower dye degradation rate.

9.2 Outlook

Our work on fibers can be commercially employed as hydrophobic cotton fabrics and hydrophilic PP fibers for diapers, bandage, or easy-clean textiles. The mechanism on cotton fibers during wetting/nonwetting transitions would help to understand reactions during several initial cycles on other fiber substrates.

Metal oxide nanosheets fabricated by ALD are very promising in various applications such as photocatalysts, gate layer, and insulating layer in nanoelectronics. The most important merit of ALD is that the multilayer nanosheets including p-n junction layers can be easily fabricated with successive ALD. In addition, ALD can provide an effective way to understand how the thicknesses and compositions of nanosheets affect their performance and find out the optimal conditions for the best performance. The free-standing Cu_2O film also can be used as photocatalysts like metal oxide nanosheets. Although not presented in this work, multilayer nanosheets by ALD or electrodeposited Cu_2O film with n-type ALD layer can be employed in water splitting. We tried to split water with Cu_2O film with Al:ZnO and TiO_2 ALD layers but did not observe water splitting. We think that Al:ZnO is not conductive enough to establish ohmic contact, so we need Pt or Ag thin layer between Cu_2O and TiO_2 layer which are very conductive and accommodate ohmic contact layers. We believe that our

works on the fabrication of free-standing nanosheets expand ALD application areas to energy storage and water splitting.

References

(1) Lin, H.; Ye, P.; Wilk, G. Leakage current and breakdown electric-field studies on ultrathin atomic-layer-deposited Al_2O_3 on GaAs. *Appl. Phys. Lett.* **2005,** 87, 182904.

(2) Ye, P.; Wilk, G.; Kwo, J.; Yang, B.; Gossmann, H.-J.; Frei, M.; Chu, S.; Mannaerts, J.; Sergent, M.; Hong, M. GaAs MOSFET with oxide gate dielectric grown by atomic layer deposition. *Electron Device Letters, IEEE* **2003,** 24, 209.

(3) Gusev, E.; Shang, H.; Copel, M.; Gribelyuk, M.; DEmic, C.; Kozlowski, P.; Zabel, T. Microstructure and thermal stability of HfO_2 gate dielectric deposited on Ge (100). *Appl. Phys. Lett.* **2004,** 85, 2334.

(4) Leskelä, M.; Ritala, M. Atomic layer deposition (ALD): from precursors to thin film structures. *Thin Solid Films* **2002,** 409, 138.

(5) Paracchino, A.; Laporte, V.; Sivula, K.; Gratzel, M.; Thimsen, E. Highly active oxide photocathode for photoelectrochemical water reduction. *Nat. Mater.* **2011,** 10, 456.

APPENDIX

Langmuir 2009 (26) 2550

Atomic Layer Deposition and Abrupt Wetting Transitions on Nonwoven Polypropylene and Woven Cotton Fabrics

G. Kevin Hyde, Giovanna Scarel, Joseph C. Spagnola, Qing Peng, Kyoungmi Lee, Bo Gong, Kim G. Roberts, Kelly M. Roth, Christopher A. Hanson, Christina K. Devine, S. Michael Stewart, Daisuke Hojo, Jeong-Seok Na, Jesse S. Jur, and Gregory N. Parsons

ABSTRACT: Atomic layer deposition (ALD) of aluminum oxide on nonwoven polypropylene and woven cotton fabric materials can be used to transform and control fiber surface wetting properties. Infrared analysis shows that ALD can produce a uniform coating throughout the nonwoven polypropylene fiber matrix, and the amount of coating can be controlled by the number of ALD cycles. Upon coating by ALD aluminum oxide, nonwetting hydrophobic polypropylene fibers transition to either a metastable hydrophobic or a fully wetting hydrophilic state, consistent with well-known Cassie-Baxter and Wenzel models of surface wetting of roughened surfaces. The observed nonwetting/wetting transition depends on ALD process variables such as the number of ALD coating cycles and deposition temperature. Cotton fabrics coated with ALD aluminum oxide at moderate temperatures were also observed to transition from a natural wetting state to a metastable hydrophobic state and back to wetting depending on the number of ALD cycles. The transitions on cotton appear to be less sensitive to deposition temperature. The results provide insight into the effect of ALD

film growth mechanisms on hydrophobic and hydrophilic polymers and fibrous structures. The ability to adjust and control surface energy, surface reactivity, and wettability of polymer and natural fiber systems using atomic layer deposition may enable a wide range of new applications for functional fiber-based systems.

My contribution on this work includes measuring water contact angle on cotton fabrics with Al_2O_3 ALD and taking water drop images.

Langmuir 2010 (26) 8239

Temperature-Dependent Subsurface Growth during Atomic Layer Deposition on Polypropylene and Cellulose Fibers

Jesse S. Jur , Joseph C. Spagnola , Kyoungmi Lee , Bo Gong , Qing Peng and Gregory N. Parsons

ABSTRACT: Nucleation and subsequent growth of aluminum oxide by atomic layer deposition (ALD) on polypropylene fiber substrates is strongly dependent on processing temperature and polymer backbone structure. Deposition on cellulose cotton, which contains ample hydroxyl sites for ALD nucleation and growth on the polymer backbone, readily produces a uniform and conformal coating. However, similar ALD processing on polypropylene, which contains no readily available active sites for growth initiation, results in a graded and intermixed polymer/inorganic interface layer. The structure of the polymer/inorganic layer depends strongly on the process temperature, where lower temperature (60 °C) produced a more abrupt transition. Cross-sectional transmission electron microscopy images of polypropylene fibers coated at higher temperature (90 °C) show that non-coalesced particles form in the near-surface region of the polymer, and the particles grow in size and coalesce into a film as the number of ALD cycles increases. Quartz crystal microbalance analysis on polypropylene films confirms enhanced mass uptake at higher processing temperatures, and X-ray photoelectron spectroscopy data also confirm heterogeneous mixing between the aluminum oxide and the polypropylene during deposition

at higher temperatures. The strong temperature dependence of film nucleation and subsurface growth is ascribed to a relatively large increase in bulk species diffusivity that occurs upon the temperature-driven free volume expansion of the polypropylene. These results provide helpful insight into mechanisms for controlled organic/inorganic thin film and fiber materials integration.

My contribution on this work is XPS measurement and analysis for polypropylene fibers after Al_2O_3 ALD 100 cycles at 60 and 90 °C as well as after TMA soaked for 60 min at 80 °C.

Chem. Mater. 2011, (23) 3476

Sequential Vapor Infiltration of Metal Oxides into Sacrificial Polyester Fibers: Shape Replication and Controlled Porosity of Microporous/Mesoporous Oxide Monoliths

Bo Gong, Qing Peng, Jesse S. Jur, Christina K. Devine, Kyoungmi Lee, and Gregory N. Parsons*

ABSTRACT: The preparation of microporous and mesoporous metal oxide materials continues to attract considerable attention, because of their possible use in chemical separations, catalyst support, chemical sensors, optical and electronic devices, energy storage, and solar cells. While many methods are known for the synthesis of porous materials, researchers continue to seek new methods to control pore size distribution and macroscale morphology. In this work, we show that sequential vapor infiltration (SVI) can yield shape controlled micro/mesoporous materials with tunable pore size, using polyesters as a sacrificial template. The reaction proceeds by exposing polymer fiber templates to a controlled sequence of metal organic and co-reactant vapor exposure cycles in an atomic layer deposition (ALD) reactor. The precursors infuse sequentially and thereby distribute and react uniformly within the polymer, to yield an organic-inorganic hybrid material that retains the physical dimensions of the original polymer template. Subsequent calcination in air results in an inorganic microporous/mesoporous material that again retains the macroscopic physical shape of the starting polymer matrix. The microporous/mesoporous structure is

confirmed by microscopy and nitrogen adsorption/desorption analysis, and the resulting pore size is controlled by the size of the starting polymer repeat unit and by the kinetics of the infiltration/annealing process steps. In situ infrared transmission and quartz crystal microbalance results confirm the chemical reaction mechanisms. The chemical transformation that occurs during SVI could be important for a range of applications that utilize well-defined porous nanostructures.

My contribution on this work is XPS measurement and analysis of polybutylene terephthalate (PBT) films after TMA/water infiltration.

Appl. Phys. Lett. 2011 (99) 112115

SiNx Charge-Trap Nonvolatile Memory Based on ZnO Thin-Film Transistors

Eunkyeom Kim, Youngill Kim, Do Han Kim, Kyoungmi Lee, Gregory N. Parsons, and Kyoungwan Park

ABSTRACT: We have demonstrated the fabrication and application of a nonvolatile thin-film transistor memory with SiN_x charge traps using a ZnO thin film as the active channel layer. The thin film of ZnO was deposited using an atomic-layer deposition process and was subsequently post-annealed in an O_2-filled atmosphere. X-ray diffraction and x-ray photoemission results indicated that the O_2 annealing process was effective for the crystallinity and stoichiometry of the ZnO films. A saturation field-effect mobility of 6 cm^2/Vs, on/off ratio of $\approx 10^5$, subthreshold slope of 0.7 V/decade, and threshold voltage of −5 V were obtained in transistor operations. Threshold-voltage shift measurements performed for various stress voltages and time durations revealed that these devices had a large memory window of 5.4 V and a long retention time (>10 years) in nonvolatile memory operations.

My contribution on this work is atomic layer deposition of ZnO on the substrates.

J. Vac. Sci. Technol. A 2012 (30) 01A105

Wetting Properties Induced in Nano-Composite POSS-MA Polymer Films by Atomic Layer Deposited Oxides

Kyle A. Vasquez, Anita J. Vincent-Johnson, W. Christopher Hughes, Brian H. Augustine, Kyoungmi Lee, Gregory N. Parsons, and Giovanna Scarel

ABSTRACT: Due to their unique properties, nano-composite polyhedral oligomeric silsequioxane (POSS) copolymer films are attractive for various applications. Here we show that their natural hydrophobic character can become hydrophilic when the films are modified by a thin oxide layer, up to 8 nm thick, prepared using atomic layer deposition. A proper choice of the deposition temperature and thickness of the oxide layer are required to achieve this goal. Unlike other polymeric systems, a marked transition to a hydrophilic state is observed with oxide layers deposited at increasing temperatures up to the glass transition temperature (~110 °C) of the POSS copolymer film. The hydrophilic state is monitored through the water contact angle of the POSS film. Infrared absorbance spectra indicate that, in hydrophilic samples, the integral of peaks corresponding to surface Al–O (hydrophilic) is significantly larger than that of peaks linked to hydrophobic species.

My contribution on this work is SEM measurement of ALD Al_2O_3-coated POSS-MA films on silicon.

Nanoscale, 2012, (4) 4731

Stable Anatase TiO_2 Coating on Quartz Fibers by Atomic Layer Deposition for Photoactive Light-Scattering in Dye-Sensitized Solar Cells

Do Han Kim, Hyung-Jun Koo, Jesse S. Jur, Mariah Woodroof, Berç Kalanyan, Kyoungmi Lee, Christina K. Devine and Gregory N. Parsons

ABSTRACT: Quartz fibers provide a unique high surface-area substrate suitable for conformal coating using atomic layer deposition (ALD), and are compatible with high temperature annealing. This paper shows that the quartz fiber composition stabilizes ALD TiO_2 in the anatase phase through TiO_2–SiO_2 interface formation, even after annealing at 1050 °C. When integrated into a dye-sensitized solar cell, the TiO_2-coated quartz fiber mat improves light scattering performance. Results also confirm that annealing at high temperature is necessary for better photoactivity of ALD TiO_2, which highlights the significance of quartz fibers as a substrate. The ALD TiO_2 coating on quartz fibers also boosts dye adsorption and photocurrent response, pushing the overall efficiency of the dye-cells from 6.5 to 7.4%. The mechanisms for improved cell performance are confirmed using wavelength-dependent incident photon to current efficiency and diffuse light scattering results. The combination of ALD and thermal processing on quartz fibers may enable other device structures for energy conversion and catalytic reaction applications.

My contribution on this work includes assisting TiO_2 ALD on quartz fibers and discussion about the results.

ChemSusChem 2013 (6) 1014

Atomic Layer Deposition of High Performance Ultrathin TiO_2 Blocking Layers for Dye-Sensitized Solar Cells

Do Han Kim, Mariah Woodroof, Kyoungmi Lee, and Gregory N. Parson

ABSTRACT: Dye-sensitized solar cells (DSSCs) often use a thin insulating or semiconducting layer (typically TiO_2) between the transparent conductive oxide and the mesoporous TiO_2 to block electron/hole recombination at the conducting oxide/electrolyte interface. The blocking layer (BL) is essential to maintain efficient charge generation under low light conditions, at which DSSCs perform well compared to common semiconductor-based photovoltaic devices. In this work, we show that atomic layer deposition (ALD) can produce ultrathin (<10 nm) BLs that significantly impede charge recombination in functional DSSCs, leading to improved photocurrents, open-circuit photovoltages, and fill factors; this results in an increase in the overall efficiency from 7% to 8.4% under AM 1.5G illumination. The 5 – 10 nm ALD BLs are the thinnest optimized DSSC BLs reported to date. The BL retards the open-circuit voltage decay and extends the electron lifetime from 0.2 s to more than 10 s at 0.3 V, confirming that the ALD films significantly impede photogenerated charge recombination. By preparing BLs through other deposition techniques, we directly demonstrate that ALD results in better performance, even with thinner films, which is ascribed to the lower pinhole density of ALD materials.

My contribution on this work includes assisting TiO_2 ALD on mesoporous TiO_2 layer and discussion about the results.

Coordin. Chem. Rev. 2013 in press

Mechanisms and Reactions during Atomic Layer Deposition on Polymers

Gregory N. Parsons, Sarah E. Atanasov, Erinn C. Dandley, Christina K. Devine, Bo Gong, Jesse S. Jur, Kyoungmi Lee, Christopher J. Oldham, Qing Peng, Joseph C. Spagnola, Philip S. Williams

ABSTRACT: There is significant growing interest in atomic layer deposition onto polymers for barrier coatings, nanoscale templates, surface modification layers and other applications. The ability to control the reaction between ALD precursors and polymers opens new opportunities in ALD materials processing. It is well recognized that ALD on many polymers involves subsurface precursor diffusion and reaction which are not encountered during ALD on solid surfaces. This article reviews recent insights into chemical reactions that proceed during ALD on polymers, with particular focus on the common Al_2O_3 reaction sequence using trimethyl aluminum (TMA) and water. We highlight the role of different polymer reactive groups in film growth, and how the balance between precursor diffusion and reaction can change as deposition proceeds. As a strong Lewis acid, TMA forms adducts with Lewis base sites within the polymer, and the reactions that proceed are determined by the neighboring bond structure. Moreover, the Lewis base sites can be saturated by TMA, producing a self-limiting half-reaction within a three-dimensional polymer, analogous to a self-limiting half-reaction commonly observed during ALD on a solid planar surface.

My contribution on this work includes Al_2O_3 and ZnO ALD on cotton and polypropylene fibers, examination their wetting properties, and surface analysis of cotton fiber substrates during wetting transition.